

## ABSTRACT

### Characterization of the Internal Temperature and Phase State of Amorphous Materials Using Ultrasonic Non-Destructive Evaluation

Taylor Danielle Jeffrey, M.S.M.E

Mentor: David A. Jack, Ph.D.

Ultrasound has a wide range of applicability and is used across many industries for non-destructive evaluation. Temperature is one of the key parameters in thermodynamic systems, and ultrasound has been studied as a means of temperature measurement for many years. Polymer, petro-chemical, power plant, food processing, and composites are just some of the industries which already make use of ultrasonics and stand to benefit from advances in the understanding and technology surrounding ultrasonic testing and evaluation. This research uses an amorphous wax with a low coefficient of thermal expansion; it is highly attenuative, and that attenuation change is a function of the temperature of the wax. The results of this research demonstrate the ability of this method to approximate 2D planar temperature behavior of the wax using only ultrasonic data and externally located thermocouples, making it a truly non-invasive method.

Characterization of the Internal Temperature and Phase State of Amorphous Materials Using  
Ultrasonic Non-Destructive Evaluation

by

Taylor Danielle Jeffrey, B.S.M.E.

A Thesis

Approved by the Department of Mechanical Engineering

---

Paul I. Ro, Ph.D., Chairperson

Submitted to the Graduate Faculty of  
Baylor University in Partial Fulfillment of the  
Requirements for the Degree  
of  
Master of Science

Approved by the Thesis Committee

---

David A. Jack, Ph.D., Chairperson

---

Ian Gravagne, Ph.D.

---

William Jordan, Ph.D.

Accepted by the Graduate School

August 2019

---

J. Larry Lyon, Ph.D., Dean

Copyright © 2019 by Taylor Danielle Jeffrey

All rights reserved

## TABLE OF CONTENTS

LIST OF FIGURES .....	v
LIST OF TABLES .....	viii
ACKNOWLEDGMENTS .....	ix
DEDICATION .....	x
CHAPTER ONE .....	1
Introduction.....	1
1.1 . Motivation and Articulation	2
1.2 . Thesis Overview	3
CHAPTER TWO .....	6
Literature Review.....	6
2.1 . Introduction	6
2.2 Ultrasonic Basics	8
2.3 Ultrasound in Material Characterization and Monitoring	11
2.4 Ultrasound in Temperature Monitoring	15
2.5 Ultrasound and Current Research	23
CHAPTER THREE .....	24
Experimentation and Data Processing .....	24
3.1 . Ultrasonic Theory	24
3.2 . Material Characterization	31
3.3 . Experimental Set Up	39
3.4 . MATLAB and LabVIEW	46
3.5 Radial Temperature Approximation	68
3.6 2D Temperature Approximation	82
CHAPTER FOUR.....	85
Data Analysis and Results .....	85
4.1 Time of Flight and Bulk Speed of Sound Curves	86
4.2 . Thermocouple Data	98
4.3 2D Approximated Temperature Profiles	102
4.4 Further Experimentation	118
CHAPTER FIVE .....	125
Conclusions and Future Work .....	125
5.1 Scientific Contributions	125
5.2 Future Work	126
5.3 Conclusions	127
APPENDIX.....	129
BIBLIOGRAPHY.....	136

## LIST OF FIGURES

Figure 2.1. A-scan.....	10
Figure 2.2. Pulse-echo (left) and through-transmission (right) transducer setup. ....	11
Figure 3.1. Transducer and beam divergence .....	25
Figure 3.2. Flowchart of through-transmission ultrasonic testing .....	26
Figure 3.3. A-scan as displayed by LabVIEW .....	27
Figure 3.4. Methods of determining time of flight. ....	28
Figure 3.5. Normalized a-scan and $\pm 30\%$ detection threshold. ....	29
Figure 3.6. Ultrasonic testing methods: Pulse-echo (left), pitch-catch (center), through-transmission (right) .....	30
Figure 3.7. EUT3160 Pulsar/receiver .....	31
Figure 3.8. Olympus and Panametrics transducers .....	32
Figure 3.9. Graphtec midiLOGGER GL820.....	32
Figure 3.10. TA Instruments Differential Scanning Calorimeter Q20. ....	34
Figure 3.11. DSC curve for CBL-125 at a rate of $2^{\circ}\text{C}/\text{min}$ .....	34
Figure 3.12. CBL-125 with five thermocouples for thermal equilibrium tests (left) and Thermo Scientific Precision Compact Oven (right). ....	36
Figure 3.13 Time of flight at $34^{\circ}\text{C}$ (left) and $61^{\circ}\text{C}$ (right). ....	37
Figure 3.14 Diagram of isothermal wax container .....	37
Figure 3.15. CBL-125 Speed of Sound vs Temperature Master Curve.....	38
Figure 3.16. Watlow EZ-Zone temperature controller with hookups.....	40
Figure 3.17. Diagram of internal experimental setup. ....	41
Figure 3.18. Ultrasonic pathways and thermocouple bar location.....	42
Figure 3.19. Ultem dimensions.....	45

Figure 3.20. Representative Ultem insulating plate.....	45
Figure 3.21 Diagram of the experimental setup (left) and photograph of the experimental setup (right).....	46
Figure 3.22. High SNR a-scan (left) and low SNR a-scan (right) .....	49
Figure 3.23. Raw signal intensity (top) and normalized signal intensity (bottom).....	52
Figure 3.24. Typical a-scan after signal shifting and +/-100 normalization.....	53
Figure 3.25. Measured time of flight for a representative channel.....	55
Figure 3.26. Calculated bulk speed of sound for a representative channel.....	56
Figure 3.27. Recorded electrical gain of a representative channel.....	59
Figure 3.28. B-scan for a representative channel.....	60
Figure 3.29. Time of flight for Channel 1 with multiple detection thresholds .....	61
Figure 3.30. Channel 3 a-scan at t = 30 minutes with detection threshold of 30% (left) and 85% (right) .....	62
Figure 3.31. a) Channel 1 TOF with detection thresholds b) Channel 1 b-scan.....	63
Figure 3.32. Time of flight curve after signal processing.....	64
Figure 3.33 Channel 1 b-scan with TOF curve superimposed.....	65
Figure 3.34 Bulk speed of sound curves.....	66
Figure 3.35. Thermocouple temperature approximation scheme .....	67
Figure 3.36. 2D temperature mapping from internal thermocouple data at a time when the bucket is not fully melted on the top plane (left) and bottom plane (right). .....	67
Figure 3.37 Radial symmetry.....	69
Figure 3.38. Three categories of wax melt. ....	70
Figure 3.39. Temperature profile for $X < 0$ during a) heating and b) cooling.....	72
Figure 3.40. Temperature profile for $0 < X < r_{\text{wall}}$ during a) heating and b) cooling.....	76
Figure 3.41. COMSOL model of 1D heat equation for heating approximation. ....	76
Figure 3.42. COMSOL model of 1D heat equation for cooling approximation.....	77

Figure 3.43. Temperature profile for $X > r_{\text{wall}}$ during a) heating and b) cooling.....	79
Figure 3.44 Plot of measured bulk TOF and estimated bulk TOF for Channel 1.....	81
Figure 3.45 Channel 1 radial temperature over time. ....	82
Figure 3.46. Interpolation between ultrasonic paths.....	83
Figure 3.47. 2D temperature approximation for ultrasonic data from the a) upper plane and b) lower plane. ....	84
Figure 4.1. Recorded gain from Channel 1 (left) and Channel 5 (right). ....	87
Figure 4.2 TOF from Channel 1 (left) and Channel 5 (right). ....	88
Figure 4.3. Bulk speed of sound for Channel 1 (left) and Channel 5 (right).....	88
Figure 4.4. Raw and filtered a-scan for a) Channel 1 at $t = 100$ min, b) Channel 5 at $t = 100$ min, c) Channel 1 at $t = 180$ minutes, d) Channel 5 at $t = 180$ min. ....	90
Figure 4.5. Recorded electrical gain for Channel 4. ....	91
Figure 4.6. B-scan for Channel 4 (top) and Channel 3 (bottom). ....	92
Figure 4.7. TOF curve for Channel 4.....	93
Figure 4.8. Channel 4 b-scan with TOF curve superimposed in red. ....	94
Figure 4.9. TOF curves for all 8 channels ....	95
Figure 4.10. Time of flight curves with notable times.....	96
Figure 4.11. Bulk SOS curves for all 8 channels ....	97
Figure 4.12. Internal thermocouple numbering scheme ....	98
Figure 4.13. Internal thermocouple temperatures ....	99
Figure 4.14. Location and labeling of external transducers and thermocouples on the upper plane (left) and lower plane (right).....	100
Figure 4.15. External thermocouples ....	101
Figure 4.16 Comparison of linear and spline fits for TC25.....	102
Figure 4.17. Comparison of measured TOF and approximate TOF for Channel 5.....	103
Figure 4.18. Radial temperature over time for Channel 5. ....	104

Figure 4.19 Top xy-plane temperature at $t_{\text{experiment}} = 0$ minutes, a) experimental observation, b) approximated temperature state from acoustic measurements. ....	105
Figure 4.20 Bottom xy-plane temperature at $t_{\text{experiment}} = 0$ minutes, a) experimental observation, b) approximated temperature state from acoustic measurements. ....	105
Figure 4.21 Top xy-plane temperature at $t_{\text{experiment}} = 66$ minutes, a) experimental observation, b) approximated temperature state from acoustic measurements. ....	106
Figure 4.22 Bottom xy-plane temperature at $t_{\text{experiment}} = 66$ minutes, a) experimental observation, b) approximated temperature state from acoustic measurements. ....	106
Figure 4.23 Top xy-plane temperature at $t_{\text{experiment}} = 127$ minutes, a) experimental observation, b) approximated temperature state from acoustic measurements. ....	107
Figure 4.24 Bottom xy-plane temperature at $t_{\text{experiment}} = 127$ minutes, a) experimental observation, b) approximated temperature state from acoustic measurements. ....	107
Figure 4.25 Top xy-plane temperature at $t_{\text{experiment}} = 205$ minutes, a) experimental observation, b) approximated temperature state from acoustic measurements. ....	108
Figure 4.26 Bottom xy-plane temperature at $t_{\text{experiment}} = 205$ minutes, a) experimental observation, b) approximated temperature state from acoustic measurements. ....	108
Figure 4.27 Top xy-plane temperature at $t_{\text{experiment}} = 233$ minutes, a) experimental observation, b) approximated temperature state from acoustic measurements. ....	109
Figure 4.28 Bottom xy-plane temperature at $t_{\text{experiment}} = 233$ minutes, a) experimental observation, b) approximated temperature state from acoustic measurements. ....	109
Figure 4.29. Top xy-plane temperature at $t_{\text{experiment}} = 254$ minutes, a) experimental observation, b) approximated temperature state from acoustic measurements. ....	110
Figure 4.30. Bottom xy-plane temperature at $t_{\text{experiment}} = 254$ minutes, a) experimental observation, b) approximated temperature state from acoustic measurements. ....	110
Figure 4.31 Top xy-plane temperature at $t_{\text{experiment}} = 272$ minutes, a) experimental observation, b) approximated temperature state from acoustic measurements. ....	111
Figure 4.32 Bottom xy-plane temperature at $t_{\text{experiment}} = 272$ minutes, a) experimental observation, b) approximated temperature state from acoustic measurements. ....	112
Figure 4.33. Top xy-plane temperature at $t_{\text{experiment}} = 310$ minutes, a) experimental observation, b) approximated temperature state from acoustic measurements. ....	112
Figure 4.34 Bottom xy-plane temperature at $t_{\text{experiment}} = 310$ minutes, a) experimental observation, b) approximated temperature state from acoustic measurements. ....	113

Figure 4.35 Top xy-plane temperature at  $t_{\text{experiment}} = 366$  minutes, a) experimental observation, b) approximated temperature state from acoustic measurements. .... 114

Figure 4.36 Bottom xy-plane temperature at  $t_{\text{experiment}} = 366$  minutes, a) experimental observation, b) approximated temperature state from acoustic measurements. .... 114

Figure 4.37 Top xy-plane temperature at  $t_{\text{experiment}} = 497$  minutes, a) experimental observation, b) approximated temperature state from acoustic measurements. .... 115

Figure 4.38 Bottom xy-plane temperature at  $t_{\text{experiment}} = 497$  minutes, a) experimental observation, b) approximated temperature state from acoustic measurements. .... 115

Figure 4.39 Top xy-plane temperature at  $t_{\text{experiment}} = 552$  minutes, a) experimental observation, b) approximated temperature state from acoustic measurements. .... 116

Figure 4.40 Bottom xy-plane temperature at  $t_{\text{experiment}} = 552$  minutes, a) experimental observation, b) approximated temperature state from acoustic measurements. .... 116

Figure 4.41 Average temperature difference between ultrasonic and thermocouple 2D temperature approximations over time. .... 117

Figure 4.42 Time of flight curves ..... 119

Figure 4.43 Top xy-plane temperature at  $t_{\text{experiment}} = 0$  minutes, a) experimental observation, b) approximated temperature state from acoustic measurements. .... 120

Figure 4.44 Bottom xy-plane temperature at  $t_{\text{experiment}} = 0$  minutes, a) experimental observation, b) approximated temperature state from acoustic measurements. .... 120

Figure 4.45 Top xy-plane temperature at  $t_{\text{experiment}} = 74$  minutes, a) experimental observation, b) approximated temperature state from acoustic measurements. .... 121

Figure 4.46 Bottom xy-plane temperature at  $t_{\text{experiment}} = 74$  minutes, a) experimental observation, b) approximated temperature state from acoustic measurements. .... 121

Figure 4.47 Top xy-plane temperature at  $t_{\text{experiment}} = 151$  minutes, a) experimental observation, b) approximated temperature state from acoustic measurements. .... 122

Figure 4.48 Bottom xy-plane temperature at  $t_{\text{experiment}} = 151$  minutes, a) experimental observation, b) approximated temperature state from acoustic measurements. .... 122

Figure 4.49 Top xy-plane temperature at  $t_{\text{experiment}} = 249$  minutes, a) experimental observation, b) approximated temperature state from acoustic measurements. .... 123

Figure 4.50 Bottom xy-plane temperature at  $t_{\text{experiment}} = 249$  minutes, a) experimental observation, b) approximated temperature state from acoustic measurements. .... 123

Figure 4.51 Average temperature difference between ultrasonic and thermocouple 2D temperature approximations over time ..... 124

## LIST OF TABLES

Table 3.1. Transducer pairs and ultrasonic channels .....	43
---	----

## ACKNOWLEDGMENTS

I must first thank Dr. David Jack, for without his teaching, encouragement, and mentoring, this would not have been possible. I learned a great deal from his classes, but also from his leadership style and watching him foster an environment of teamwork and mutual support. His rapport with all of the graduate students is evident as soon as you walk into the lab, and I am incredibly grateful to have been part of the SICEM research group as one of Dr. Jack's students.

Speaking of the SICEM group, I have to say that the snark, the commiseration, the encouragement, the extra sets of hands, and all the camaraderie made graduate school a good experience. Special thanks to Nate Blackman for his help with MATLAB and LabVIEW coding and troubleshooting.

I would like to thank all of my family for supporting my decision to pursue this degree, for their love and encouragement, and for believing in me even when I didn't believe in myself.

Thank you to Sandia National Laboratories for their funding and support of this research, and a special thanks to David Moore and Sarah Stair for their collaboration and work on this project.

Finally, I would like to thank Dr. David Jack, Dr. Bill Jordan, and Dr. Ian Gravagne for serving on my committee.

## DEDICATION

To my daughter, Cara

## CHAPTER ONE

### Introduction

In many industrial, scientific, and engineering applications there is a need to characterize the internal temperature distribution within a material as it undergoes thermal gradients. This is particularly of interest for materials transitioning between a solid-like to a liquid-like behavior as there are often substantial changes in the thermal gradients near the phase transition boundary. Thermocouples are a common solution, however they are an invasive method which may damage the material during insertion or disrupt flow during the phase change, cause non-uniform heating due to their thermal conductive behavior within the structure itself, or have limited use long-term in high-temperature or other hostile environments. Infrared imaging is commonly used for temperature measurement, however it is limited to the surface temperature of the material or container and cannot provide quantification of the internal temperature state.

Thermography and temperature mapping using ultrasonics have been researched for many years, and there are new methods and techniques for temperature reconstruction being created and studied nearly every single year. It has been observed that ultrasonic signals vary in time-of-flight, intensity, and wave characteristics based on temperature and phase of a material, they can be used to interpret the physical or chemical changes occurring within a material .

Wax is selected for this research, due to its amorphous nature and melt over a range of temperatures, specifically a wax with a safe melting temperature around 50°C and a broad phase transition temperature band. Unlike water, which changes phase at 100

degrees Celsius, the wax transitions from a semi-solid to a softened gel with a measurable viscosity to that of a low viscosity fluid over a broad range of temperatures. This behavior is sought out to represent that of a thermoplastic experiencing cooling and heating through the transition temperature, or a slurry experiencing curing.

### *1.1. Motivation and Articulation*

The ability to determine temperature and phase of materials through non-invasive techniques has immediate applications in the petro-chemical industry, the food industry, the composites industry, and the polymer industry. The Trans-Alaska Pipeline faces the challenge of crude oil threatening to drop below the temperature where the viscosity increases into a range which causes difficulty with flow, a complication which is typically detected by change in flow at pump stations. In the oil and gas industry, oil tie-back wells need to be poured and cured quickly. The use of ultrasonics for in-situ monitoring of the cement curing process could reduce the time spent waiting for the cement to cure, improving efficiency and saving drilling companies valuable time and money.

Food composition and phase can also be measured using ultrasound. Sugar-based candies must reach specific temperatures to maintain their desired texture once cool. Chocolate fat content and temperature is critical to the tempering process. Using a non-invasive method like the one proposed in this thesis can increase the safety and sanitation levels of the monitoring process while monitoring the internal uniformity of the temperature the food experiences.

In polymer processing, the temperature of the polymer melt during molding and demolding has significant impact on the properties of the finished part. This is especially

true for injection molding of thermoplastics, screw extrusion of polymers, and the extruders used in large area additive manufacturing. Ultrasonic monitoring of temperature in these applications can be used to gain insight into the exact temperature across a part or polymer flow, as well as the cooling behavior and process, leading to increased efficiency, reduced thermal warping, and improved part performance. The ability to quantify in-situ the cure state within a thermoset laminated composite would be of interest to both the automotive and aerospace industries.

### *1.2. Thesis Overview*

This thesis contains two notable scientific contributions. The first is the approximation of temperature in a solid without use of a waveguide. While previous research with wax and other solid materials has determined the effective temperature, assuming there is no thermal gradient in the material, solid materials typically require use of a waveguide to determine the change in temperature through a material. This research uses a mathematical approximation for the internal temperature state of a solid material. The second scientific contribution is the mathematical modeling of the temperature within a material as it undergoes phase change, using ultrasonic data and wall temperature boundary conditions. Previous work done with a similar wax successfully modeled phase as a binary system, either liquid or solid. This research goes beyond phase and into a temperature profile across a 2D plane of the material.

This thesis consists of five chapters. Chapter Two is a review of literature relevant to discerning phase and temperature using ultrasonic data. The chapter begins by covering the basics of ultrasound, starting with an a-scan. Chapter Two presents methods for temperature monitoring that employ ultrasound, including a variety of mathematically

complex reconstruction algorithms. Material characterization and monitoring through ultrasound is addressed in Chapter Two, covering food, composites, and locating defects. The chapter ends with a discussion of how the literature is applicable to the research done in conjunction with this thesis.

Chapter Three covers the experimentation and data processing done for this thesis. Beginning with ultrasonic theory, the chapter introduces and explains such concepts as beam spread, through-transmission, identifying time of flight of an ultrasonic signal, material attenuation, and acoustic impedance. The wax is characterized using isothermal ultrasonic data measurements to define a master curve relating temperature and speed of sound. Differential scanning calorimetry (DSC) is used to further characterize the wax and its thermal response, as well as the range of temperatures over which melting occurs. The experimental set-up is shown in pictures and diagrams and is explained in detail, followed by an explanation of the ultrasonic data collection process using LabVIEW, and the steps taken to analyze that data using MATLAB. The internal thermocouples, used to validate the ultrasonic results, are also discussed in Chapter Three, as are the external thermocouples, used to establish the boundary conditions for the estimated temperature profile.

The penultimate chapter is an in-depth explanation of a singular data-set analyzed for this thesis. Chapter Four discusses the particular features of this test, which begins with solid wax. Noisy data must be processed and accounted for, as is typical in a highly attenuative material. The steps taken to generate smooth time of flight and speed of sound curves are explained in detail in this chapter. The chapter concludes with a comparison of

the results from ultrasonic data against the temperatures recorded by the internal thermocouples.

This thesis concludes that ultrasonic measurement of 2D temperature and phase is not only possible, but can be accomplished with relatively simple mathematic processes. The results show that the characterized internal temperature state is sensitive to the associated error, and the approximated 2D temperature state of the wax, based on the ultrasonic data, has a typical variation of 3-5°C from the 2D temperature state based on the internal thermocouples. Finally, there is discussion of future work with a phase changing material which exhibits markedly different thermal behavior.

## CHAPTER TWO

### Literature Review

#### *2.1. Introduction*

This chapter discusses the basics of ultrasound and ultrasound techniques, as well as previous research conducted around ultrasound as a means of monitoring temperature and material properties. Ultrasound has a wide range of applicability and is used across many industries for non-destructive evaluation. Temperature is one of the key parameters in thermodynamic systems, and ultrasound has been studied as a means of temperature measurement from as far back as 1873, when Alfred Mayer published a study detailing his development of an acoustic pyrometer [1–4]. The time of flight of an ultrasonic signal, and its relation to the speed of sound, can be used to reconstruct information from a system which may have multiple possibilities for temperature profiles based on the known variables. While bulk temperature, the average temperature across an ultrasound path, may be found using only the time of flight and distance the signal travels, in 1985 Green suggested a deconvolution technique where temperature distribution is represented by a Fourier series [5]. The method used can be considered a precursor to the myriad of techniques studied and tested in the decades since, most methods map temperature based on ultrasonic paths and the time of flight (TOF) of the signals.

With multiple transducers and acoustic paths, reconstruction algorithms of many types have been developed. Bramanti et al. designed a procedure using ultrasound for a specific experiment with a power plant boiler to capture the internal temperature [6]. Least square method was compared to radial basis function approximation and singular

value decomposition by Jia et al. [7]. Shen et al. made use of the Markov radial basis approximation and singular value decomposition [8]. Fujii and Zhang employed the linear-interpolation method [9]. The inverse method was used by Schmidt et al. [10]. Zhu et al. studied both extrapolated filtered back projection (FBP) and computerized tomography (CT) for reconstruction [11]. Each of these methods attempted to reconstruct temperature data from ultrasonic signals.

Ultrasound has also been studied for use in material characterization and monitoring. McClements and Gunasekaran identified many areas of use for ultrasound in the food and beverage processing industry [12]. Gregg studied baking chocolate as well as wax, and identified similarities in their melting behavior [13]. Ultrasonic technology has also been used to identify defects in composite parts without the need for destructive evaluation [14]. In composite parts, resin curing can be monitored using ultrasound, as shown by Tuziuti et al., Lionetto et al., Lionetto and Maffezoli, and Samet et al. [15–18]. The ability to monitor in-situ curing of thermosets can reduce process time and improve efficiency. The phase change undergone by the wax has similar characteristics to thermoset curing, and the techniques used in this research could be applied to in-situ cure monitoring.

The wax studied in this thesis has heating and cooling characteristics which resemble some polymer behavior. Polymer processing requires control over the temperature of the polymers for melting, stability, viscosity, and to prevent degradation of the material [19]. While thermocouples and infrared are common methods for temperature monitoring, Brown et al. studied ultrasound transducers which could be used in-line and provide data in real time. Ning et al. examined the effects of nozzle

temperature on the tensile properties of carbon fiber reinforced polymer (CFRP) parts additively manufactured using fused filament fabrication (FFF) [20]. A two-dimensional temperature map, as shown in Chapter Four, could increase the strength and precision of polymer parts created through injection molding, large area additive manufacturing, and more.

Polymers like PMMA and PEEK are used as buffer-rod materials, affixed to ultrasound transducers in an ultrasonic pulse-echo system. Carlson et al. presented a method for measuring speed of sound, acoustic attenuation, and density of buffer-rod materials [21]. They determined that the values of those parameters depended upon the temperature of the material as well as the ultrasound frequency used. Since these parameters change based on both temperature of the material and ultrasound frequency of the transducer, results dependent on standard values for attenuation or density may have more error than previously supposed.

This thesis builds on the work done by previous researchers Gregg, Stair, and Jost, who studies soy-based wax along with other materials [13,22,23]. Jost's approach to the temperature and speed of sound curve for the soy-based wax is important for the mathematical reconstruction of temperature along an ultrasonic path, particularly in materials where the relationship between temperature and SOS is not linear.

## *2.2 Ultrasonic Basics*

Ultrasonic waves are characterized by amplitude, frequency, wavelength, and attenuation. For 1D waves in a fluid medium without attenuation, the ultrasonic velocity is related to both wavelength and frequency ( $c = \lambda f$ ) (see e.g. [24]). This assumes no viscoelastic damping or temperature dependence. The bulk velocity can be measured by

the time it takes a wave to travel a known distance ( $\tilde{c} = d/t$ ). The representation for the speed of sound may not necessarily correlate to the speed of sound defined in terms of frequency (see e.g. [25]), but in this research,  $\tilde{c} = c$  is assumed. McClements and Gunasekaran write that in materials which have low attenuation, the ultrasonic velocity is simply related to two physical properties: density and elastic modulus [12] as shown in equation 2.1.

$$1/c^2 = \rho/E \quad (2.1)$$

Although lower density will increase speed of sound, the elastic modulus controls the equation. In gases, the ultrasound velocity,  $c$ , can be related to the square root of temperature by

$$c = B\sqrt{T} \quad (2.2)$$

where  $B$  is a constant coefficient dependent upon the universal gas constant, and ratio and average molecular weight of the specific gas [6–8,26]. In isotropic solids, Young's modulus, shear modulus, bulk modulus, and Poisson ratio may all be found using a material of known density and the longitudinal and shear wave speeds in that material [27]. These relationships between the speed of sound and other material properties makes ultrasound a broad and useful tool for many different scenarios.

Visually, ultrasonic waves are commonly represented by the variation of amplitude, or signal voltage, over time; this is known as an A-scan, shown in Figure 2.1 (see e.g. [25]).

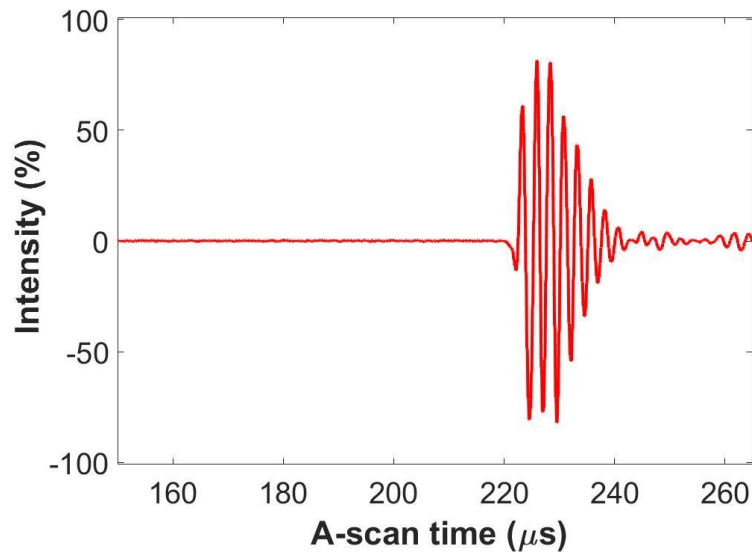


Figure 2.1. A-scan.

An a-scan can be acquired using a single ultrasonic transducer and the pulse-echo method, where the ultrasonic signal passes through the material, reflects off any material boundaries, and then reflects to the transducer which transmitted the signal. Another method of obtaining an a-scan is to use through-transmission, which requires two ultrasonic transducers. One transducer transmits the ultrasonic signal, which passes through the material and is received by the second transducer. Both methods are shown in Figure 2.2. In this research, the through-transmission method is used for the experiments discussed in later chapters.

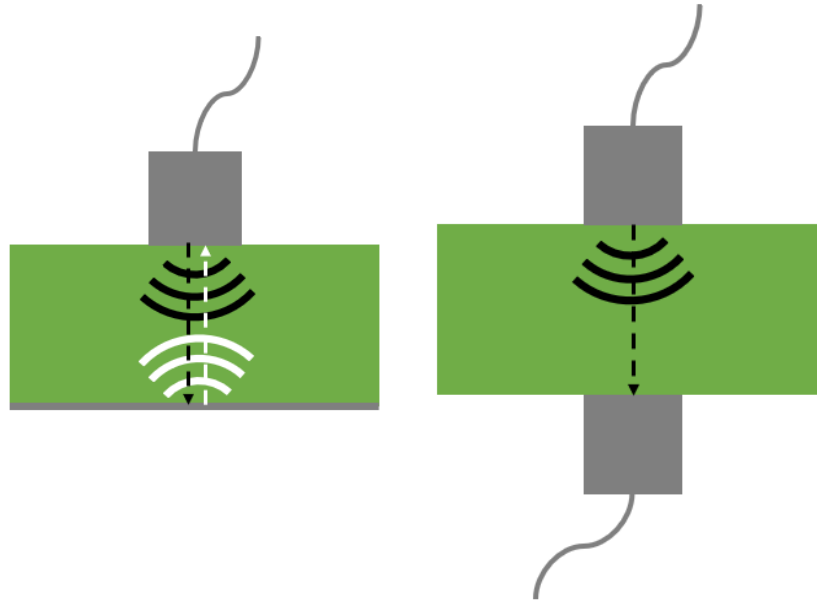


Figure 2.2. Pulse-echo (left) and through-transmission (right) transducer setup.

### *2.3 Ultrasound in Material Characterization and Monitoring*

Ultrasound can be used for applications beyond temperature measurement. With polymers, ultrasound has been used for imaging fillers within a polymer flow, and measuring elastic constants such as Poisson ratio and Young's modulus [27,28]. The ability to detect bubbles in a viscous fluid and measure the velocity has applications for composite parts, as does monitoring the cure of thermosetting resin and automated detection of internal defects [14,16–18,29]. In the food industry, ultrasound has been used for characterization of physiochemical properties, including composition and particle size [12].

Ultrasound tomography was studied by Halmen et al. for use in imaging local filler distribution inside plastic melts [28]. Ultrasound process tomography (USPT) is a technology developed for inline imaging of melt during polymer rod extrusion, and can be directly integrated into the manufacturing process. A sensor ring containing 40

transducers was designed to the geometry of the rods being extruded and fit onto the melt channel just before the polymer exits the shaping nozzle. Two types of fillers were used in a basic polypropylene polymer. To examine the local filler distribution of the rods with the tested geometry required a balance between transducer size, opening angle, and the number of transducers. The results from the experiment have adequate image quality only in the middle part of the reconstruction due to the experimental setup used. The method was shown to be sound, but there are many parameters which can affect the results. In the present research, a similar ring of eight transducers surround the test cell to perform our USPT.

In solid polymers, the elastic constants of a material can be found using the density of the material and the speed of shear and longitudinal waves [27]. The tests performed by Rae and Brown on six types of polymers were all done at ambient temperature, and on samples 3-19 mm thick. Although the attenuation in the thicker samples was significantly greater, the uncertainty associated with the wave speed measurements was lower. The researchers obtained the Poisson ratio, Young's modulus, shear modulus, and bulk modulus from their ultrasonic testing, and recommend using samples 9 mm thick or greater.

In composite materials, bubbles which form during resin transfer molding (RTM) can weaken the matrix material, and thus the end-user material. Samet et al. designed a method for detecting macro-bubbles in a flow of viscous fluid using an ultrasonic phased array transducer [18]. Viscous fluid is pumped through a channel, where the back wall is aluminum and the front wall is glass, and the phased array transducer is in contact with the glass wall. Using ultrasonic signals which are focused by the glass and then reflected

off the aluminum, the velocity of the macro bubbles was measured, and then the bubble quantities and sizes were observed. The measurements were validated using video from the experiment, as well as theoretical results.

Maffezzoli et al. published a paper in 1999 examining the use of ultrasonic velocity, as a function of bulk longitudinal modulus, to monitor resin during curing. Ultrasonic velocity changes in conjunction with the mechanical stiffness of the resin, making it an interesting parameter to track [29]. Isothermal and non-isothermal experiments were performed on resin samples. For comparison and validation, cure degree was monitored by using a DSC at the same temperatures for isothermal conditions.

Lionetto and Maffezzoli underscore the importance of cure monitoring for ensuring manufacturing reliability and reproducibility of composite parts [17]. Other techniques applied to cure monitoring, such as differential scanning calorimetry (DSC), dielectric analysis (DEA), dynamic mechanical thermal analysis (DMTA), and near infrared spectroscopy (NIR), are not suitable for broad industrial application, and Sia et al. determined that DSC and DMTA did not fully characterize the polymer when the degree of cure was above 80% [30]. The experimental work done by Lionetto and Maffezzoli was to determine the reliability of ultrasonic dynamic analysis (UDMA) to monitor the curing process of thermosetting resins, and to quantify the degree of cure more precisely than the standard DSC technique. Time of flight and attenuation of the ultrasonic signal are both used to evaluate the curing process. The researchers showed that non-contact transducers produced similar results to contact transducers. Air-coupled ultrasonics, using the pitch-catch method with two transducers, were also studied by

Lionetto et al. to monitor the curing of unsaturated polyester resin [16]. Because the thermoset is undergoing a chemical reaction, the elastic and acoustic properties change during the curing process. The lack of physical contact required, and the need to access only one side of the tested material are both advantages for on-line quality control.

Non-destructive techniques are important in the detection of internal defect in composite materials, offering more than visual analysis without damaging the material. D’Orazio et al. studied the automation of internal defect detection in composites [14]. Researchers worked to train three neural networks to recognize defects using an example 48 plies thick. When testing the neural networks against parts with known defects, increasing the number of plies from 48 to 64 and then to 128 successively lowered the percentage of points correctly identified, which the researchers posited was due to the increased thickness compared to the training sample. The method used in Chapter Three to generate the wax time of flight and speed of sounds curves require user input, but neural networks may be pursued in future to identify the ultrasonic signal onset.

Neural networks have been studied for use in the oil and gas industry as well. Figueiredo et al. studied the ability of neural networks to identify flow pattern and measure gas volume fraction based on ultrasonic data [31]. They found that the gas volume fraction could be measured with less than 20% uncertainty for a multiphase flow of glass beads, air, and glass beads (intended to simulate sand inside oil flow). The training of neural networks to identify between phases is relevant to the two-phase experiments in this thesis.

The food industry has used ultrasound for decades. McClements and Gunasekaran list four categories of application for ultrasound in the characterization of

physicochemical properties of food materials: composition, phase transitions, particle size, and miscellaneous [12]. In each of these categories, the ultrasonic velocity is the property measured most frequently. For materials with low attenuation, there is a simple relationship between ultrasonic velocity, density, and elastic modulus. Level detection, extraneous matter detection, temperature measurement, flow rate measurement, composition identification, and particle size determination are a few of the specific applications of ultrasound for use in food and drink processing. Certain fatty materials require a specific ratio of solid to liquid fat over a range of temperatures. While attenuation can also be used to determine the solid fat content (SFC), the ultrasonic velocity is less sensitive to the structure of the fat crystals and can be measured with more accuracy. Häupler et al. studied the in situ characterization of chocolate using ultrasonics, using attenuation and speed of sound to differentiate between the crystallization and temper of chocolates with different solid fat contents [32]. Such a method has potential for identifying phase change, cure, or crystallinity in amorphous materials, such as wax, or semi-crystalline materials.

#### *2.4 Ultrasound in Temperature Monitoring*

Mayer's study of acoustic pyrometry used sound waves in a metal tube filled with air. As the air temperature changed, the wavelengths observed in the tube changed, leading to the conclusion that the speed of sound was changing with temperature [4]. This laid the groundwork for using acoustics like ultrasound to monitor temperature in a wide range of industries. Temperature monitoring using ultrasound has applications in food processing, polymer processing, additive manufacturing, and more. As Schmidt et al. pointed out, "the vast majority of temperature sensing methodologies require that

sensors be placed near, or have access to the location where the thermal measurement is required” [10]. For applications that do not fit these criteria, as well as applications which expose sensors to harsh or corrosive environments, ultrasound provides a viable alternative [6].

The time of flight in a material, such as an amorphous wax, has been shown to be a function of temperature (see [13,22,23]). The bulk speed of sound (SOS) is defined in terms of the time of flight (TOF) and distance traveled, as shown by equation 2.3, where  $c$  is the effective bulk speed of sound,  $d$  is the distance traveled, and  $t$  is the time required to travel the distance  $d$  (see, e.g. [12]).

$$c = d/t \quad (2.3)$$

At a known temperature, a simple through transmission or pulse-echo transmission from an ultrasonic transducer can be used to measure the time required for the ultrasonic signal to travel through a sample of known thickness. From this information, the speed of sound can be directly calculated for the material at a given temperature by assuming the acoustic medium is at a homogeneous temperature state.

#### 2.4.1 *Temperature in Foods*

This relationship between the speed of sound and the temperature has been studied for a wide variety of materials. Oliveira et al. used a pulse-echo technique to measure the temperature of a soybean oil sample [33]. A cell containing the sample was immersed in a thermal bath for temperature control, and a K-type thermocouple was used to validate the temperature. After performing five tests at each set temperature, using intervals of 5 degrees Celsius, researchers approximated a linear regression fit of the data for speed of sound as a function of temperature. Beef was also found to have a linear

regression fit between temperature and SOS, as shown by Hægström and Luukkala [34]. After frying the beef on both sides using a pan at 198°C, a 50mm disc was removed from the beef; this disc contained the thermocouple sensor used to verify the temperature measurements garnered from ultrasound. The beef discs were then placed between transducers and allowed to cool from 75-45°C, during which time the thermocouple temperature was recorded simultaneously with ultrasonic measurements. The relationship between the product of sound velocity and signal amplitude is linear with the change in temperature, and a linear regression was created using the measured data. In this way, Hægström and Luukkala showed it possible to measure the internal temperature of the beef during the roasting process.

#### 2.4.2 *Temperature in Polymers*

The mechanical properties of additively manufactured parts are known to vary based on the processing parameters, such as flow rate, temperature, and, for fiber reinforced composite parts, the fiber orientation (see e.g. [35]). In fused deposition modeling, nozzle temperature refers to the working temperature of the nozzle. The polymer melt non-Newtonian viscosity is strongly correlated to the polymer melt's temperature state (see e.g. [36]). Ning et al. studied the resultant tensile properties of carbon fiber reinforced polymer (CFRP) composite specimens as four different process parameters (raster angle, infill speed, nozzle temperature, and layer thickness) were varied [20]. The tensile properties measured all showed an increase, followed by a decrease, as nozzle temperature was increased from 200°C to 240°C. The poorer results at lower temperatures were hypothesized to be caused by weakened bonding between interlayers and rasters, while at higher temperatures the CFRP composite was more

porous. Real-time monitoring of the CFRP inside the nozzle, using embedded ultrasonic transducers, could offer a way to ensure more reliable tensile properties from additively manufactured parts. Praher et al. studied tomography using the speed of sound along different paths within a polymer melt, based on the temperature dependence of speed of sound within the material. A simultaneous iterative construction technique took into account speed of sound, temperature, and pressure to better approximate temperature during the injection molding process [37]. Hopmann and Wipperfurth used 20 ultrasound transducers around a cylindrical mold to prove the feasibility of measuring the temperature within a mold, non-invasively [38]. The work in this thesis is similar to the studies done by both Praher and Hopmann, however moves a step beyond by successfully accounting for the phase change that occurs during melt and cooling.

Brown et al. provides a thorough overview of the importance of melt temperature for polymer extrusions, including both rheology and stability [19]. The experimental setup to measure the in-line melt temperature utilized a pair of ultrasound transducers mounted opposite each other, similar to the approach used in this thesis, with the melt flow passing between them. In the setup by Brown et al., the transducers are flush with the melt flow and do not penetrate it, thus ensuring a non-invasive measurement. Brown et al. used the ultrasound data to approximate bulk temperature and suggested that it may be possible narrow the choices of temperature profiles which might represent the melt flow.

### *2.4.3 Temperature in Gas*

Power plant boilers can develop hot spots, and require internal temperature maps to safely monitor the internal temperature and conditions. Optical techniques can be used

in some circumstances for surface measurements, but not all environments are feasible for that technology. In 1996, Bramantic et al. published a paper discussing acoustic pyrometry as a method of mapping the temperature inside power plant boilers. The methods proposed in [6] took advantage of preexisting relationships between the speed of sound and temperature for an ideal gas, as shown in equation 2.2. The methods work to reconstruct the temperature profile by fitting it to data based on the time of flight of acoustic signals. Earlier studies with gas and ultrasound even refined the universal gas constant [2,3], confirming the level of precision possible with ultrasonic techniques.

#### *2.4.4 Temperature in Solid Materials*

In recent years, the internal material state and temperature of select solid materials have been characterized using ultrasound. Jia et al. studied temperature in a model gasifier refractory constructed from Portland Type I/II cement [39]. The goal of the Jia et al. study was to determine if the speed of sound in the refractory itself is temperature dependent, and if it is possible to create partial internal reflections along the propagation path. These partial internal reflection function similar to a waveguide, which has built-in physical features at specified intervals. The features of a waveguide reflect a portion of the signal, while allowing the rest to continue propagating through the waveguide. The reflected signals vary in time of flight with temperature, making it possible to determine the temperature gradient along a waveguide. To determine the difference in the TOF at different temperatures, the researchers chose to use cross-correlation between the echoes of the initial waveform to discern the  $\Delta$ TOF. The temperatures based on ultrasonic data were approximately 10°C hotter than the thermocouple temperatures, although they followed the same trends as the thermocouples. Thermal expansion within the cement

used is cited as a likely cause for the discrepancy. The authors suggested that if the experiments were to be scaled up, the thermal expansion and changing geometry of the cement would need to be taken into consideration to ensure accuracy of results. Chen et al. created a waveguide from a steel rod with stainless steel cladding, and used piezoelectric transducers to measure the temperature along the rod [40]. Waveguides are a frequently used method for temperature determination in solids.

In 2016, Jia published a paper with a different group of researchers, this time to specifically measure the temperature distribution in solids [41]. The method employed for this study required a structured ultrasound propagation path with echogenic features which create partial reflections at known locations. The change in TOF from each of these known locations, when used together, provide data which can be interpreted as the temperature distribution along the propagation path. The successful experiment tested a range of temperatures, from 0°C to an excess of 1000°C in a rod of high purity alumina, and results were validated with thermocouples. Schmidt et al. studied similar effects in the barrel of large caliber weapons using physical discontinuities on the remote surface of the structure [10], and found that the data measured was in good agreement with values based on empirical references.

#### *2.4.5 Temperature in Non-Homogeneous Materials*

Not all materials are homogeneous and without obstacles which might interfere with measurement. Temperature distribution in a material that contains an acoustic obstacle was studied by Fujii and Zhang [9]. They studied an agar-gel, 98% water by mass, and heated it using a platinum wire. The sample and a pair of ultrasonic transducers were immersed in a water bath. The transducers were mounted from a fixture that moved

and rotated, allowing for a full scan of the agar-gel sample. The second test they performed was conducted with an acrylic cylinder placed off-center inside the agar-gel sample. The time of flight measurements were used to create a temperature profile inside the agar-gel and the acrylic cylinder. For comparison, the measured temperatures from ultrasound were compared against theoretical temperatures from the heat conduction equation with a constant heat flux. In the homogeneous setup, measured and theoretical temperature profiles were within 0.1K of each other. The exception was where the gradient was very large near the platinum wire. In the setup with the acrylic cylinder, the agar-gel temperatures measured agreed within 0.2K with the theoretical temperatures, except in the areas directly near the platinum wire and acrylic cylinder.

#### *2.4.6 Temperature in Wax*

The work in this thesis is a continuation of previous research done by Gregg, Stair, and Jost to measure temperature and phase using ultrasound [13,22,23]. Gregg studied soy-based candle wax, base paraffin wax, and baking chocolate. Those experiments heated the material from one end to another of a rectangular container to the other, forcing heat flow to be unidirectional. Ultrasonic transducers using through-transmission captured time of flight across the materials as they heated and cooled, including across phase changes, and the time of flight was used to calculate speed of sound. The relationship between speed of sound and the material temperature was characterized by Gregg, and the approximate temperature calculated based on the ultrasonic data. Stair also used a soy-based wax, in addition to studying a machinist wax, with an experimental set-up nearly identical to Gregg's. One of Stair's significant contributions to this direction of research was to identify the non-linear relationship

between speed of sound and temperature for the soy-based wax. Jost's research also used the soy-based wax, and found that the relationship between speed of sound and temperature could be expressed as a bi-linear, continuous function. The current research uses the same approach for another type of wax.

Jost studied additional ways to identify when the phase change occurred in the soy-based wax: a-scan shape, speed of sound, electrical gain, and frequency decomposition. Using the same type of rectangular experimental geometry as Gregg and Stair, the phase change boundary crosses each transducer face. A-scan shape was used to visually inspect the signal and determine if the phase change was occurring, and which phase(s) were covering the transducer face. Speed of sound transitioned sharply between liquid and solid during this experiment, and Jost identified the phase change based on the speed of sound over time. The electrical gain required to maintain the a-scan signal at the appropriate saturation was observed to change with phase and temperature, reaching a local maximum at the transition from solid to liquid. Jost also observed that the frequency spectra of an a-scan changed significantly if the signal passed through solid vs liquid wax. This change in spectra was used to identify the phase change of the soy-based wax.

Jost's research moved beyond a rectangular geometry and into a cylindrical geometry, which was a scaled-down version of the experimental set-up described in Chapter Three. While the temperature vs speed of sound curve was approximated bi-linearly, the temperature and phase curve was approximated by Jost as a step function, changing from solid to liquid at the melt temperature. Jost created approximate representations of the physical wax state across a 2D plane of the cylindrical geometry, which was a direct precursor to the research in this thesis.

### *2.5 Ultrasound and Current Research*

It is evident that ultrasound has a wide range of applications for non-invasive and non-destructive temperature and material monitoring, particularly in applications when other methods are undesirable or impossible. The purpose of this research is to study and assess the use of ultrasound techniques to establish time of flight and speed of sound [24] as a means of monitoring the temperature [5–10,19,26,27,33,34,39,41] and phase change [12,17,29] of a material. This research uses wax as the material of interest, due to the stability and repeatability of testing with it. The thermal response of wax is similar to that of polymers, softening to a gel-like state prior to achieving full melt, and these experiments could also be performed on polymers [15,19,20,27,28] or on other materials [12,33,34].

## CHAPTER THREE

### Experimentation and Data Processing

This chapter introduces the basics of the ultrasonic theory used, the correlation between sound and temperature, and how those two distinct physical quantities will be correlated in this thesis. The chapter provides a discussion on material characterization, the equipment used, discussion on the experimental setup, testing protocol, and data analysis. All testing is performed on CBL-125, a Candlewic wax, chosen because of its melt similarity to that of a classical thermoplastic undergoing melting. The CBL-125 is characterized through differential scanning calorimetry and isothermal tests to quantify the speed of sound.

#### *3.1. Ultrasonic Theory*

In ultrasonic testing electric signals are converted to mechanical vibrations, which create ultrasonic pulses that travel through a medium before being received by another (or sometimes the same) transducer where the acoustic waves are converted back to an electrical voltage [24]. In most acoustic transducers, the active element is a piezoelectric ceramic, sometimes referred to as a piezoelectric crystal. Piezoelectric materials create electrical charges when deformed, and this deformation comes in the form of an ultrasonic sound wave inducing a pressure on the surface of ultrasonic transducers [42]. The sound from a piezoelectric transducer emanates from most of the surface, rather than a single point. Round transducers, as used in this research, are also referred to as piston transducers because the shape of the sound field resembles a that of a cylinder. However,

the sound field is not a perfect cylinder, as the wave begins to spread in the transverse direction of motion, a phenomenon given the term beam spread in the industry. A common formula used to calculate the beam divergence, half the beam spread, is equation 3.1 (see e.g. [24]).

$$\sin \theta = 1.2 \frac{V}{DF} \quad (3.1)$$

Where  $\theta$  is the beam divergence in radians, identified as the angle from centerline to where the signal is at half strength,  $V$  is the sound velocity (cm/s),  $D$  is transducer diameter (cm), and  $F$  is the frequency of the transducer (Hz) [24]. This is shown in Figure 3.1.

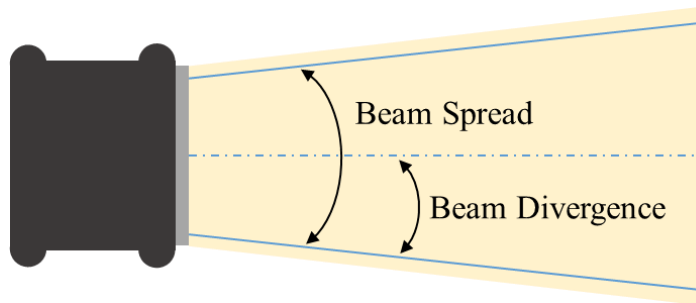


Figure 3.1. Transducer and beam divergence.

Transducers create the ultrasonic energy which propagates through a medium until it reaches a receiving transducer or is reflected and received by the initial transducer. A device known as a pulsar/receiver is used to control transducers, producing the necessary voltage to create the ultrasonic signal, and then processing the electrical signal generated by the receiving transducer.

When a transducer receives an ultrasonic wave and converts the wave into an electrical signal, the wave is often displayed on an oscilloscope in a form termed an a-

scan. This may be done on a physical oscilloscope or may be archived on a computer and post-processed. Figure 3.2 offers a flow chart of the process.

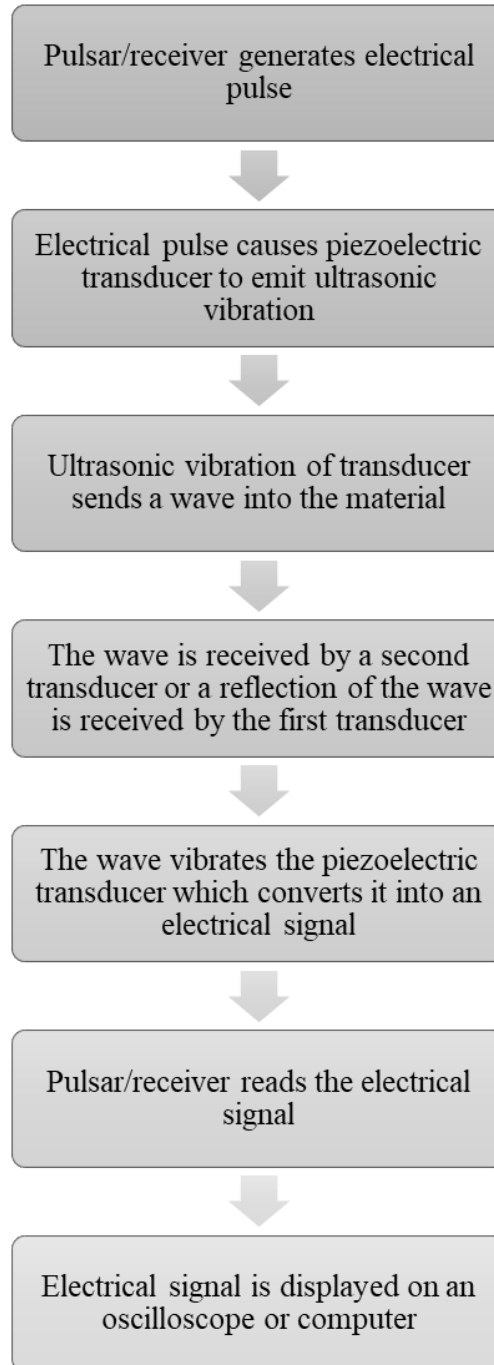


Figure 3.2. Flowchart of through-transmission ultrasonic testing.

A-scans are displayed as the amount of ultrasonic energy received over time. A basic a-scan is shown in Figure 3.3 of a. A-scans represent a single point or ultrasonic path taken at a single moment in time. Depending on the known parameters, the a-scan time of flight when a signal is detected can be used to measure the speed of sound or, if the speed of sound is known, the dimensions of a sample. As discussed in Chapter 2, the relationship between time of flight, distance traveled, and speed of sound is represented by equation 2.3.

$$c = d/t \quad (2.3)$$

The speed of sound of a material, also called the wave velocity, and in this thesis will be reported in meters per second.

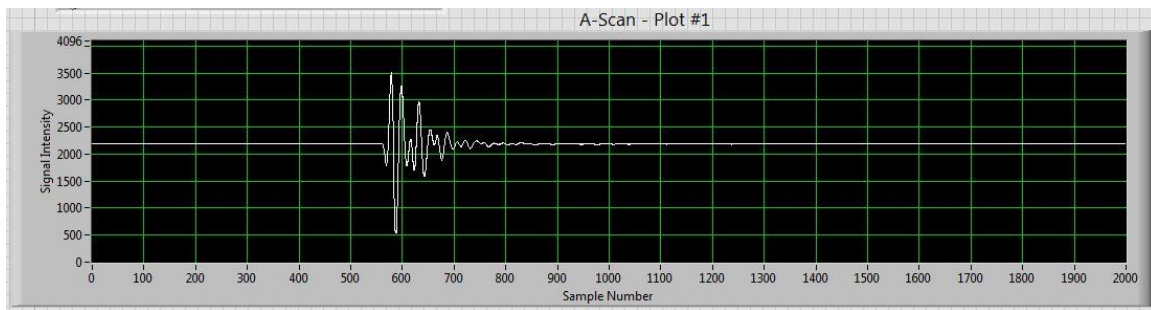


Figure 3.3. A-scan as displayed by LabVIEW.

There are several methods for determining the time of flight of an ultrasonic signal, sometimes called time of arrival (TOA), time delay estimate (TDE), or time delay of arrival (TDOA). Three methods studied by Svilainis are based on peak location, zero crossing, or arbitrary level crossing [43]. An illustration of these methods is shown in Figure 3.4.

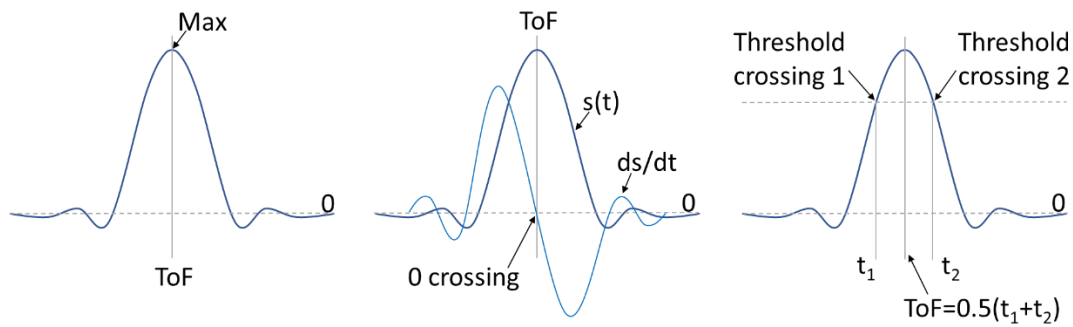


Figure 3.4. Methods of determining time of flight.

Using the peak of the signal to determine time of flight poses problems with noisy data or if a signal has a complicated shape. Zero crossing takes the signal derivative and locates the zero crossing of that derivative signal; however, this requires a trigger to ensure that the correct zero crossing is chosen, as there can be many peaks in a single ultrasonic signal. Arbitrary level crossing uses a pre-established threshold and determines where the signal crosses the threshold. This method can handle complex signals, however the signal can be missed if the threshold level is too high, or additional peaks could be captured if the threshold is too low [43]. The research on this current project has used a custom method, similar to arbitrary level crossing. In a bid to capture the initial onset of the signal, a detection threshold is set at 30% of the maximum normalized signal intensity, as shown in Figure 3.5.

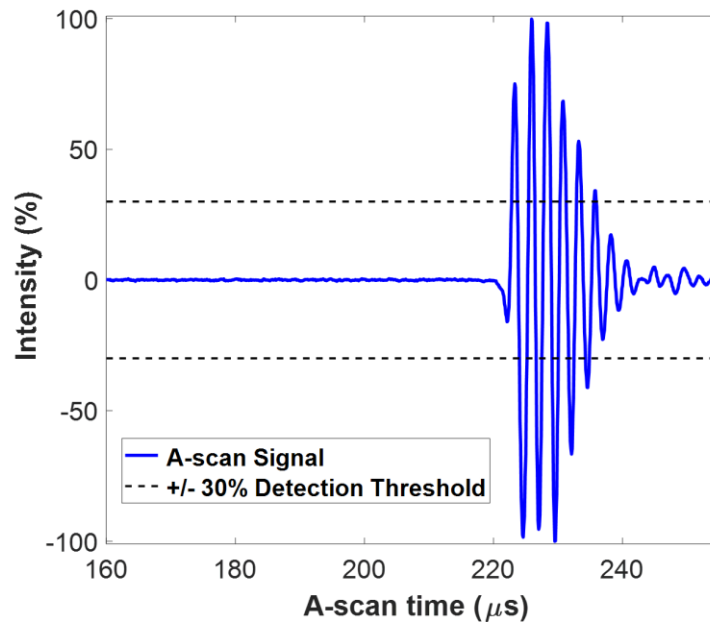


Figure 3.5. Normalized a-scan and  $\pm 30\%$  detection threshold.

Time of flight estimation techniques can be used regardless of the ultrasonic method used. There are three methods primarily used in ultrasonic non-destructive evaluation (NDE): pulse-echo, pitch-catch, and through transmission. As shown in Figure 3.6, pulse echo uses a single transducer to both transmit and receive the ultrasonic signal. Pulse-echo only requires access to a single side of a part or material, and it is often used with composite parts (see e.g. [17]). Research with waveguides uses pulse-echo, and it can be used for speed of sound estimations as well [33,41]. The pitch-catch method uses a pair of transducers on the same side of a part or material, and the signal is sent through the part at an angle by the first transducer, so that the second can receive it [16]. This project uses through-transmission, which utilizes a pair of transducers, one on each side of the material or part as depicted in Figure 3.6. Through-transmission has been in use for inline monitoring of polymer melts and extrusion processes (see e.g. [19]).

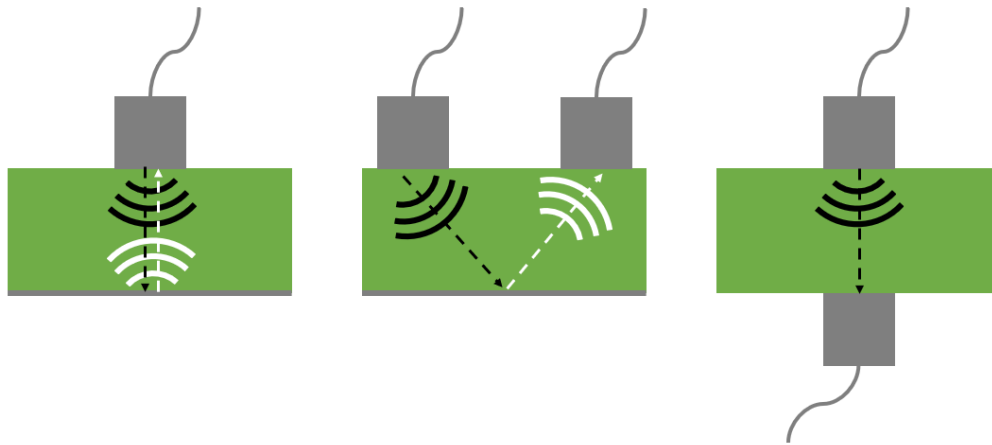


Figure 3.6. Ultrasonic testing methods: Pulse-echo (left), pitch-catch (center), through-transmission (right).

Ultrasonic signals traveling through any material are subject to attenuation, the decay of the signal energy due to scattering and absorption. The current research uses custom LabVIEW VI's to monitor the signal intensity, and to automatically adjust the gain of the signal to maintain a certain threshold. The amplitude, or signal intensity, of a wave is reduced the longer the distance traveled as:

$$A = A_0 e^{-\alpha z} \quad (3.2)$$

Where  $A$  is the amplitude of the received wave,  $A_0$  is the amplitude expected without any signal loss or reduction,  $z$  is the distance the signal has traveled, and  $\alpha$  is the attenuation coefficient. The signal amplitude of the wax used in these experiments was observed to change with temperature, but no further quantification was performed other than to adjust the signal gain throughout the experiment.

### 3.2. Material Characterization

This research uses a wax, CBL-125, produced by the Candlewic Company. It is a paraffin wax with proprietary additives included. Paraffin wax is made of straight chain hydrocarbons [44]. This wax has a low coefficient of thermal expansion and is designed to completely fill glass candle containers while maintaining contact with the interior surface of the glass throughout the solidification process. CBL-125 is highly attenuative, and that attenuation change is a function of the temperature of the wax. The thermal transition during melting and cooling of CBL-125 is similar to that of a thermoplastic and, as the later DSC curves will show, is representative of a polymer transitioning from melt to a rubbery material above the glass transition temperature.

#### 3.2.1 Equipment Used

A US Ultratek EUT3160 pulsar/receiver, shown in Figure 3.7, sends and receives the electrical signals to and from 1-inch diameter, 0.5 MHz transducers. These transducers are sold by Olympus which acquired Panametrics (Figure 3.8). Using through-transmission, a total of eight channels are possible on the equipment available for this research.



Figure 3.7. EUT3160 Pulsar/receiver.



Figure 3.8. Olympus and Panametrics transducers.

Transducers are acoustically coupled using a couplant and in this study both EchoPure ultrasonic couplant and Sonotech Ultragel II ultrasonic couplant are used. K-type thermocouples are wired to a Graphtec midi-LOGGER GL820 to record internal and external temperature. The data logger allows up to 100 channels to be monitored simultaneously.

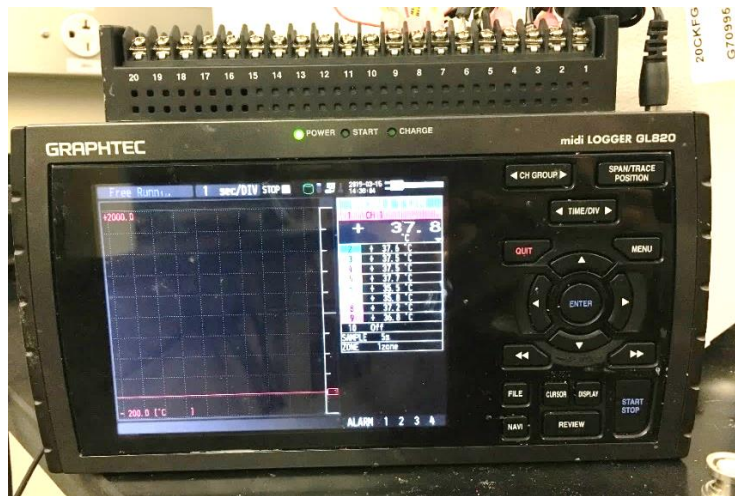


Figure 3.9. Graphtec midiLOGGER GL820.

### 3.2.2 Differential Scanning Calorimetry

The melt transition is characterized using a TA Instruments Q20 Differential Scanning Calorimeter (DSC), shown in Figure 3.10. The DSC records heatflow vs temperature, where the heatflow is related to the energy required to change the temperature of the sample. Multiple 5-15mg samples of CBL-125 are weighed using a TA Instruments Q50 Thermogravimetric Analyzer (TGA), then the sample is placed into the an encapsulated T-zero pan and placed in the DSC. Three cycles of heating are completed. Each cycle begins at  $-20^{\circ}\text{C}$  and is heated to  $120^{\circ}\text{C}$  at  $2^{\circ}\text{C}/\text{min}$ , then to  $-20^{\circ}\text{C}$  at a rate of  $-2^{\circ}\text{C}/\text{min}$ . The first cycle is done to insure the sample is melted and uniformly covers the pan, and thus its data is disregarded in the analysis. Further heating cycles are then completed, and this data analyzed in Figure 3.11 for a 13.91mg sample. As CBL-125 increases in temperature during the heating, the “valley” seen in Figure 3.11 which indicates melting initiates just before  $45^{\circ}\text{C}$ . The greatest inward heat flow occurs at  $46.35^{\circ}\text{C}$ . The DSC curve shows an inflection point at  $50^{\circ}\text{C}$ , which was observed to correlate with the wax changing visually from partially opaque to fully transparent and liquid.

Solidification is much the same for CBL-125, where the transition appears to occur at approximately  $49^{\circ}\text{C}$ , and is completed by  $44^{\circ}\text{C}$ . The DSC results do indicate that melting and solidification occur over the same range for CBL-125. Because this material melts and solidifies over a range of temperatures, as opposed to the instant transition of ice to water, it is difficult to define an exact melt or solidification temperature based on the DSC results, but a range of  $45^{\circ}\text{C}$  to  $50^{\circ}\text{C}$  is identified as the melt and solidification zone.



Figure 3.10. TA Instruments Differential Scanning Calorimeter Q20.

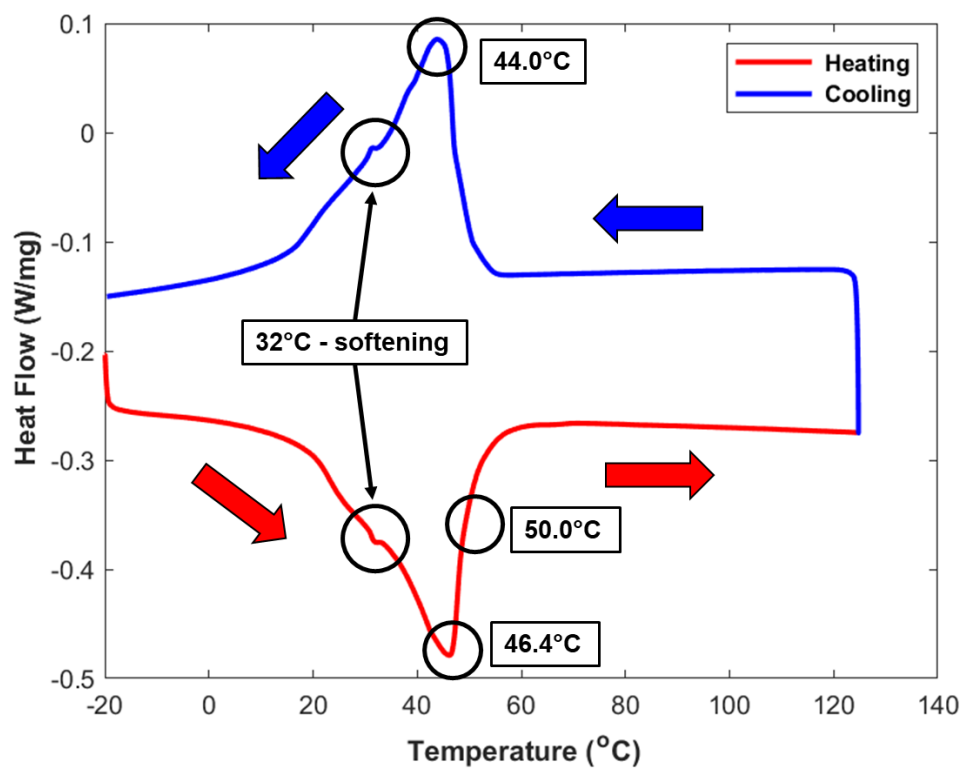


Figure 3.11. DSC curve for CBL-125 at a rate of 2°C/min.

It is interesting to note that a change occurs in the DSC curve at 32°C which corresponds to the onset of softening, a physically observable change when the wax becomes significantly more malleable but is still solid.

### *3.2.3 Isothermal Speed of Sound Tests*

To further characterize CBL-125, the relationship between the speed of sound and temperature is studied. This is done by placing the wax into a container and placing it into a furnace at a fixed temperature until thermal equilibrium is reached, and then the sample is subjected to an ultrasonic wave. This is then repeated over a range of temperatures of interest for later testing. An acrylic container is filled with CBL-125, and 5 k-type thermocouples are inserted into the liquid wax at varying spatial locations (Figure 3.12). The randomized locations of the thermocouples are to ensure the wax is isothermal prior to data collection. The thermal equilibrium tests are performed using a Thermo Precision Compact Oven with an analog control. Two additional k-type thermocouples monitor the air temperature inside the oven, and all seven thermocouples are connected to a GL-820 Midi DataLogger. Observations of the air measurements inside the furnace indicate that this oven model is subject to temperature oscillations as it attempts to reach the set temperature, and even after that temperature has been reached. These oscillations spanned up to 10 degrees Celsius as the air temperature within the oven changed. But due to the larger heat capacity of the wax, these oscillations were never detected in the sample. Testing for the speed of sound measurements was not undertaken until all five internal thermocouples were within 0.5°C of each other. The temperatures of the five internal thermocouples are recorded and their average value used in the data analysis.

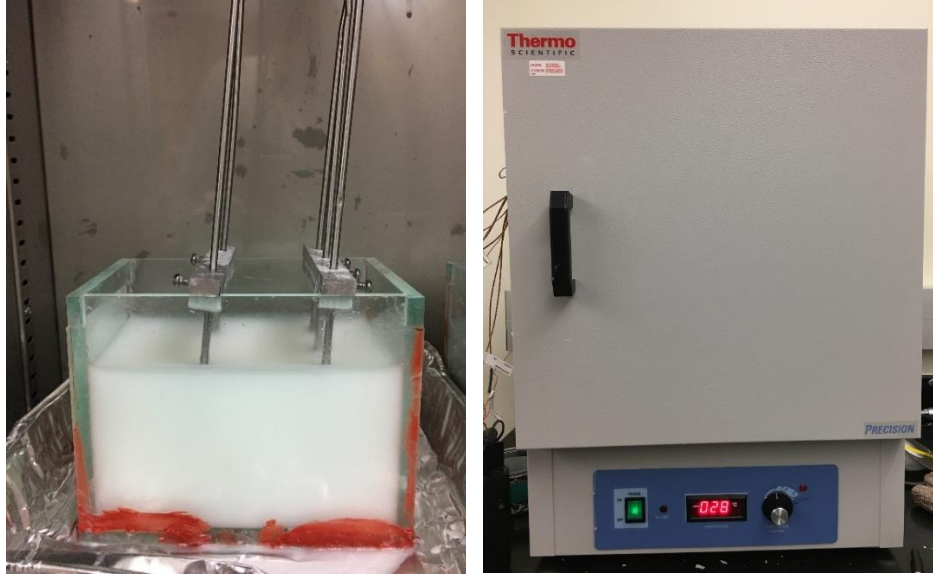


Figure 3.12. CBL-125 with five thermocouples for thermal equilibrium tests (left) and Thermo Scientific Precision Compact Oven (right).

Ultrasonic measurements are taken once thermal equilibrium has been reached. A pair of transducers is used in through-transmission mode, and the ultrasonic signal is sent lengthwise through the wax and container. The transducers are coupled to the surface of the acrylic container with EchoPure ultrasonic couplant and held manually in place until at least 5 clean signals have been captured and recorded by LabVIEW. The stored value of the a-scan is an average of 150 a-scans which occur at the same electrical gain.

The ultrasonic data recorded in these thermal equilibrium tests is processed in MATLAB. The temperature ranges from an ambient temperature of 21°C to 87°C, fully encompassing the melt transition of the wax. During data collection, the electric gain (in dB) required to maintain the signal at the appropriate threshold is recorded.

The time of flight is found using the signal onset time. In this research, it is defined using a detection threshold of  $\pm 30\%$  for the normalized signal intensity. Figure

3.13 shows the onset time of flight for the isothermal experimental setup at 34°C and 61°C. The signal onset occurs at 82.4μs and 97.0μs, respectively.

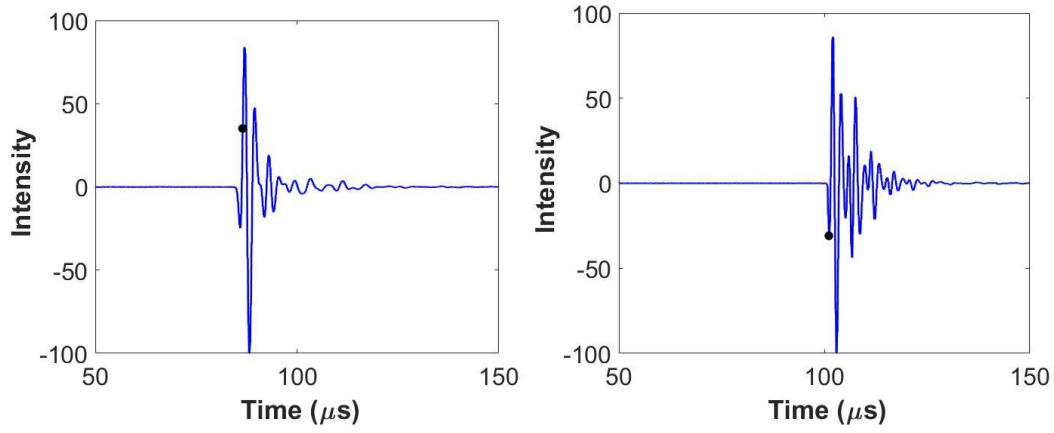


Figure 3.13 Time of flight at 34°C (left) and 61°C (right).

The acrylic container is 137.73mm in length, 87.69mm in width, and with wall thickness,  $th$ , of 5.58mm (Figure 3.14).

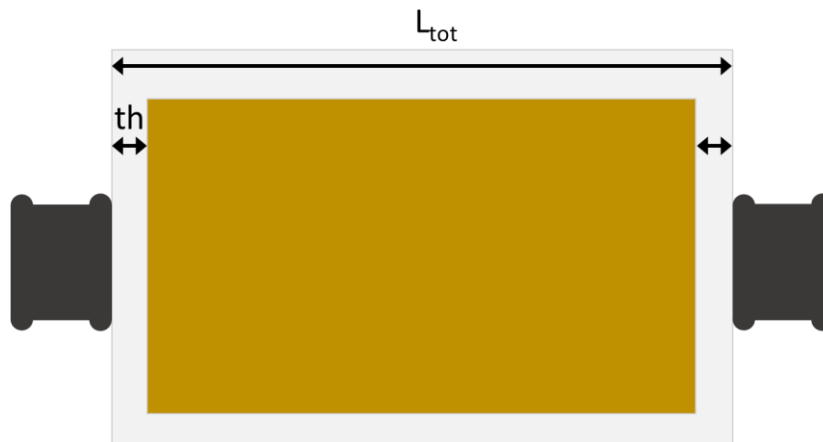


Figure 3.14 Diagram of isothermal wax container.

The speed of sound of acrylic is taken to be a constant 2730m/s [45]. The amount of time the ultrasonic signal spends inside the acrylic is given by equation 3.3.

$$t_{\text{acrylic}} = \frac{2 * th}{\text{SOS}_{\text{acrylic}}} \quad (3.3)$$

The signal time of flight includes the wax and the acrylic, so the time of flight for the material inside the container is the signal time minus the time spent in the acrylic.

$$\text{TOF}_{\text{wax}} = \text{TOF}_{\text{total}} - t_{\text{acrylic}} \quad (3.4)$$

Finally, the bulk speed of sound of the wax inside the container is found by

$$\text{SOS}_{\text{wax,bulk}} = \frac{L_{\text{tot}} - 2 * th}{\text{TOF}_{\text{wax}}} \quad (3.5)$$

Equation 3.5 assumes an isothermal state for the wax inside the container, the temperature of which is measured by the five internal thermocouples.

Once the speed of sound data is tabulated, it is possible to approximate the relationship between speed of sound and temperature using a piecewise, continuous function comprised of two discrete linear polynomials that are optimized to fit the data as shown in Figure 3.15.

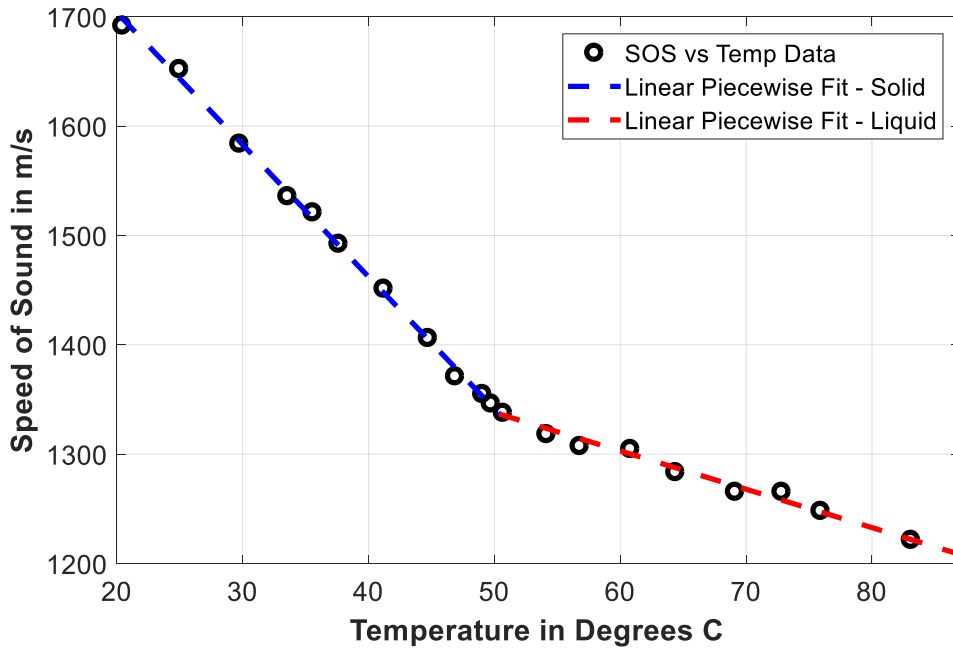


Figure 3.15. CBL-125 Speed of Sound vs Temperature Master Curve.

The temperature measurements, taken with k-type thermocouples, have an associated error which is within the marker size of the data points shown in Figure 3.15, so there are no error bars shown. The equations for these polynomials are given by equation 3.6, where T is temperature in degrees Celsius.

$$\text{SOS} = 1945.3 - 12.076 * T, \quad T < 50.4 \quad (3.6a)$$

$$\text{SOS} = 1513.4 - 3.5064 * T, \quad T > 50.4 \quad (3.6b)$$

Analysis of the fit to the data is most easily understood by examining the R-squared values for the two linear polynomials: at lower temperatures, below 50.4°C, the R-squared value is 0.998; at higher temperatures, above 50.4°C, the R-squared value is 0.988. The intersection of the discrete linear polynomials occurs at 50.4°C, which researchers define as the melt temperature. This melt temperature, also called  $T_{\text{melt}}$ , corresponds to the material behavior observed during the DSC testing.

### *3.3. Experimental Set Up*

Work done by previous researchers examined phase and temperature identification in rectangular geometries through ultrasonic waves [13,22,23]. Current research built on the work of Jost for cylindrical geometry by extending to the 2D quantification of the internal temperature and phase state. Experimentation was performed with CBL-125 wax inside a 5-gallon steel container.

The five-gallon container uses a 3.5 inch aluminum cube, fabricated by the project sponsor, with a Watlow heating element placed inside of it as the heat source. Wires containing a K-type feedback thermocouple for the heater block as well as the power supply cord for the heating element protrude from a small hole in the bottom of the

container. The heating element is powered and controlled using a Watlow EZ-Zone temperature controller and is shown in Figure 3.16.



Figure 3.16. Watlow EZ-Zone temperature controller with hookups.

The heater block has a 1-inch standoff above a 1/2-inch thick mat of high temperature RTV silicone rubber, which insulates the bottom of the container. A cutout schematic of the steel bucket containing the heater is shown in Figure 3.17, along with depiction of the thermocouples and transducers. It should be noted that the steel container has a larger diameter at the top than at the bottom [46]. The diameter is 280.64mm at the location of the upper transducers and 277.00mm at the location of the lower transducers

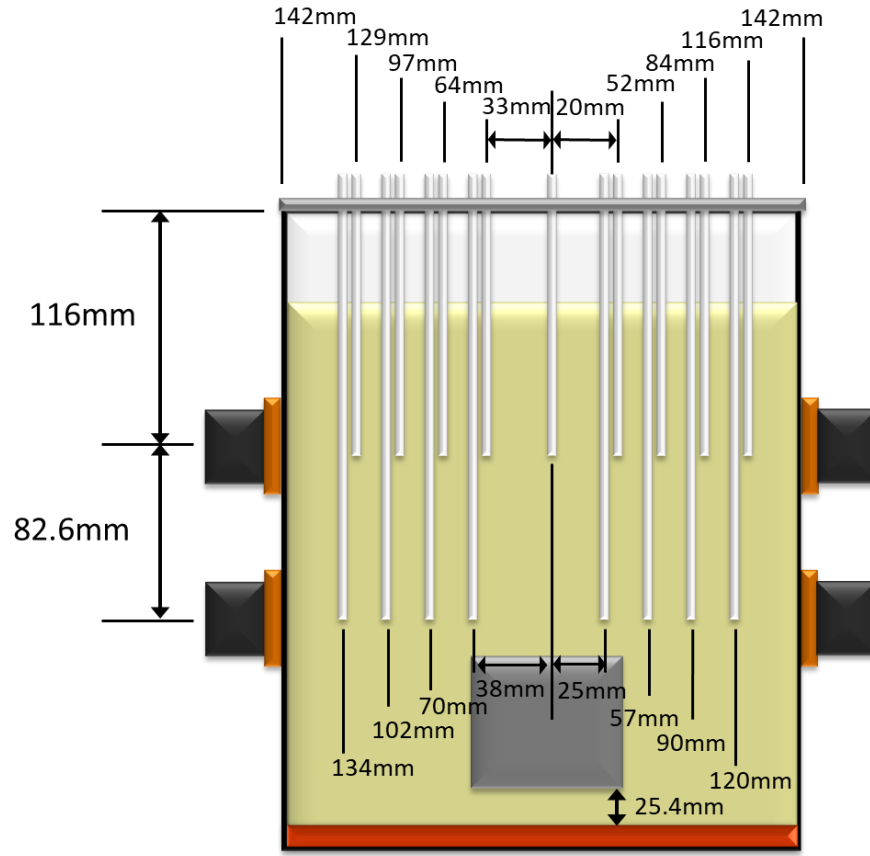


Figure 3.17. Diagram of internal experimental setup.

There are seventeen internal thermocouples (all K-type) which monitor the internal temperature of the CBL-125 and record that data to a computer using the Graphtec GL820. Nine of those thermocouples are inserted until they are at the depth of the center-height of the upper ring of transducers, and another eight thermocouples are inserted to the depth corresponding to the center-height of the lower ring of transducers. The thermocouples are held in place by a custom machined aluminum bar which spans the top of the container and maintains all thermocouples in a single line. To reduce the amount of interference with ultrasonic signals, the bar is positioned so that it is between

ultrasonic paths, and no transducers are sending signals across or through all the thermocouples as depicted in Figure 3.18.

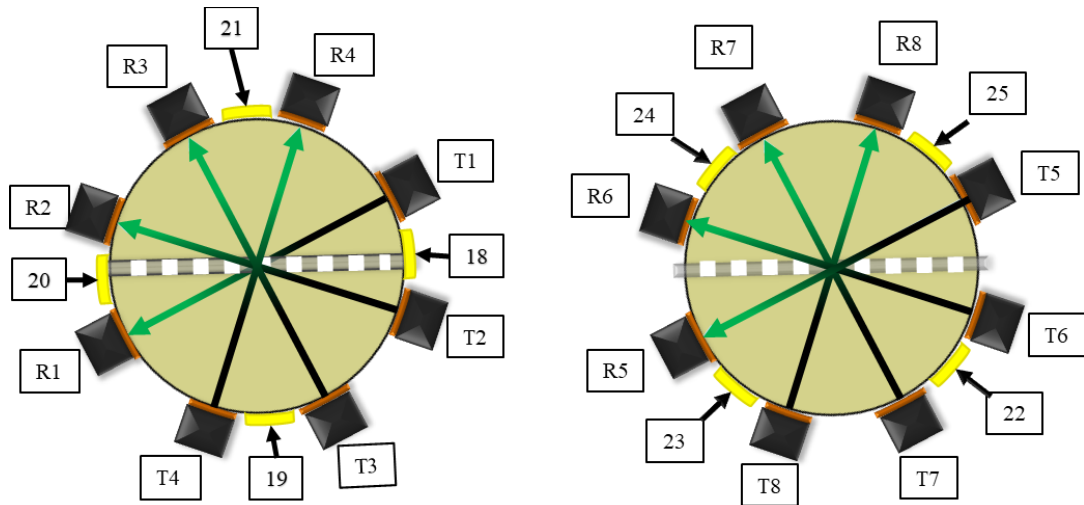


Figure 3.18. Ultrasonic pathways and thermocouple bar location.

On the exterior of the container, eight transducers are positioned at the same height, forming 4 ultrasonic paths within the xy-plane formed by the transducers. This creates a total of eight ultrasonic paths using sixteen transducers, all connected to the EUT3160 pulsar/receiver. The transducers are paired such that a single transmitting transducer has a single receiving transducer. The ultrasonic pathways created by the transducer pairs are referred to as channels in further discussion, and the ultrasonic channels are delineated in Table 3.1.

Table 3.1. Transducer pairs and ultrasonic channels

Transducer Pair	Channel Number	XY-Plane
T1, R1	1	Upper
T2, R2	2	Upper
T3, R3	3	Upper
T4, R4	4	Upper
T5, R5	5	Lower
T6, R6	6	Lower
T7, R7	7	Lower
T8, R8	8	Lower

The placement of the eight transducers on a single plane is such that they are 45 degrees apart. The maximum beam spread for this experiment is calculated using equation 3.1 and taking into consideration the two ultem plates, the steel container, as well as the speed of sound of wax, such that V is 2400m/s, 5890m/s, and 1700m/s for those materials.

$$\theta = \arcsin\left(\frac{1.2 * V}{2.54\text{cm} * 0.5\text{E}6}\right) \quad (3.7)$$

The total beam spread is given by:

$$\theta_{\text{total}} = 2 * \theta_{\text{ultem}} + 2 * \theta_{\text{steel}} + \theta_{\text{wax}} \quad (3.8)$$

Using those equations, the total beam spread is calculated to be 3.6 degrees. Due to the size of the beam spread compared to the placement of the transducers, which are 45° apart, each ultrasonic receiver will only receive signal from the transducer directly opposite. This was verified by aligning transducers and incrementally moving the

receiving transducer a degree at a time. At 4°, the signal received dropped by more than 60dB. This number is the industry standard for determining when a signal is considered detectable in NDT/NDE using ultrasonics.

There are eight Olympus self-adhesive K-type thermocouples, four on each plane to log the surface temperature of the bucket. Their alternating placement is shown in Figure 3.18. The alternating placement of the external thermocouples is designed to identify if any region(s) of the container experiences significantly higher temperatures. The external temperature of the container is also used in the analysis and will be discussed further in Chapter 4. The transducers used in this study have a manufacturer recommended operation limit temperature of 50°C. The metal surface of the container does at times reach temperatures in excess of 80°C. To prevent damage to the transducers, custom machined Ultem plates are used to insulate the transducers from the container surface. The curvature of the Ultem face, corresponding to a diameter of 283mm matches the curvature of the exterior of the 5-gallon container at its widest point. A diagram of a representative ultem plate is shown in Figure 3.19. The curvature allows acoustic coupling between the container surface and the transducer. The Ultem plates are 1.5-inch by 1.5-inch squares, which are 3.174mm (1/8in) thick prior to machining the radius. A photograph of an ultem insulating plate is shown in Figure 3.20.

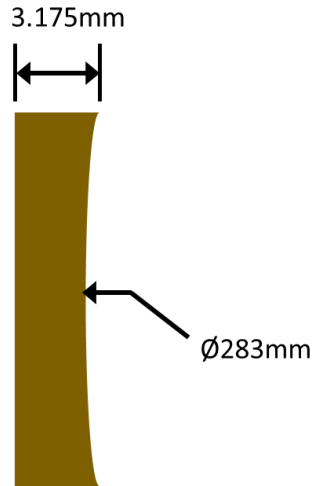


Figure 3.19. Ultem dimensions.

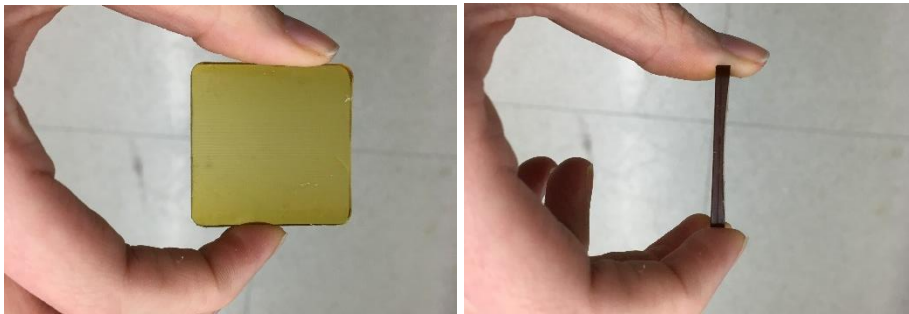


Figure 3.20. Representative Ultem insulating plate.

A diagram and photograph of the experimental setup are shown in Figure 3.21. The 5-gallon container is set on wooden blocks to allow the wires for the heating element to exit the container and reach the power supply without pinching. A quick-release hose clamp from McMaster-Carr is used on each plane of transducers to hold them in place. The pressure also aids in maintaining acoustic coupling between the transducers and the ultem insulating plate, and between the ultem insulating plate and the 5-gallon container.

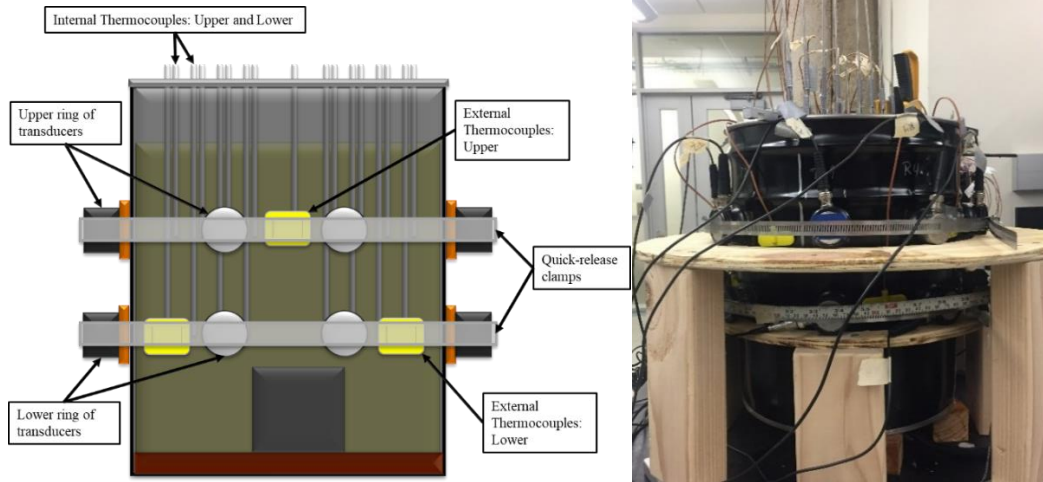


Figure 3.21. Diagram of the experimental setup (left) and photograph of the experimental setup (right).

### 3.4. MATLAB and LabVIEW

Ultrasonic data is collected using an in-house code deployed within the LabVIEW environment. The captured thermocouple and ultrasonic data are processed using a custom script written in MATLAB. This section details the steps taken to collect and analyze the data. As part of the analysis, the speed of sound as a function of temperature profile from Section 3.2 is used to approximate the spatially varying temperature across an ultrasonic path based on the time of flight of the ultrasonic signal and the externally observed temperature profile.

#### 3.4.1 LabVIEW: Data Collection

The pulsar/receiver is controlled through a custom LabVIEW program, developed as part of this thesis. The main VI begins by enabling the EUT pulsar/receiver. The transducer is then fired  $N$  times and the average signal displayed on the front panel, where  $N$  is a user-defined number which can be changed on the front panel. Averaging

the a-scan reduces some of the random electrical noise present due to the large signal amplification required. Because the transducer can fire multiple times on the order of several milliseconds between firing, and the thermal variations of the wax occur on the order of minutes, even 100 transducer firings are occurring at essentially the same temperature state. The averaged signal from N scans is then saved to a .dat file, and this process is repeated until each transmit/receive pair has executed the firing sequence. In addition to recording the averaged a-scan from each of the eight transmit/receive pairs, the code records the gain used during data collection for each channel, as well as the global time the transducers are firing. The custom front panel also allows the user to define buffer length, ultrasonic frequency, trigger delay, total test time, the time between scans, the saturation threshold used in the automatic gain adjustment, and the desired test method (through transmission or pulse-echo).

The buffer length sets the number of samples captured by LabVIEW, and the frequency (MHz) determines the rate at which the ultrasonic signal from the transducer is sampled. A sampling frequency of 10MHz was chosen, capturing 10 samples every microsecond. Experimental observation determined this to be a frequency which captured all the peaks of the ultrasonic signal. Buffer length and frequency must be set so that the recording duration fully captures the ultrasonic signal as:

$$\text{recording duration } (\mu\text{s}) = \frac{\text{buffer length (samples)}}{\text{frequency (MHz)} \times 1\text{E}6} \quad (3.9)$$

The buffer length is expanded so that no features of the ultrasonic signal were lost during data collection by LabVIEW. An increase in buffer length requires more data to be recorded and stored. The trigger delay in number of samples is defined so as not to log data until just before the relevant signal is desired to be captured. A proper choice of the

trigger delay and buffer length will allow the entire ultrasonic wave to be captured without unnecessary data collection, thus increasing the program execution efficiency while reducing the data set file size.

The test duration is based on the global timer within the LabVIEW program. The longest tests with the 5-gallon setup ran 552 minutes. A test time of 552 minutes provided enough time to fully melt the wax across both transducer planes, as well as to turn off the heater and observe the cooling and resolidification process of the wax.

The time between scans is also a user defined option set on the LabVIEW front panel. This is called the time between scans, as each Nscans for all channels may take several seconds. The captured ultrasonic signals are plotted in terms of intensity, on a scale of 0 to 100 percent. Built into the LabVIEW code is a saturation threshold, which is the maximum intensity of an a-scan. This value was set at 80%, which is industry standard and allows the signal to be fully captured. When an ultrasonic signal was above or below the threshold, an algorithm was coded within LabVIEW to adjust the gain to match the saturation threshold set point. Electrical gain is defined by equation 3.10,

$$\text{Gain (dB)} = 20 \log_{10} \left( \frac{V_{\text{output}}}{V_{\text{input}}} \right) \text{dB} \quad (3.10)$$

where  $V_{\text{input}}$  is the voltage prior to amplification, and  $V_{\text{output}}$  is the voltage after amplification. To automatically adjust the gain, the ratio of  $\frac{V_{\text{output}}}{V_{\text{input}}}$  is defined as

$\frac{\text{detection threshold}}{\text{signal max}}$ , such that,

$$\text{Gain}_2 \text{ (dB)} = 20 \log_{10} \left( \frac{\text{detection threshold}}{\text{signal max}} \right) \text{dB} + \text{Gain}_1 \quad (3.11)$$

If the detection threshold is larger than the signal max, the gain will increase, and  $\text{Gain}_2$  will be larger than  $\text{Gain}_1$ . If the detection threshold is below the signal max, the gain will decrease, and  $\text{Gain}_2$  will be less than  $\text{Gain}_1$ .

Increasing the electrical gain and amplifying the signal also amplifies any noise in the signal. During data processing, some noise may be filtered out by averaging multiple signals or applying high and low-pass filters, however it is preferred to begin with a high signal-to-noise ratio (SNR). The relative noise present in a signal is represented by SNR, a common ultrasonic parameter. Figure 3.22 shows the difference between a signal with high and low SNR.

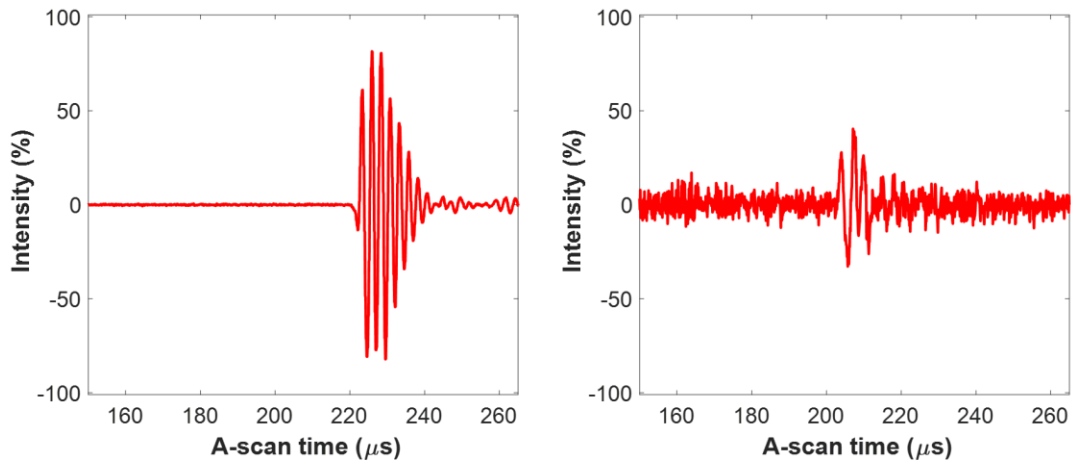


Figure 3.22. High SNR a-scan (left) and low SNR a-scan (right).

The electrical gain from the EUT 3160 pulsar/receiver has an upper limit of 80dB, but in practice a gain of 60dB produces an unacceptable SNR. In times when the coupling between the wax and container or between the container and transducer was poor, the signal required an extremely high gain, yielding a low SNR, making it difficult to determine if an ultrasonic signal was propagating through the material. The automatic

gain adjustment algorithm implemented for data collection does not distinguish between high and low SNR signals and will amplify the signal to reach the saturation threshold, even when the signal has random electrical noise. This frequently resulted in gain that stayed steady at around 80dB until acoustic coupling was improved as the wax melted. The gain recorded and observed is discussed further in Chapter 4.

In this research, through transmission was the only method used; however, the software developed as part of this thesis is capable of running the pulsar/receiver using the pulse-echo method. Chapter 5 discusses future work which may involve both pulse-echo and through transmission in conjunction, and the merits of pursuing that research.

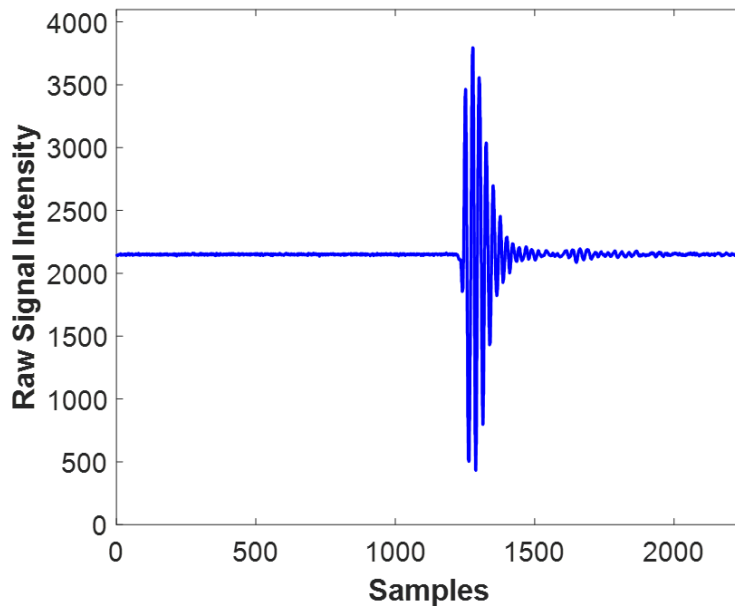
#### 3.4.2 *MATLAB: Ultrasonic Data Processing*

The parameters of the experiment are archived at the beginning of the experiment. At the completion of each subsequent scan, the current time and the number of scans is also archived along with the scan data itself. With this information available it was possible to copy the test data to a new folder and begin analysis at any point during the experiment, without disrupting the test. Thus a real time analysis could be performed at any point during the testing.

A script was developed in MATLAB to process and present all the data for analysis. The developed code consists of four main steps: 1) converting the .dat files from LabVIEW into .mat files for faster analysis; 2) creating informative plots for each transducer channel; 3) processing and plotting the data from the internal thermocouples for comparison with the ultrasonic data; 4) and processing and plotting the estimated temperature data for the channels at each xy-plane without the use of internal thermocouple data.

### 3.4.3 MATLAB: Ultrasonic Data Conversion and Processing

The a-scan data from the EUT 3160 is 12 bit, thus the waveform for intensity can take one of  $4096 = 2^{12}$  values, as shown in Figure 3.23a. The captured 12 bit values were converted in the MATLAB script to a double precision number with a range of -100 to +100. Each a-scan was then shifted vertically by subtracting the mean of the first 500 samples, a region of pure electrical noise. These steps ensured that all a-scans were centered around zero and had identical data ranges that were easy to understand. After shifting and normalizing, the processed data was saved into a proprietary MATLAB format called a \*.mat file for rapid retrieval in later post-processing.



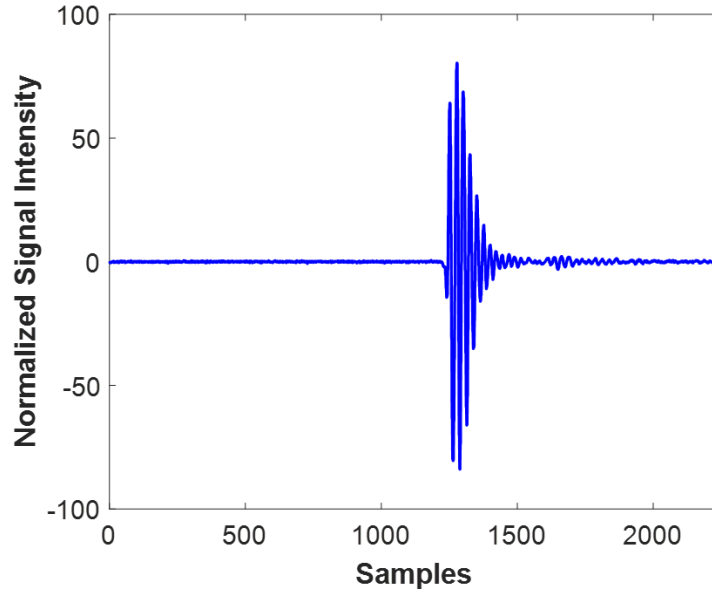


Figure 3.23. Raw signal intensity (top) and normalized signal intensity (bottom).

Note that the signal features are the same between the raw and normalized signals. The normalization process does not alter the signal shape or features.

The second step in the code began by loading the shifted data along with the test parameters. A fast Fourier transform (FFT) was performed on each a-scan to convert the data to the frequency domain. From there, a custom filter was used to denoise the signal. The custom filter combines a low-pass filter of  $0.5\text{MHz} + 0.3\text{MHz}$  and a high-pass filter of  $0.5\text{MHz} - 0.3\text{MHz}$  to keep the signal of the  $0.5\text{MHz}$  transducer and remove other frequencies. The filtered signal was then used for subsequent analysis. The inverse fast Fourier transform was applied to the filtered a-scans, and this filtered signal was used for the subsequent analysis.

The time of flight, used in the speed of sound calculations, is determined from the filtered a-scan. The time of flight is determined by recording the time when the filtered a-scan first crosses a predefined threshold value. This research used a detection threshold to

determine signal onset. The onset of a signal in this research is defined as the time when there is a change from the baseline established previously. A two-part detection threshold of  $\pm 30\%$  and  $\pm 85\%$  was used. The first instance of the signal that was past the detection threshold is considered to be the signal onset. Recall that the signal has been converted to range from -100 to +100.

#### 3.4.4 MATLAB: Informative Plots of Ultrasonic Data

With the data processed, plots could be created for each channel and for each data point in time. Figure 3.24 depicts a representative a-scan at a single point in time. The blue line is the filtered signal, which is used for analysis. The circle marker occurs at the first instance the signal crosses the arbitrary threshold for signal detection.

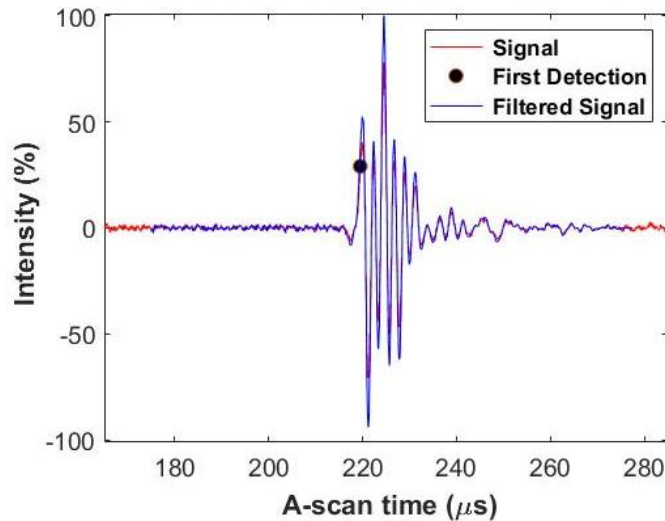


Figure 3.24. Typical a-scan after signal shifting and +/-100 normalization.

The time of flight of a signal is the time when the a-scan intensity passes the detection threshold. Each a-scan is processed using researcher created custom MATLAB

scripts, and a time of flight is measured. This is the raw time of flight, not the time of flight solely within the wax.

The steel container lists a minimum wall thickness of 29 gauge steel [46], and 1020 steel has an ultrasonic velocity of 5890m/s [45]. The duration of the signal passing through one steel wall is

$$\frac{0.3571875\text{mm}}{5890\text{m/s}} = 0.061\mu\text{s} \quad (3.12)$$

Accounting for both walls that the ultrasonic signal must pass through, the time it takes for the signal to pass through both walls is 0.12 $\mu$ s. This value is considered to be negligible, as it is on the order of 1000 times smaller than the time of flight through the wax.

The ultem insulating plates have an experimentally determined speed of sound of 2400m/s<sup>1</sup>, and have a nominal thickness of 3.175mm. In the thinnest part of the radius of the ultem face, the thickness is 2.54mm. Equation 3.13a and 3.13b compares the duration an ultrasonic signal spends in a single ultem plate at nominal thickness and minimum thickness.

$$t_{\text{ultem}} = \frac{3.175\text{mm}}{2400\text{m/s}} = 1.32\mu\text{s} \quad (3.13a)$$

$$t_{\text{ultem}} = \frac{2.54\text{mm}}{2400\text{m/s}} = 1.06\mu\text{s} \quad (3.13b)$$

The duration for two ultem plates, accounting for one ultem plate with the transmitting transducer and one with the receiving transducer is between 2.12 $\mu$ s and

---

<sup>1</sup> Experimental determination of Ultem speed of sound at ambient temperature performed by Taylor Jeffrey on July 2, 2018.

2.64 $\mu$ s. Taking as an example a raw time of flight of 185 $\mu$ s, the time of flight within the wax can be found by subtracting the time spent inside the ultrasonic channel from the raw TOF.

$$\text{TOF}_{\text{wax}} = 185\mu\text{s} - (2 \times 2.12\mu\text{s}) = 180.76\mu\text{s} \quad (3.14a)$$

$$\text{TOF}_{\text{wax}} = 185\mu\text{s} - (2 \times 2.64\mu\text{s}) = 179.62\mu\text{s} \quad (3.14b)$$

The time of flight curve for a representative ultrasonic channel, shown in Figure 3.25, is created by plotting the time of flight inside the wax for each a-scan for the channel over the duration of the test time. This time of flight curve is used extensively in subsequent analysis.

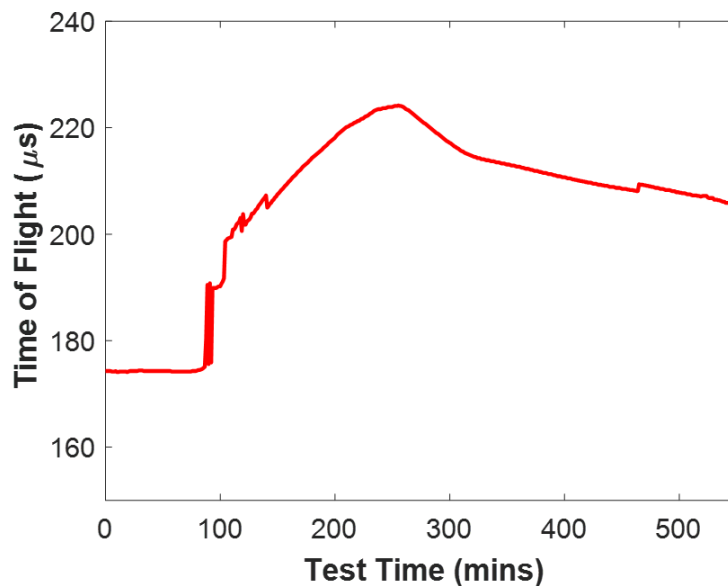


Figure 3.25. Measured time of flight for a representative channel.

The bulk speed of sound curve, shown in Figure 3.26, is created using the data from the time of flight curve. The container has a larger diameter at the top than at the bottom. The diameter is 280.64mm at the height of the upper transducers. Using equation 2.3, the bulk speed of sound is calculated.

$$\frac{0.28064\text{m}}{180.76\mu\text{s}} = 1552.56\text{m/s} \quad (3.15\text{a})$$

$$\frac{0.28064\text{m}}{179.62\mu\text{s}} = 1562.41\text{m/s} \quad (3.15\text{b})$$

The change in ultem thickness results in a difference of 4.94m/s. A curve showing the bulk speed of sound for a representative channel is shown in Figure 3.26. Calculated bulk speed of sound for a representative channel

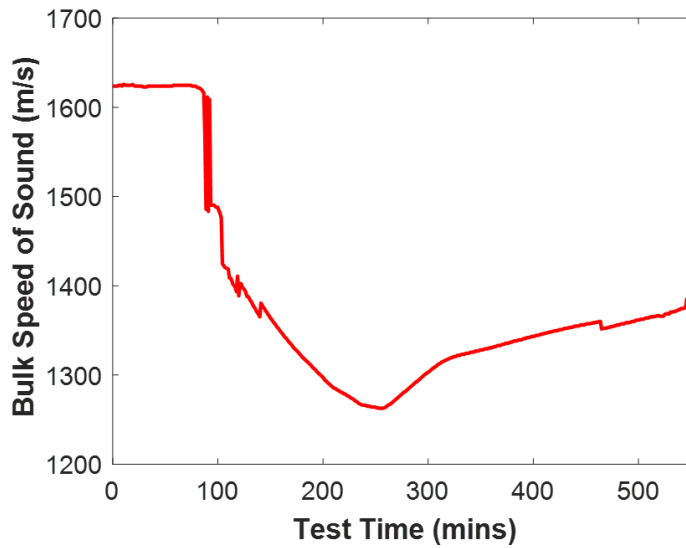


Figure 3.26. Calculated bulk speed of sound for a representative channel

The bulk speed of sound has an inverse relationship with time of flight, so the trends in the bulk speed of sound curve are directly opposite to the trends observed in the time of flight curve. Speed of sound is used to calculate temperature, and bulk speed of sound may be used to calculate bulk temperature, that is a single temperature value corresponding to the bulk speed of sound across the container. Using equation 3.6 and the bulk speed of sound calculated in equation 3.15, a temperature corresponding to the bulk speed of sound is calculated.

$$\frac{1945.3\text{m/s} - 1565.61\text{m/s}}{12.076 \text{ m/s/}^\circ\text{C}} = 32.52^\circ\text{C} \quad (3.16\text{a})$$

$$\frac{1945.3\text{m/s} - 1562.41\text{m/s}}{12.076 \text{ m/s/}^\circ\text{C}} = 31.71^\circ\text{C} \quad (3.16\text{b})$$

A lower speed of sound corresponds to a higher temperature, and the difference in calculated temperature is  $0.81^\circ\text{C}$ . Due to the curved design of the two ultem plates and the 1-inch diameter of the transducer face, it is impossible to know what thickness of ultem the ultrasonic signal is passing through. For subsequent calculations, the assumed thickness of each ultem plate is 2.54mm.

It should be noted that in this example, a difference of 1.27mm resulted in a change in approximated temperature of  $0.81^\circ\text{C}$ . The steel container used has a non-constant diameter. The diameters used in the subsequent calculations are assumed to be at the center of the transducer. However, the transducer face is 25.4mm in diameter. Given that the center point of the transducer is an assumption, and the measurement of the height at which the transducers are located has an associated error of  $1/16''$ , which is 1.59mm, due to the measuring tape used to determine the height, then it is possible that the diameter of the container is reasonably within  $\pm 2\text{mm}$ . If the diameter was assumed to be 277mm and it is actually 275mm equation 2.3 can be used to determine the bulk speed of sound for both cases, assuming a representative TOF of  $220\mu\text{s}$ .

$$\frac{0.277\text{m}}{220\mu\text{s}} = 1259.09\text{m/s} \quad (3.17\text{a})$$

$$\frac{0.275\text{m}}{220\mu\text{s}} = 1250.0\text{m/s} \quad (3.17\text{b})$$

The change in diameter has a significant impact on the bulk speed of sound. Using equation 3.6, the effective temperature is calculated.

$$(1513.4 - 1259.09)/3.5064 = 72.41^{\circ}\text{C} \quad (3.18\text{a})$$

$$(1513.4 - 1250.0)/3.5064 = 75.12^{\circ}\text{C} \quad (3.18\text{b})$$

The resulting difference in effective temperature is  $2.71^{\circ}\text{C}$ , based on a change of 2mm in the diameter. It should be noted that this calculation is done for a higher time of flight and lower speed of sound, which is the region of the master curve where the effective temperature changes most rapidly with speed of sound. With a shorter TOF, a smaller difference is to be expected.

The electrical gain of a signal is shown in Figure 3.27 and can be used to identify when the material goes through a phase transition. Experimentation showed that the gain correlated to the phase and generally increased with decreasing temperature, however, the electrical gain varied when there was a disturbance in the signal or change in coupling. In some testing it was observed that it was possible to have an increasing or steady electrical gain that ran counter to the changing temperature of the material, making it an inconsistent measure for material behavior, and thus is only used as indirect validation of the results obtained from the time of flight analysis.

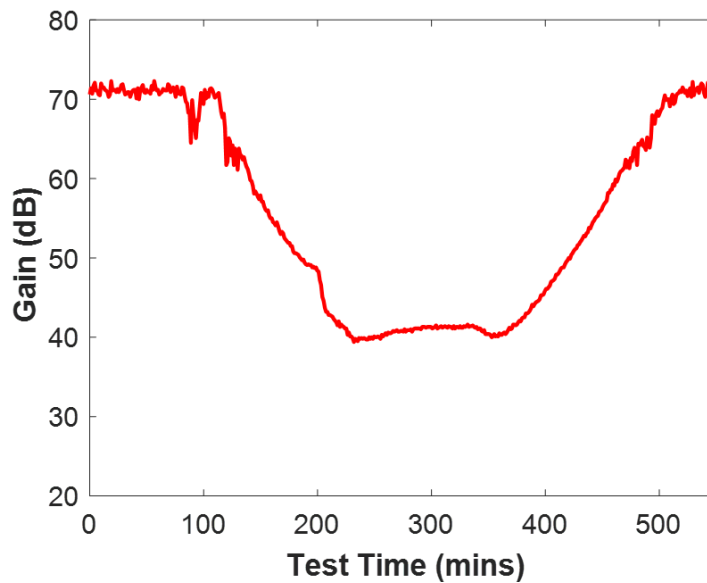


Figure 3.27. Recorded electrical gain of a representative channel.

To visualize the a-scans of a single channel over time, a-scans can be normalized and formatted into a “b-scan.” This visualization differs from a classical b-scan, which plots a signal as a function of position. For the b-scan in Figure 3.28 the vertical axis is the signal time measured relative to a signal firing. The horizontal axis is the wall clock time that the signal was captured. The a-scan signal for each individual scan is normalized to +/- 1 to allow a comparison of waveforms taken over a 25dB range over the duration of the test. The high and low intensity peaks of the a-scans appear as light and dark bands. In the time range between 0 minutes and 80 minutes, the areas of less intensity, with values near zero, exhibit random noise which looks reminiscent of “static”. The signal onset, which is to say the time where the signal peaks first appear, is visually identifiable in this region.

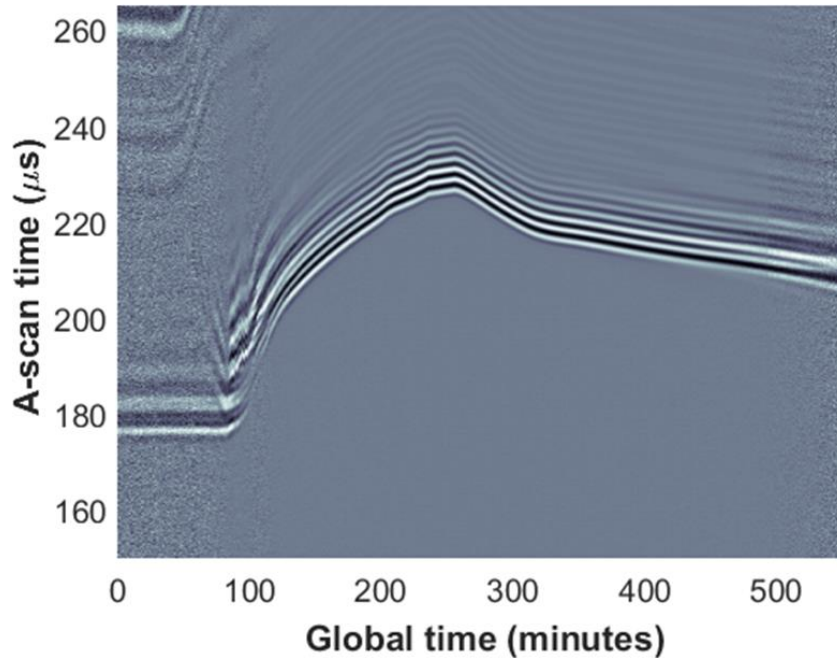


Figure 3.28. B-scan for a representative channel.

The random noise can have values above the detection threshold for signal onset. In those instances, the detected signal time of flight is not representative of the actual signal time of flight as observed in the b-scan. The heating and cooling of the CBL-125 can be observed through the changing time of flight curve for each channel.

Figure 3.29 shows the time of flight curve for Channel 1 with detection thresholds of 15%, 30%, 45%, 60% and 85%. Deviations and aberrations within the time of flight curves are typically the result of a noisy signal, which causes the first detection threshold to miscalculate the actual onset of the signal. The time of flight curve shown in Figure 3.25 is a representation of the signal onset after the two-part detection threshold has been applied to a smoothed curve. Both the two-part threshold and the smoothing of the curve are designed to account for deviations and aberrations within the time of flight curves. These outliers are typically the result of a noisy signal, which causes the first detection

threshold to miscalculate the onset of the signal. It is possible to adjust the detection threshold on the time of flight during post-processing of the data.

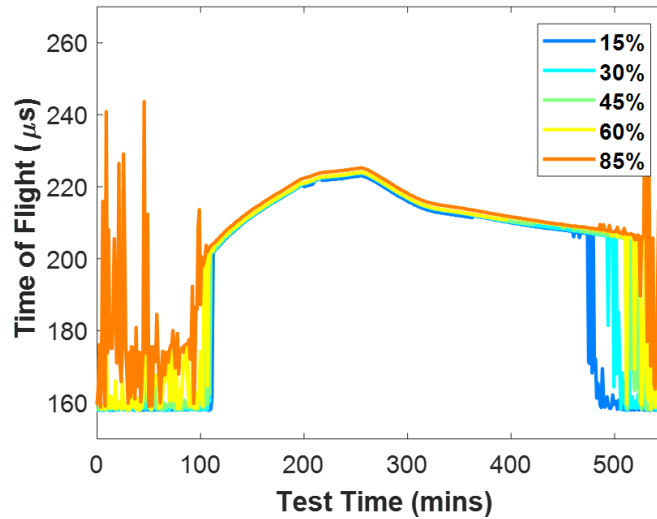


Figure 3.29. Time of flight for Channel 1 with multiple detection thresholds

Both low and high detection thresholds create time of flight curves that have significant variation between data points. The 30% threshold creates a smoother curve above 200µs when compared to the other thresholds. Additionally, when the master curve of CBL-125 speed of sound and temperature was generated, a detection threshold of 30% was used.

If the electrical gain is above 60dB, the detection threshold is set at 85% to avoid the random noise being captured at the high gains. This is based upon careful evaluation of the data and the noisy signals. Figure 3.30 shows an a-scan from Channel 3 at 100 minutes, with a detection threshold of 30% compared to 85%. Within the noise there is an ultrasonic signal visible. The ultrasonic signal is filtered using a combination of a high pass filter of 0.1 MHz and a low pass filter of 0.9 MHz. The transducers used have a nominal frequency of 0.5 MHz, so these filters reduce some of the noise outside the

frequency band of the transducer. The ultrasonic signal is normalized to  $\pm 100\%$  intensity, as discussed previously, which makes it possible to detect the signal at a 30% threshold, however the first detection does not correspond to the ultrasonic signal visible. Rather, the first detection is an artifact of the noise caused by the high electrical gain. By changing the detection threshold to 85% when gain is high ( $>60\text{dB}$ ), first detection occurs at a time corresponding with the ultrasonic signal onset.

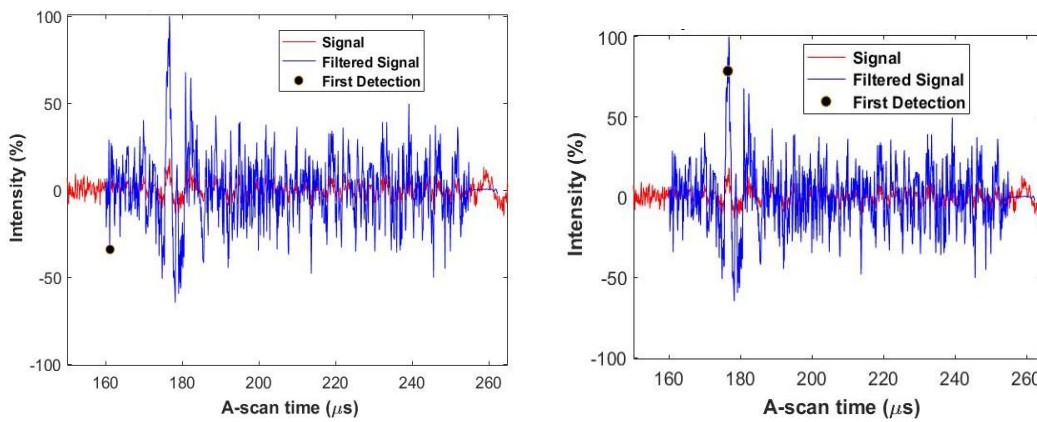


Figure 3.30. Channel 3 a-scan at  $t = 30$  minutes with detection threshold of 30% (left) and 85% (right).

The time of flight curve is crucial because it is used to directly calculate the bulk speed of sound across an ultrasonic channel at each moment in time. To account for some of the variation visible in the time of flight curve, specifically those areas where the TOF appears to oscillate between two values, a banded average approach is used to smooth the data. This is done in areas where the gain is greater than  $60\text{dB}$ , which were identified to be the regions with the greatest amount of variance within the detected signal onset time. The erratic data points seen in the first 100-150 minutes and the last 50-100 minutes of the experiment are caused by the higher electrical gain required to force the ultrasonic signal to reach the saturation threshold. In those periods of higher gain, the detection

threshold is more likely to pick up peaks which do not represent the actual time of flight of the signal. An a-scan with a recorded electrical gain of 60dB or greater is averaged with the four previous and four consecutive a-scans. This removes much of the random electrical noise, which appears as “static” on a b-scan. Figure 3.31a shows the time of flight curve for Channel 1 for multiple detection thresholds when the ultrasonic data has been subjected to the banded average approach to removing noise. Figure 3.31b shows the b-scan for Channel 1 for comparison.

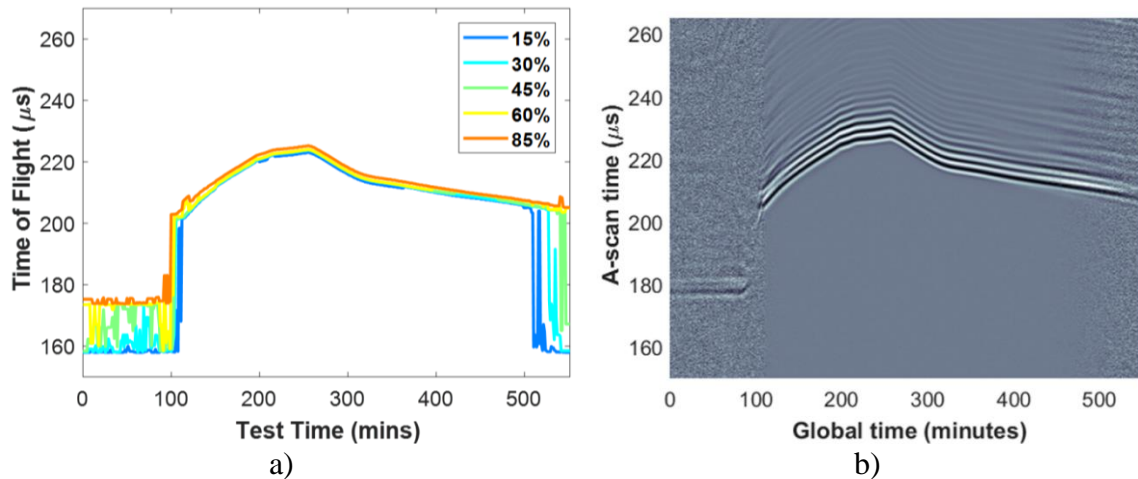


Figure 3.31. a) Channel 1 TOF with detection thresholds b) Channel 1 b-scan.

Recall that the b-scan is generated based on signal intensity, normalized for gain, so the detection threshold will not affect a b-scan. Areas of high intensity, which are either very light or very dark, make it possible to see the signal onset at  $\sim 175\mu\text{s}$ , a value which is now reflected in the TOF curve. It is interesting to note that the TOF curves from data which underwent banded averaging has eliminated the majority of the variance at 30%, 45%, 60%, and 85% detection thresholds. Figure 3.31 also shows how an increase in the detection threshold corresponds to a longer time of flight. The 85%

detection threshold leads to the most consistent signal onset, even before banded averaging.

A two-part detection threshold is created, a step function which relies on the electrical gain of an a-scan. For a-scans with electrical gain less than 60dB, the detection threshold is 30%, as it was for the testing which generated the CBL-125 speed of sound and temperature master curve. For a-scans with electrical gain greater than 60dB, the detection threshold is 85%. This method corrects for some signal onset occurrences, however there are still outliers which appear due to signal noise, as shown in Figure 3.32.

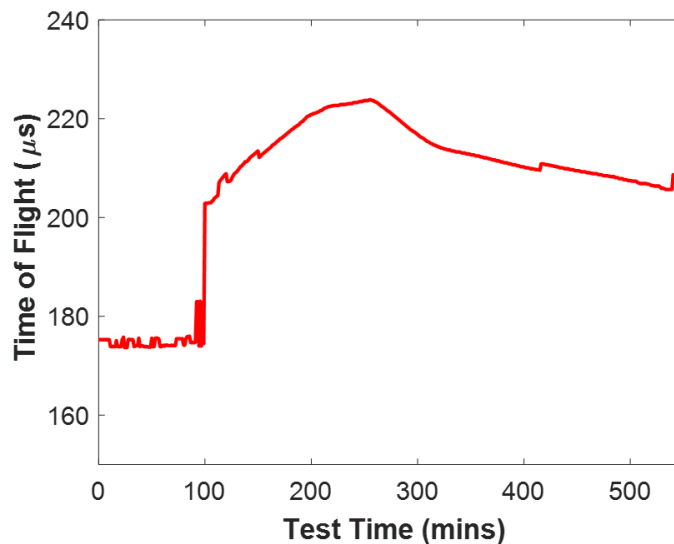


Figure 3.32. Time of flight curve after signal processing.

The effects of cleaning and smoothing the time of flight (and therefore speed of sound) data is most evident in the first two hours and last hour of data. Figure 3.33 shows the b-scan from Channel 1 with the time of flight curve superimposed.

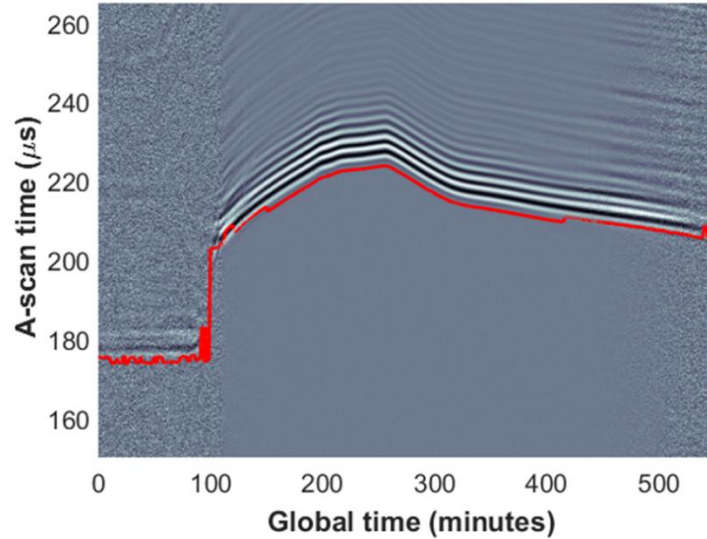


Figure 3.33 Channel 1 b-scan with TOF curve superimposed.

As mentioned, there is some variance within the time of flight curve as generated using the two-part detection threshold, but overall there is good agreement between the TOF curve and the b-scan.

Additionally, recall that in Figure 3.29 and Figure 3.31a, the 15% and 30% detection thresholds estimated signal onset to occur at  $\sim 160\mu\text{s}$ . Using the processes described earlier in this chapter, this corresponds to a bulk speed of sound of approximately 1800m/s. Based on the master curve from Figure 3.15, and extending the master curve to incorporate 1800m/s, this would correspond to an effective isothermal temperature of  $12^{\circ}\text{C}$ , which is significantly below the ambient room temperature of  $21^{\circ}\text{C}$ . Using the proper thresholding, the time of flight curve from Figure 3.32, which is identical to the curve in Figure 3.33, is converted to the bulk speed of sound using the approach earlier in this chapter and is plotted below in Figure 3.34.

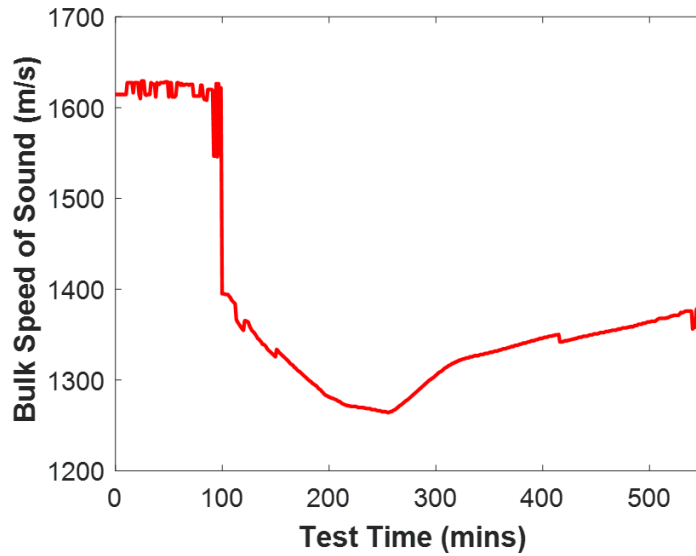


Figure 3.34 Bulk speed of sound curves.

The 2D temperature approximations in Section 4.2 are based on the time of flight and bulk speed of sound curves, where the estimated TOF and bulk SOS value at each data point, generated by the temperature approximation algorithm, is compared to the data which makes up the curves shown in Figure 3.32 and Figure 3.34.

#### 3.4.5 MATLAB: Internal Thermocouple Data Processing and Plotting

As discussed in section 3 of this chapter, there are 17 thermocouples monitoring the internal temperature of the wax along a single line, and another 8 monitoring the external temperature, as depicted in Figure 3.18. The thermocouple data is analyzed by a MATLAB script. The data from the 9 thermocouples aligned with the top transducers and the 8 thermocouples aligned with the bottom transducers are separated. The radial position of each thermocouple is defined in MATLAB based on the experimental setup, shown previously in Figure 3.17. At each moment in time, the temperatures of the internal thermocouples are read, and linear interpolation is used to approximate

temperature in the space between adjacent thermocouple locations. The thermocouple temperature values for corresponding thermocouples along the radial projection are weighted and averaged as depicted in Figure 3.35, such that,

$$T(r^*, \theta) = T_B(r^*) * \frac{\pi - \theta}{\pi} + T_A(r^*) * \frac{\theta}{\pi} \quad (3.19)$$

So the temperature at a radial distance,  $r^*$ , is a function of  $\theta$ ,  $T_A$  and  $T_B$ , the temperatures at points A and B, which are also located at radial distance  $r^*$ .

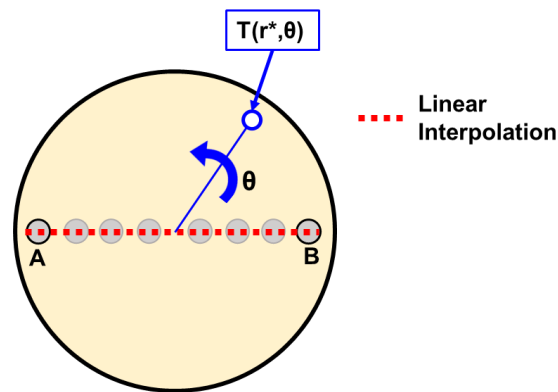


Figure 3.35. Thermocouple temperature approximation scheme.

This creates a temperature approximation which is symmetric about  $y = 0$  for the coordinate system in Figure 3.36.

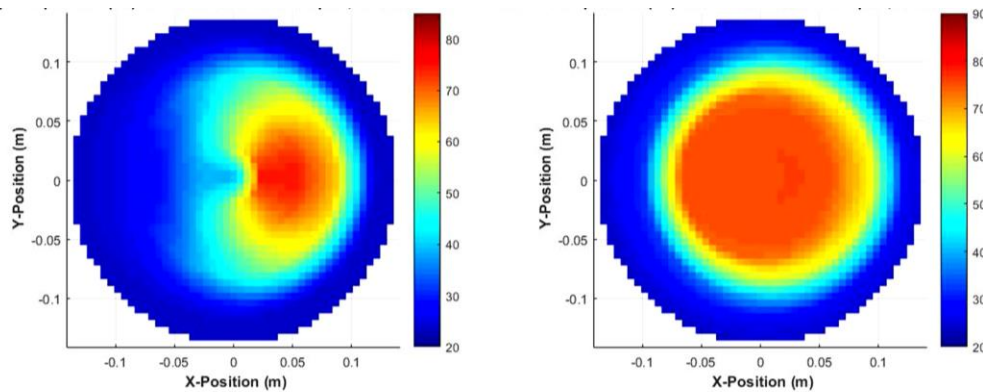


Figure 3.36. 2D temperature mapping from internal thermocouple data at a time when the bucket is not fully melted on the top plane (left) and bottom plane (right).

### 3.5 Radial Temperature Approximation

To create the desired 2D temperature approximation across an ultrasonic plane, the internal temperature profile along each ultrasonic pathway must first be identified. The bulk time of flight and bulk speed of sound through the wax have been captured, and the boundary conditions, also referred to as  $T_{\text{wall}}$ , are the temperatures recorded by the surface contact external thermocouples. Additionally, the piecewise-bilinear master curve for CBL-125, which was discussed in Chapter Three, provides a direct relationship between speed of sound and temperature of the material.

The temperature approximation algorithm assumes a radially symmetric profile across the container. An ultrasonic path, represented by the green arrow in Figure 3.37, traverses the material inside the container, and has a physical distance equal to the diameter of the container. The bulk time of flight along this path is used to approximate temperature, and the approximation is assumed to be radially symmetric, such that the temperature at  $r(x)$  away from the center  $x = 0$  is the same for the first and second halves of the ultrasonic path. Due to the assumed symmetry, the temperature calculations are done for  $0 \leq r \leq r_{\text{wall}}$ , and then symmetry is applied. This does introduce another source of error, as the actual temperature profile may not be radially symmetric, however this is left for a future study to relax this assumption.

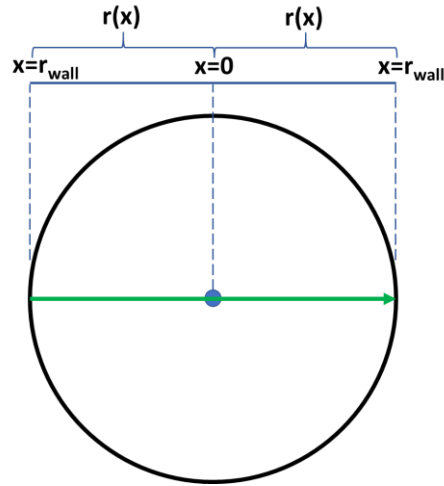


Figure 3.37 Radial symmetry.

The temperature profile takes the form of  $T(r)$ , where  $T(r_{\text{wall}}) = T_{\text{wall}}$ , the boundary condition temperature measured by the surface mounted external thermocouples. The speed of sound is a function of temperature, and the temperature along an ultrasonic path is a function of radius, such that,

$$c = c(T) = c(T(r)) \quad (3.20)$$

and the time to travel  $\Delta r$  is,

$$\Delta t = \Delta r / c(T(r)) \quad (3.21)$$

Assuming the speed of sound is constant over the small distance  $\Delta r$ , then the time of flight across a radial path can be expressed as,

$$\text{TOF}_{\text{radial}} = \sum_{i=1}^N \Delta r / c(T(r)) \quad (3.22)$$

And as  $\Delta r \rightarrow 0$ ,

$$\text{TOF}_{\text{radial}} = \int_0^{r_{\text{wall}}} dr / c(T(r)) \quad (3.23)$$

The assumed radial temperature profile,  $T(r)$ , is found such that,

$$\text{TOF}_{\text{experimental}} - 2 * \text{TOF}_{\text{radial}} = 0 \quad (3.24)$$

Where  $\text{TOF}_{\text{experimental}}$  is the measured time of flight from the ultrasonic data.

The wax inside the container falls into one of three categories: fully solid, partially melted, or fully melted (Figure 3.38). Due to the placement of the heater at the center of the container, combined with ambient temperature below  $T_{\text{melt}}$ , as well as experimental observations, the wax melts internally first.

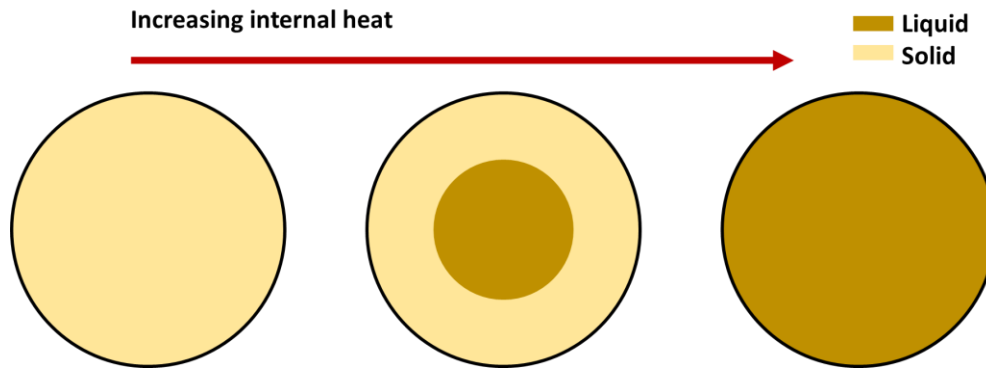


Figure 3.38. Three categories of wax melt.

The radial temperature profile,  $T(r)$  is a function of the parameter  $X$ , such that,

$$X < 0, \text{ fully solid} \quad (3.25a)$$

$$0 < X < r_{\text{wall}}, \text{ partially melted} \quad (3.25b)$$

$$X > r_{\text{wall}}, \text{ fully melted} \quad (3.25c)$$

The radial temperature profile  $T(r)$  can be written as  $T(r(i)) = T(i)$ , which is a discretization of the function  $T(r)$ . For this discretization, the spatial radial location from the center of the container to the wall can be expressed as  $r(i)$ , where  $0 \leq r(i) \leq r_{\text{wall}}$ . To bound the temperature approximation algorithm,  $X$  is bounded by  $[-r_{\text{wall}} \ 4 * r_{\text{wall}}]$ .

The temperature of the liquid wax is characterized by the parameter  $\Delta T$ , which is the temperature difference between the molten wax and the melt temperature.

$$\Delta T = T_{\text{molten}} - T_{\text{melt}} \quad (3.26)$$

Through multiple experiments,  $\Delta T$  was observed to be nearly constant so long as the container still had some solid wax and the heater was on. However, when the heater is turned off,  $\Delta T$  begins to decrease. This behavior is attributed to the internal convection of the fluid that essentially causes continual mixing, and thus a rapid dissipation of the heat, resulting in a near uniform profile inside the liquid wax. The value of  $\Delta T$  is hypothesized to be a function of the temperature state of the heater block, but this hypothesis was never studied during this research. In this research,  $\Delta T$  is represented by a piecewise function.

$$\Delta T = 20, t < t_{\text{off}} \quad (3.27a)$$

$$\Delta T = 20*(1-\beta) + 0.1*\beta, \text{ where } \beta = (t - t_{\text{off}})/(t_{\text{cooling}} - t_{\text{off}}) \quad (3.27b)$$

$$\Delta T = 0.1, t > t_{\text{cooling}} \quad (3.27c)$$

While the heater is on,  $t < t_{\text{off}}$ , the molten wax is modeled to be 20°C above the melt temperature of the wax. When the heater turns off, the residual heat contained within the heater block is modeled by setting  $\Delta T$  to linearly decrease from 20°C to 0.1°C, over a set period of time, defined by  $t_{\text{cooling}}$ . The molten wax is then at a constant  $\Delta T$  of 0.1°C. For these experiments,  $t_{\text{off}} - t_{\text{cooling}} = 150$  minutes.

### 3.5.1 Temperature Profile for $X < 0$ .

The temperature profile for  $X < 0$ , which corresponds to fully solid wax, is defined as,

$$T(i) = T_h * (1 - \beta) + T_{wall} * \beta \quad (3.28a)$$

$$\text{where } T_h = T_{melt} + (T_{melt} - T_{wall}) * X/r_{wall} \quad (3.28b)$$

$$\text{And } \beta = r(i)/r_{wall} \quad (3.28c)$$

As mentioned previously, the liquid wax has a  $\Delta T$  of  $20^\circ\text{C}$  when heating, and a linearly decreases to  $0.1^\circ\text{C}$  when cooling. Figure 3.39 compares the radial temperature profile for heating and cooling when  $X = -0.5 * r_{wall}$ , and  $T_{wall}$  is assumed to be  $30^\circ\text{C}$ .  $T_{melt}$  is at  $50.4^\circ\text{C}$  and is represented by the dashed line in all subsequent plots of radial temperature profiles.

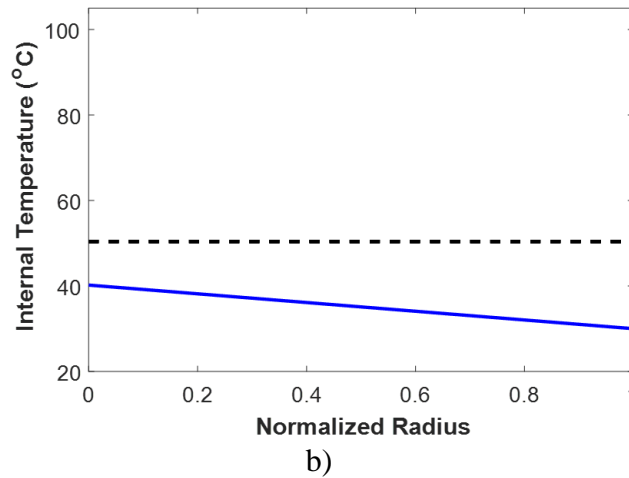
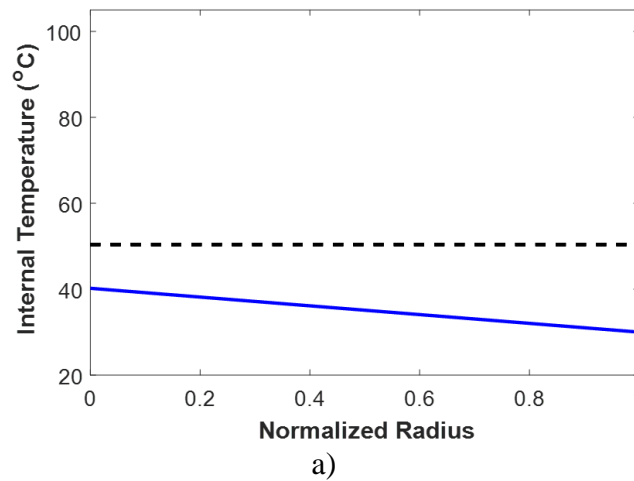


Figure 3.39. Temperature profile for  $X < 0$  during a) heating and b) cooling.

For the temperature profiles shown,  $\Delta T = 20^\circ\text{C}$  during heating and  $0.1^\circ\text{C}$  during cooling. Notice that there is no difference in these two approximations. Both profiles are hotter in the center, and linearly decrease to the wall temperature at the edge. During heating and cooling, the temperature of the liquid wax does not affect the temperature profile for the case when  $X < 0$  and the wax is fully solid.

### 3.5.2 Temperature Profile for $0 < X < r_{\text{wall}}$ .

The temperature profile when  $X$  is greater than zero but less than  $r_{\text{wall}}$  represents the physical scenario of a container with a molten center and solid edges. This temperature profile has a variation between the heating and cooling, unlike the two other cases. Additionally, this temperature profile is significantly more complex than the linear temperature gradient present in solid wax. The temperature profile is comprised of three piecewise linear functions, representing the three distinct zones present in this scenario: fully molten, transition, and outer zone. In the molten region, the temperature profile along the radius  $T(i)$  is defined as,

$$T(i) = T_h \quad (3.29a)$$

$$\text{where } T_h = T_{\text{melt}} + \Delta T \quad (3.29b)$$

$$\text{For } r(i) < r_{\text{melt}} \text{ and } r_{\text{melt}} = X \quad (3.29c)$$

Notice that the liquid wax is at a constant temperature across the radial profile. Due to natural internal convection, the temperature in the liquid wax was observed to be at nearly uniform temperature for a moment in time. The liquid wax's spatial location is bounded by  $r_{\text{melt}}$ , which is equal to the parameter  $X$ . The equations for temperature in molten wax are the same during both heating and cooling.

The outer zone and the transition zone both depend upon two parameters which are defined based on experimental observation and knowledge of material thermal behavior:  $r_{\text{mid}}$  and  $T_{\text{mid}}$ . The parameter  $r_{\text{mid}}$  corresponds to the spatial location along the radius where the wax is solid, such that  $r_{\text{melt}} < r_{\text{mid}} < r_{\text{wall}}$ . The parameter  $T_{\text{mid}}$  corresponds to the temperature at  $r_{\text{mid}}$ , such that  $T_{\text{mid}}$  is between  $T_{\text{melt}}$  and  $T_{\text{wall}}$ . The mathematical definitions of these parameters are different when the wax is heating and when the wax is cooling.

When the wax is heating,

$$r_{\text{mid}} = r_{\text{melt}} + 0.4 * (r_{\text{wall}} - r_{\text{melt}}) \quad (3.30a)$$

$$T_{\text{mid}} = 0.3 * T_h + 0.7 * T_{\text{wall}} \quad (3.30b)$$

When the wax is cooling,

$$r_{\text{mid}} = r_{\text{melt}} + 0.9 * (r_{\text{wall}} - r_{\text{melt}}) \quad (3.31a)$$

$$T_{\text{mid}} = 0.5 * T_h + 0.5 * T_{\text{wall}} \quad (3.31b)$$

With the parameters  $r_{\text{mid}}$  and  $T_{\text{mid}}$  defined, the temperature profile in the transition zone is given by,

$$T(i) = T_h * (1 - \beta) + T_{\text{mid}} * \beta \quad (3.32a)$$

$$\text{where } \beta = (r(i) - r_{\text{melt}}) / (r_{\text{mid}} - r_{\text{melt}}) \quad (3.32b)$$

$$\text{For } r_{\text{melt}} < r(i) < r_{\text{mid}} \quad (3.32c)$$

In this zone, the temperature  $T(i)$  changes linearly from  $T_h$  and  $T_{\text{mid}}$ , between  $r_{\text{melt}}$  and  $r_{\text{mid}}$ , such that  $T(r_{\text{melt}}) = T_h$  and  $T(r_{\text{mid}}) = T_{\text{mid}}$ .

The third zone is the outer “ring” of the container, referred to here as the outer zone. Recall that  $T(r_{\text{wall}}) = T_{\text{wall}}$ , so the outer zone temperature profile is constrained by the wall temperature measured by the surface mounted exterior thermocouples. Using the

same  $r_{\text{mid}}$  and  $T_{\text{mid}}$  as defined in equation 3.31, the temperature profile in the outer zone is given by,

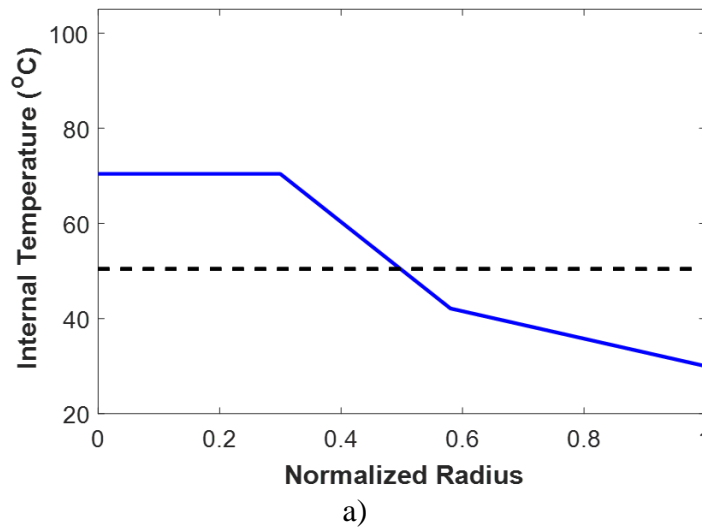
$$T(i) = T_{\text{mid}} * (1 - \beta) + T_{\text{wall}} * \beta \quad (3.33a)$$

$$\text{where } \beta = (r(i) - r_{\text{mid}})/(r_{\text{wall}} - r_{\text{mid}}) \quad (3.33b)$$

$$\text{For } r_{\text{mid}} < r(i) < r_{\text{wall}} \quad (3.33c)$$

Similar to the transition zone, the outer zone also has a linear temperature change such that  $T(r_{\text{mid}}) = T_{\text{mid}}$  and  $T(r_{\text{wall}}) = T_{\text{wall}}$ .

When these equations are taken all together, they create a temperature profile across the entire radius of the container from  $r = 0$  to  $r = r_{\text{wall}}$ . Figure 3.40 shows the temperature profile for  $X = 0.3 * r_{\text{wall}}$ , with a wall temperature of  $30^\circ\text{C}$ . Similarly to Section 3.5.1,  $\Delta T = 20^\circ\text{C}$  for heating, however  $\Delta T = 10^\circ\text{C}$  for cooling.



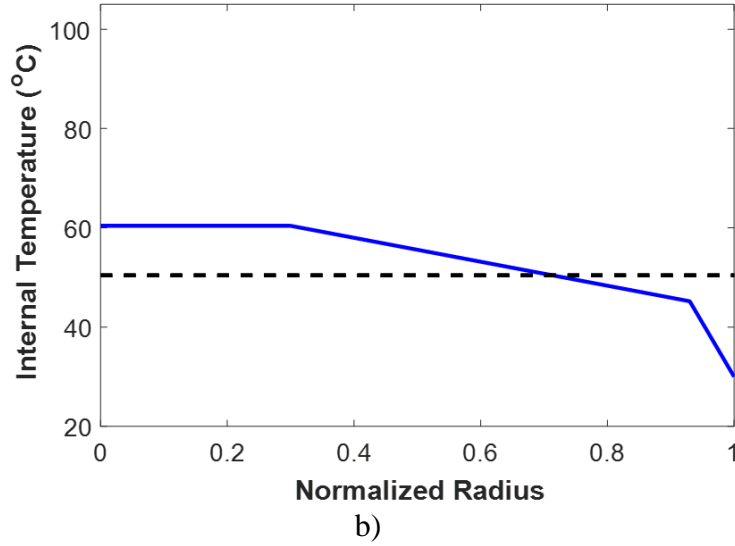


Figure 3.40. Temperature profile for  $0 < X < r_{\text{wall}}$  during a) heating and b) cooling.

The change in coefficients for parameters  $r_{\text{mid}}$  and  $T_{\text{mid}}$  between heating and cooling reflects the wax's thermal response. These equations are chosen based on the 1D heat equation, and the heat distribution that occurs in a material during heating. A 1D model, performed in COMSOL and using the material properties for paraffin wax is shown in Figure 3.41 shows the thermal response of the wax when heat is applied to one side, simulating the internal heating.

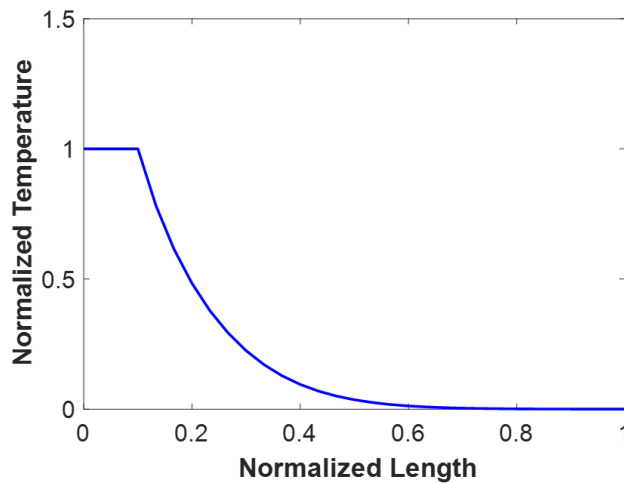


Figure 3.41. COMSOL model of 1D heat equation for heating approximation.

Note the similarity in the shape of the curve to the approximate temperature profile shown in Figure 3.40a, with the steeper slope occurring in the center portion of the radial profile. The exponential decay is significantly more complex than a piecewise linear function, however the approximation is a function only of the input  $X$  and the wall temperature.

Likewise, a 1D heat transfer model is performed, with the material beginning at a uniform temperature and cooling from one end as shown in Figure 3.42. This simulates the wax inside the container, particularly at the plane associated with the lower transducers, which is not exposed to convection from ambient conditions. The heat flux in this experimental condition of cooling comes primarily through the container wall.

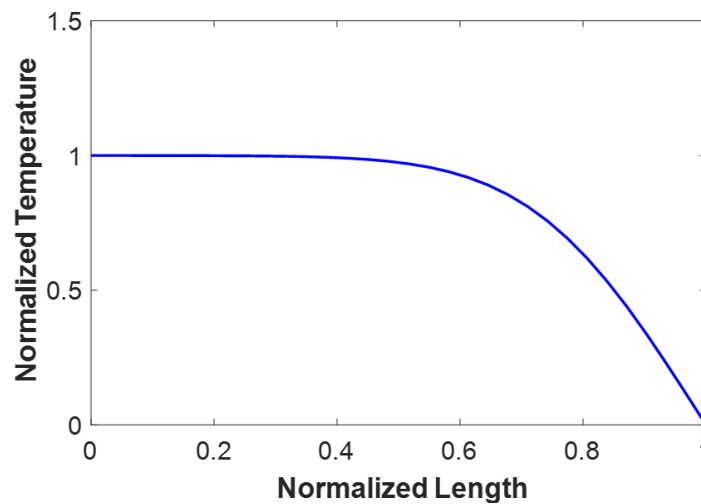


Figure 3.42. COMSOL model of 1D heat equation for cooling approximation.

The shape of this curve is matched by the shape of the representative temperature profile shown in Figure 3.40b, with the steepest slope occurring near the outer edge of the radial profile. While the temperature profile approximation is not an exact match, it is a function only of  $X$  and  $T_{\text{wall}}$ .

### 3.5.3 Temperature Profile for $X > r_{wall}$ .

When  $X > r_{wall}$ , the temperature profile represents the physical scenario of a fully molten container. Although the container is considered to be fully molten, the wall temperature was observed to often be significantly less than the temperature of the wax inside the container. To prevent a step-change from occurring, the profile is comprised of three piecewise linear functions. The first piece represents the radial temperatures inside the molten wax, and is defined as,

$$T(i) = T_h \quad (3.34a)$$

$$\text{where } T_h = T_{melt} + \Delta T * (X - r_{wall})/r_{wall} \quad (3.34b)$$

$$\text{For } r(i) < r_\alpha \text{ and } r_\alpha = 0.98 * r_{wall} \quad (3.34c)$$

Note that when  $X = r_{wall}$ ,  $T_h = T_{melt} + \Delta T$ , providing continuity from the previous case where the molten wax is at a constant  $T_h$ . In this temperature profile,  $r_\alpha$  is nearly the full radius of the container, approximating the wax being melted across the entirety of the container. The next two sections of the piecewise function serve to approximate the gradient which occurs at the very edge of the container, between the molten temperature and the wall temperature.

As in Section 3.5.2,  $r_{mid}$  and  $T_{mid}$  are defined, however in this case they are both taken as the average between the molten and the wall values. The definitions of these parameters do not change between heating and cooling.

$$r_{mid} = 0.5 * (r_{wall} + r_\alpha) \quad (3.35a)$$

$$T_{mid} = 0.5 * (T_h + T_{wall}) \quad (3.35b)$$

So then the temperature profile in the transition zone is defined as,

$$T(i) = T_h * (1 - \beta) + T_{mid} * \beta \quad (3.36a)$$

$$\text{where } \beta = (r(i) - r_{\alpha}) / (r_{\text{mid}} - r_{\alpha}) \quad (3.36b)$$

$$\text{For } r_{\alpha} < r(i) < r_{\text{mid}} \quad (3.36c)$$

This is a function where  $T(i)$  changes linearly from  $Th$  at  $r(i) = r_{\alpha}$  to  $T_{\text{mid}}$  at  $r(i) = r_{\text{mid}}$ . From  $r_{\text{mid}}$  to  $r_{\text{wall}}$ , the temperature profile is given by,

$$T(i) = T_{\text{mid}} * (1 - \beta) + T_{\text{wall}} * \beta \quad (3.37a)$$

$$\text{where } \beta = (r(i) - r_{\text{mid}}) / (r_{\text{wall}} - r_{\text{mid}}) \quad (3.37b)$$

$$\text{For } r_{\text{mid}} < r(i) < r_{\text{wall}} \quad (3.37c)$$

Taking these three pieces of the temperature profile for  $X > r_{\text{wall}}$ , a representative profile can be generated for heating and cooling, for  $X = 1.5 * r_{\text{wall}}$ , with a wall temperature of  $30^{\circ}\text{C}$ . As in Section 3.5.2,  $\Delta T = 20^{\circ}\text{C}$  for heating and  $\Delta T = 10^{\circ}\text{C}$  for cooling.

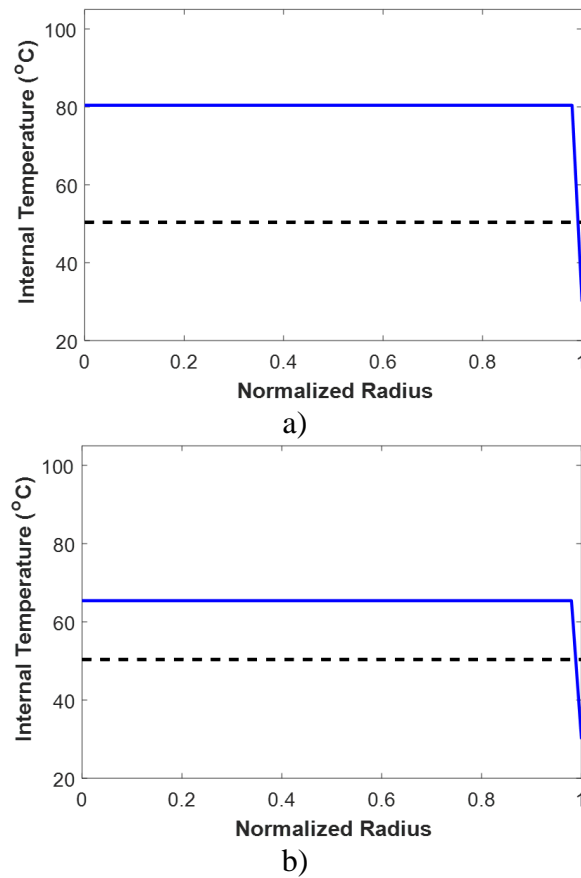


Figure 3.43. Temperature profile for  $X > r_{\text{wall}}$  during a) heating and b) cooling.

It is interesting to note that the difference between these two profiles is based solely on the temperature of the molten wax, which is driven by  $\Delta T$ . At the edge of the container, the steepness of the slope depends on  $T_{\text{wall}}$  relative to  $\Delta T$ .

#### 3.5.4 Temperature Profile Analysis

Recall that the radial temperature approximation is a function of the parameter  $X$  and  $T_{\text{wall}}$ , and that the difference between the measured time of flight and the time of flight based on the radial temperature approximation should be zero, as mentioned in equation 3.24. Since  $T_{\text{wall}}$  is a measured value, the parameter which must vary in order to achieve the minimum difference between  $\text{TOF}_{\text{measured}}$  and  $\text{TOF}_{\text{approximate}}$  is the parameter  $X$ . The algorithm finds the value of the parameter  $X$  which minimizes,

$$|\text{TOF}_{\text{measured}} - \text{TOF}_{\text{approximate}}(X)| \quad (3.38a)$$

$$\text{And, } \text{TOF}_{\text{approximate}} = 2 * \text{TOF}_{\text{radial}} \quad (3.38b)$$

$\text{TOF}_{\text{approximate}}$  is calculated for each a-scan, and the radial temperature approximation  $T(r)$  is also calculated as part of the algorithm. To determine the success of the minimization of the difference between the measured and approximate times of flight, the measured TOF curve is plotted with the approximate TOF curve. Recall that there are multiple sources of uncertainty, such as container diameter, wall temperature thermocouple measurements, as well as those uncertainties and error sources associated with the creation of the master curve which relates speed of sound and temperature for CBL-125. It is reasonable to assume that the estimated bulk TOF and the measured bulk TOF are within  $\pm 3\mu\text{s}$  of each other, based on the error sources discussed previously in Section 3.4.4. Plotting the measured and estimated bulk TOF as a function of time, the

difference between the two is visible in Figure 3.44. If the estimated TOF is within  $\pm 3\mu\text{s}$  of the measured bulk TOF, the approximation is considered to be within the acceptable limits of error for this experiment.

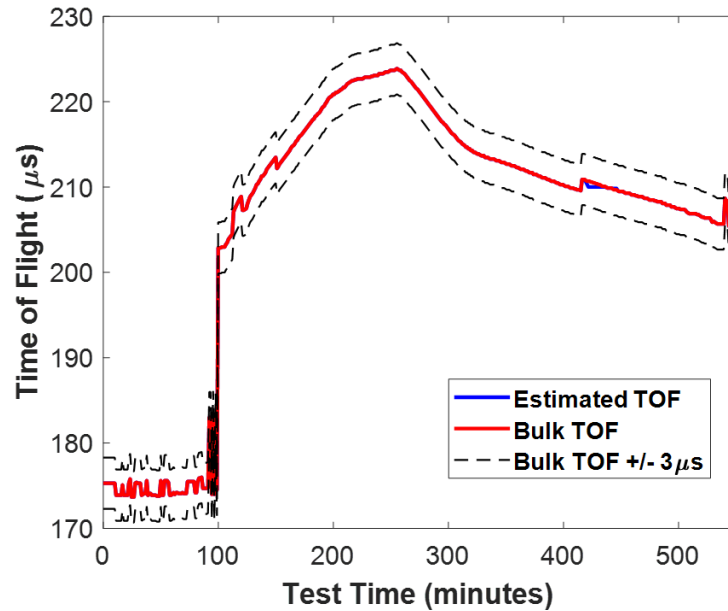


Figure 3.44 Plot of measured bulk TOF and estimated bulk TOF for Channel 1.

This plot is used primarily as a visual assessment of the agreement between the measured TOF and approximate TOF for a channel. To visualize the temperature profile for a channel, the temperature profile  $T(r)$  is plotted across the radial locations at each moment in time, as shown in Figure 3.45.

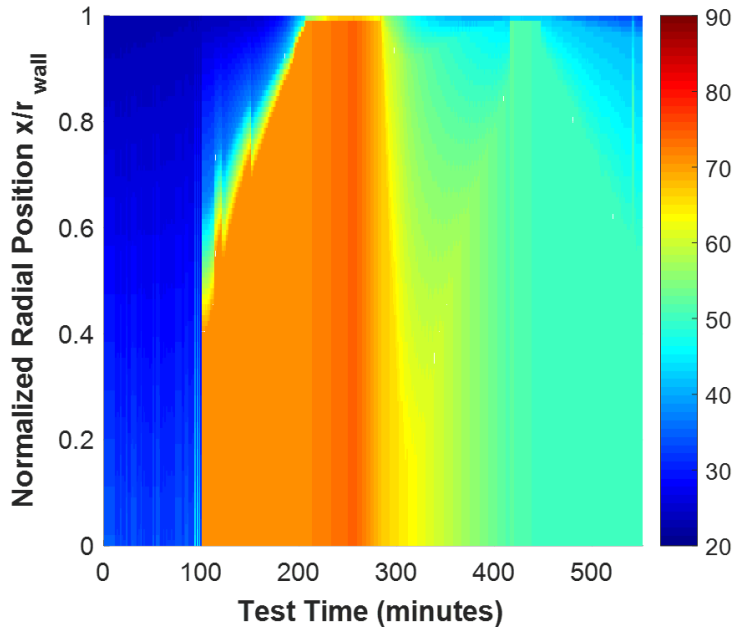


Figure 3.45 Channel 1 radial temperature over time.

### 3.6 2D Temperature Approximation

The final step is combining the channels into a 2D planar temperature map of the internal temperature state of the wax. Channels 1-4, the upper channels, and Channels 5-8 are processed as two groups for the two xy-planes of transducers.

To obtain a 2D temperature approximation, the program connects each temperature value along a radial path using a cubic spline, such that  $T(r(i))$  is now a continuous function  $T(r)$ . The radial temperature profile is mirrored, as per Figure 3.37, so that the temperature profile across the diameter of the container is symmetric about the point  $r = 0$ . Each xy-plane now contains one temperature profile associated with each ultrasonic channel, which spans the diameter of the container. A weighted average scheme interpolates between adjacent temperature profiles on an xy-plane, as  $\theta$  goes from 0 to  $2\pi$ , as shown in Figure 3.46. This method of interpolation allows for temperature profiles which are elliptical in nature.

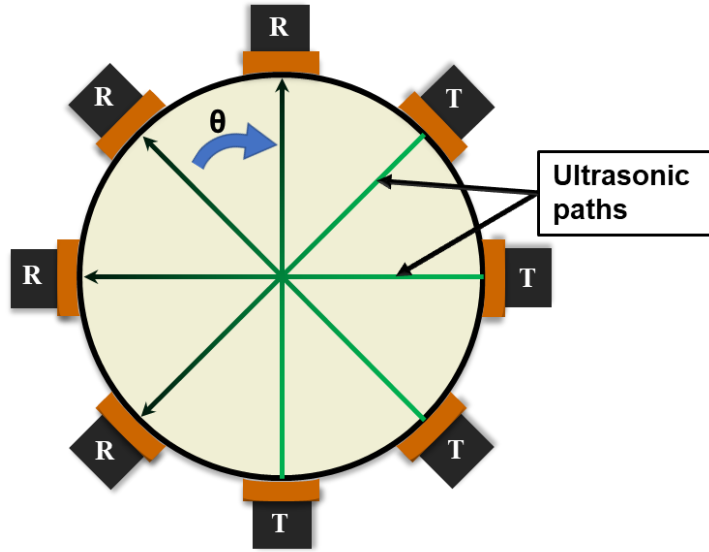
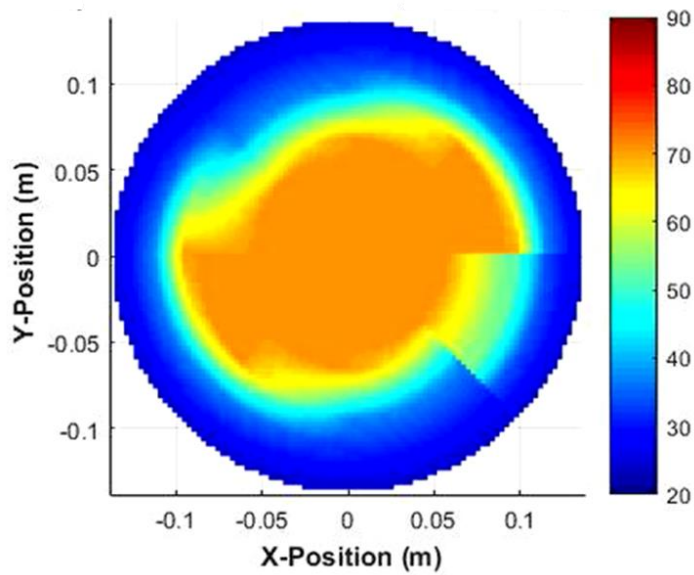
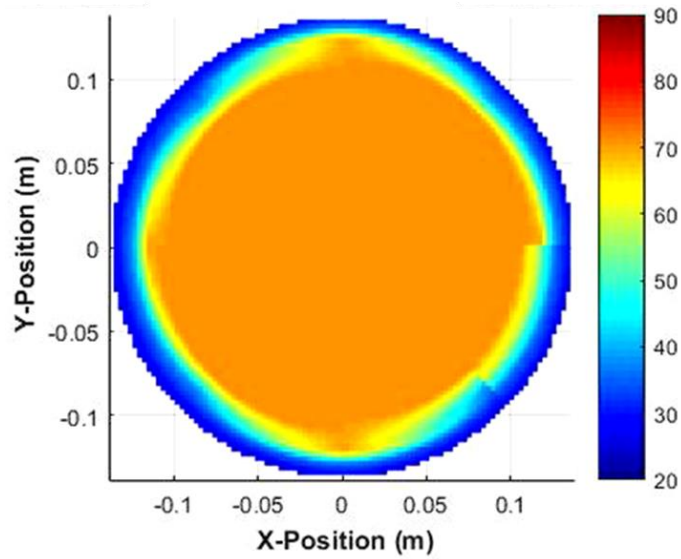


Figure 3.46. Interpolation between ultrasonic paths.

Representative 2D temperature approximations for the xy-planes associated with the upper transducers and lower transducers are shown in Figure 3.47. The 2D images are from line projections of temperature but allow for rapid visual interpretation of the internal temperature state of the wax.



a)



b)

Figure 3.47. 2D temperature approximation for ultrasonic data from the a) upper plane and b) lower plane.

The results of the ultrasonic 2D temperature approximation and the comparison of the ultrasonic approximation with the 2D approximation from the thermocouple data is discussed in Chapter Four.

## CHAPTER FOUR

### Data Analysis and Results

The following chapter will demonstrate on a single data set the methodology introduced in Chapter 3. The experiment analyzed is that of a 5-gallon steel container filled with CBL-125 wax as shown in Figure XYZ. The container was taken to a fully molten state and, 24 hours before data collection began, it was allowed to cool. This allowed there to be an existing thermal gradient in the bucket prior to the test initialization. From all external measurements, both visually and the surface mounted thermocouples, the bucket contained wax in a solid state when the test began. 37 minutes after starting the data collection the internal heater was turned on and set to 230°F. Transducers and thermocouples are positioned and monitored as described in Chapter 3, and thermocouple temperature is collected every 1.0 seconds. The heater is turned off 255.2 minutes into the test, and the data collection continues for an additional 296 minutes until the wax in the vessel had fully solidified based on visual inspection.

In the following discussion, channels 1-4 are the upper ultrasonic paths, and channels 5-8 are the lower ultrasonic paths, as listed in Table 3.1 and shown in Figure 3.18, reproduced below.

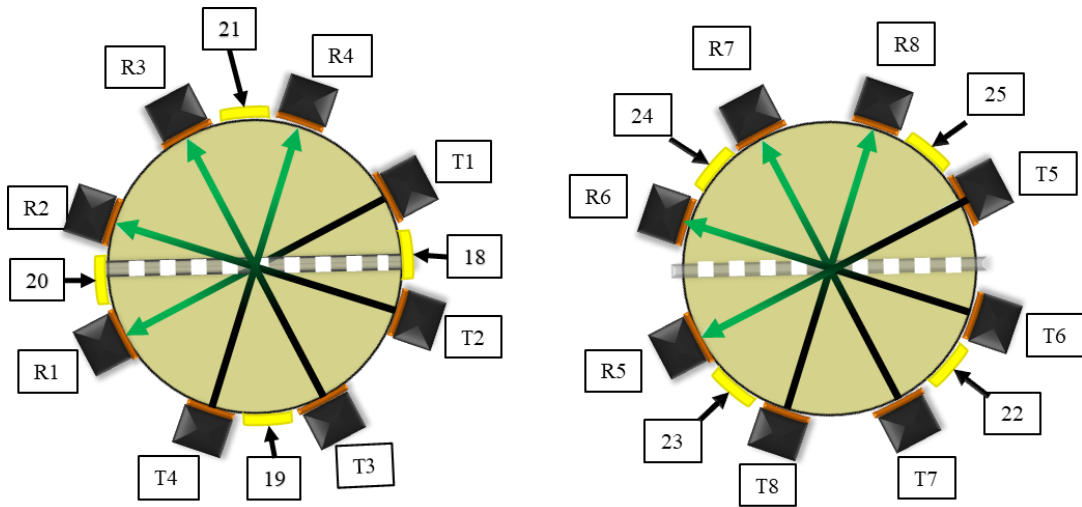


Figure 3.18. Ultrasonic pathways and thermocouple bar location.

#### *4.1 Time of Flight and Bulk Speed of Sound Curves*

Attenuation within a material changes with temperature, and is characterized by the attenuation coefficient,  $\alpha$ , as discussed in equation 3.2 of Chapter Three. As the attenuation present changes with temperature, the electrical gain necessary to maintain signal saturation also changes. The LabVIEW code created in this research is programmed to adjust the electric gain during the data collection so that the signal strength is at 80% saturation. This gain is recorded each time data is collected and is shown in Figure 4.1 for two ultrasonic channels.

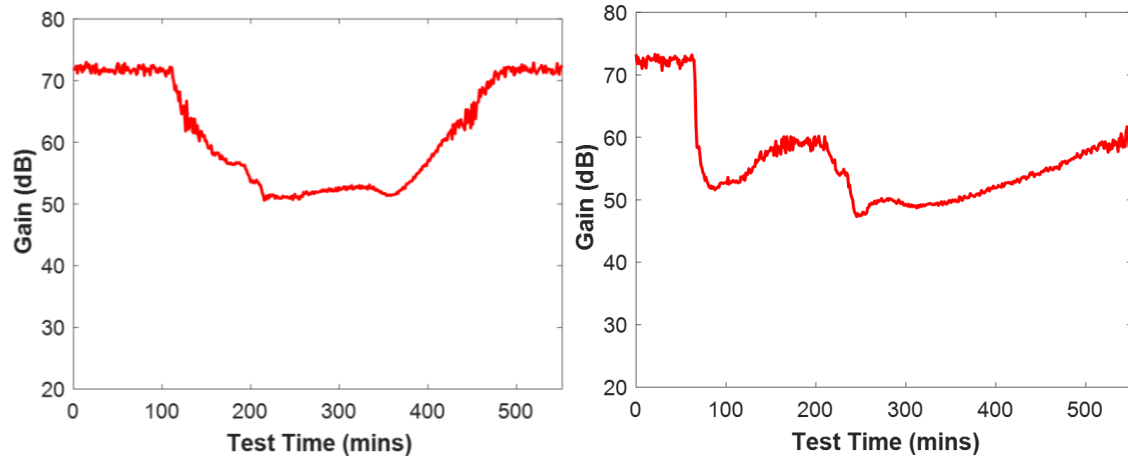


Figure 4.1. Recorded gain from Channel 1 (left) and Channel 5 (right).

Channel 1 is a typical gain curve, which is at the maximum electrical gain of ~72dB for the first 100+ minutes into the test, decreases over time, then increases again during the latter 150+ minutes of the test. Channel 5 displays an increase in gain between  $t = 110$  minutes and  $t = 200$  minutes, which is atypical. The maximum gain occurs when the LabVIEW code attempts to force the ultrasonic signal to reach the saturation threshold. The high gain required is hypothesized to be caused by poor acoustic environment in the test, as the wax has incurred some degree of physical separation from the container wall in the solid state. After that point, as the wax begins to soften and expand, the gain begins to decrease. Following the methodology described in Chapter Three, the time of flight is obtained at each time the data is collected. This is then plotted for Channel 1 and Channel 5 in Figure 4.2.

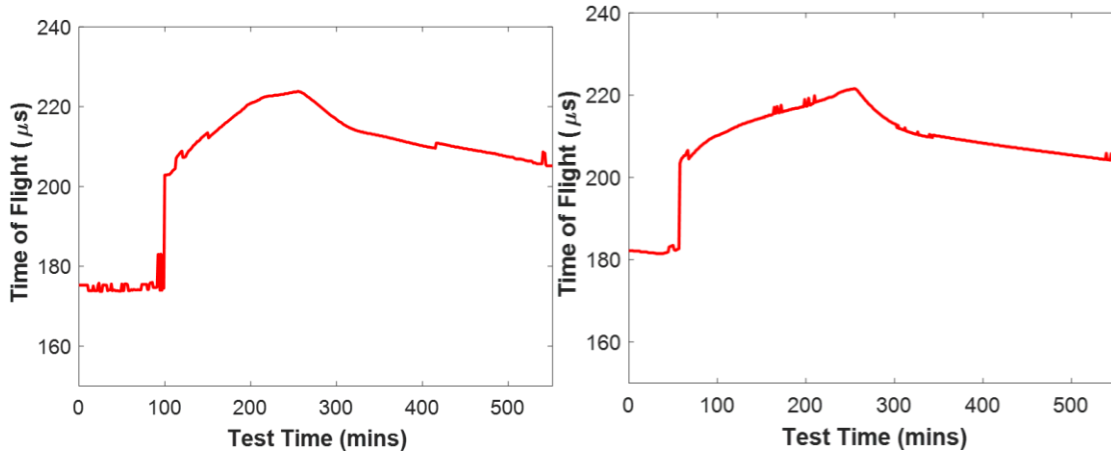


Figure 4.2 TOF from Channel 1 (left) and Channel 5 (right).

It should be noted that time of flight is a function of temperature, as shown in Figure 3.13, where TOF increases as the temperature increases. The temperature and time of flight decrease after 255 minutes while the gain for Channel 1 and Channel 5 is observed to increase as well. The bulk speed of sound at each data collection interval is calculated using the methodology discussed in Chapter Three, and then plotted in Figure 4.3.

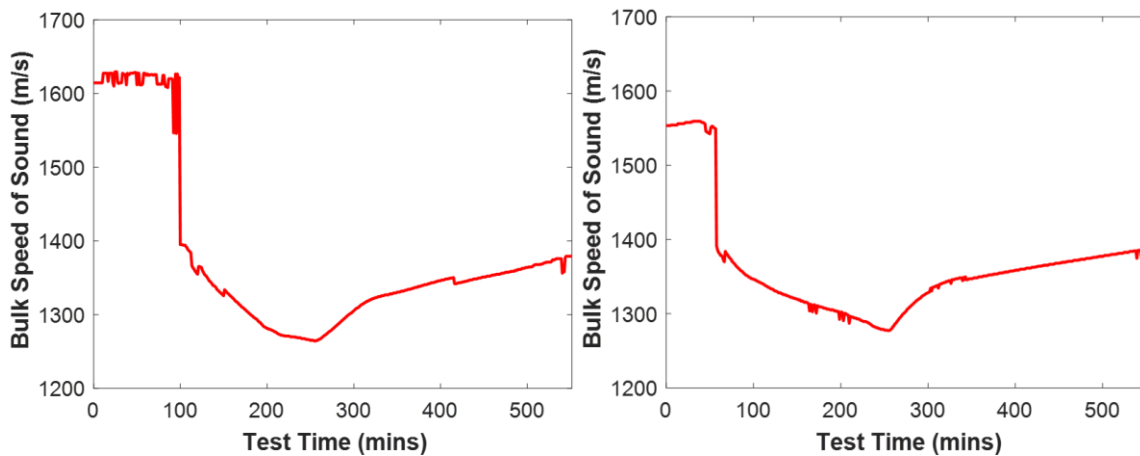


Figure 4.3. Bulk speed of sound for Channel 1 (left) and Channel 5 (right).

Previous research examined tracking the electrical gain required to maintain the saturation threshold and using that data to corroborate or determine if the material is heating or cooling [23]. While gain does follow similar trends as bulk speed of sound, and therefore trends opposite of the temperature of the material, it is an unreliable method. Recall the atypical gain observed in Channel 5. It does not follow the same trend as speed of sound and increases for a significant length of time, between  $t = 110$  minutes and  $t = 200$  minutes, as the speed of sound decreases during that same time period.

To examine a possible cause for this phenomena, two a-scans are compared, one from before the gain began to trend opposite the speed of sound and one from during that time. At  $t = 100$  minutes (Figure 4.4b) the a-scan is clean, with very little noise before or after the ultrasonic signal. The a-scan taken at  $t = 180$  minutes (Figure 4.4d) is significantly noisier. One possible explanation for the difference between these two a-scans is the shifting or slipping of a transducer. As coupling between the transducer and the container degrades, the signal requires more amplification to reach the saturation threshold. That amplification comes in the form of electrical gain, which amplifies not only the ultrasonic signal, but also the data before and after the signal. It should be noted that both a-scans present very similar signal shapes, which might suggest that the increased gain is due to poor coupling rather than an internal phenomenon which might affect signal strength. It is interesting to note that the atypical increase in gain does appear to self-correct and the gain for Channel 5 resumes a typical trend after  $t = 200$  minutes.

For further comparison, a-scans from Channel 1 are included for  $t = 100$  minutes (Figure 4.4a) and  $t = 180$  minutes (Figure 4.4c). Recall that Channel 1 is on the upper

plane, while Channel 5 is on the lower plane. A marked change in bulk speed of sound occurs for Channel 1 at  $t = 102$  minutes, and for Channel 5 at  $t = 64$  minutes. So, the a-scan of Channel 1 occurring at  $t = 100$  minutes is before this change, and in the region of maximum electrical gain, as was shown in Figure 4.1.

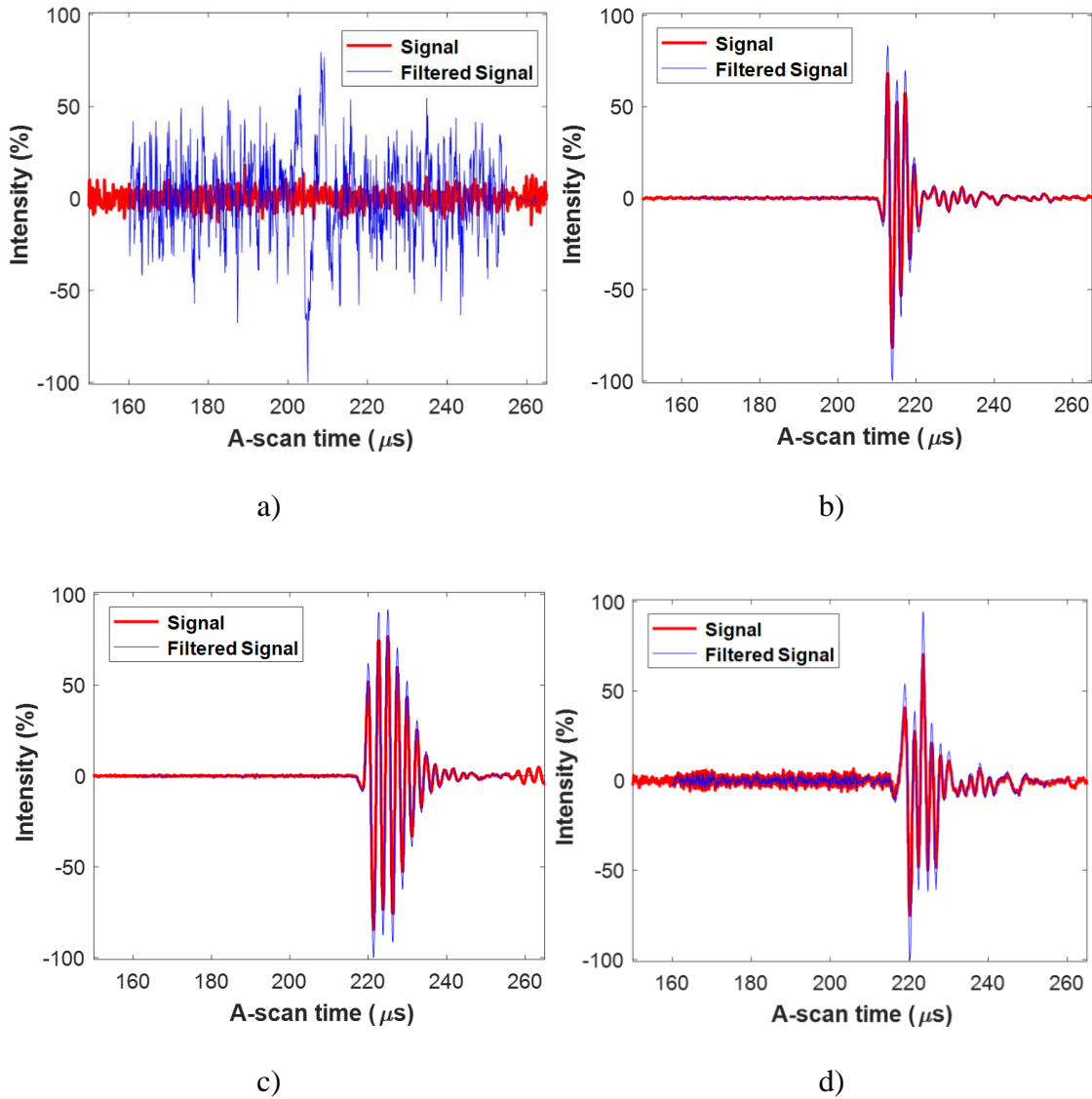


Figure 4.4. Raw and filtered a-scan for a) Channel 1 at  $t = 100$  min, b) Channel 5 at  $t = 100$  min, c) Channel 1 at  $t = 180$  minutes, d) Channel 5 at  $t = 180$  min.

There is no decisive evidence as to the cause of the increasing gain in channel 5 during that the aforementioned time frame, making it an unreliable indicator of the temperature change of the material.

The recorded electrical gain is used to normalize the a-scans, which are used to create b-scans. The time of flight and signal peaks of a-scans change with temperature, and b-scans are one way to visualize the shifting and changing shape of a-scans over time. The electrical gain can also be used to identify a channel which has more noise than is typical. The recorded electrical gain for Channel 4 is shown in Figure 4.5. Note how the gain is above the 60dB threshold used to set the signal detection threshold to 85%.

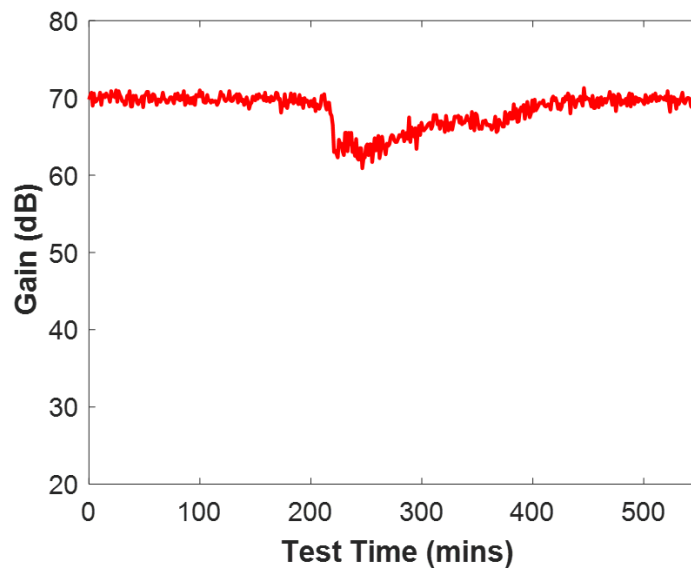


Figure 4.5. Recorded electrical gain for Channel 4.

Examining the b-scan from Channel 4, as shown in Figure 4.6, the first ~200 minutes and last ~100 minutes have high levels of random electrical noise, which presents as static on the grayscale image. The b-scan from Channel 3 has some static which occurs within the first 100 minutes, and it is visible in the last 50 minutes.

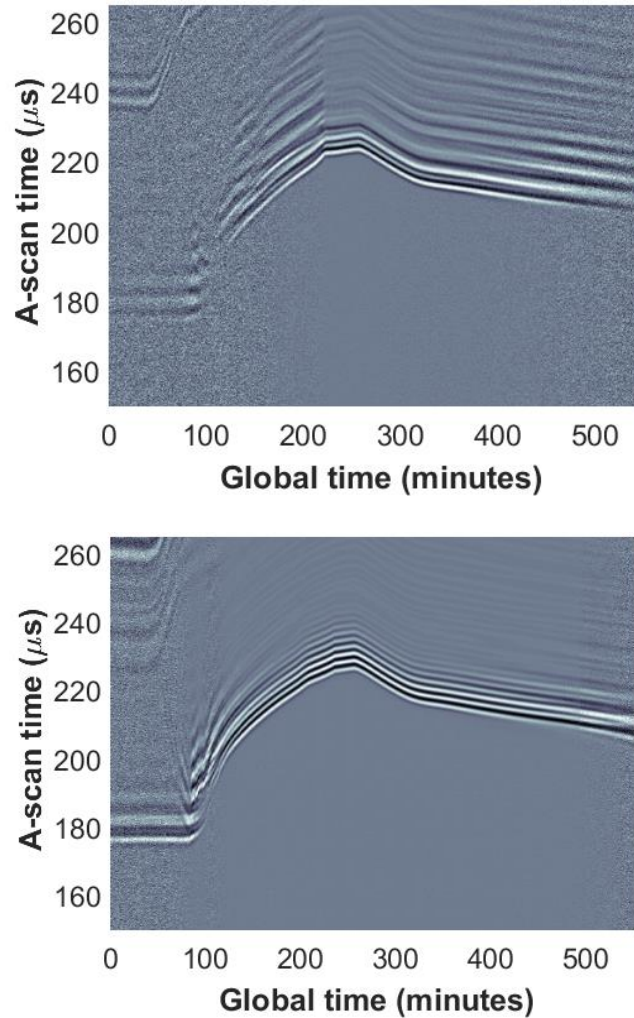


Figure 4.6. B-scan for Channel 4 (top) and Channel 3 (bottom).

Visually examining these two b-scans, the signal peaks and valleys appear as very light or very dark. As the a-scans change and shift during the test, the signal curve is clearly visible throughout the test for Channel 3. Conversely, it is much more difficult to identify the peaks and valleys of the Channel 4 signal curve in the regions of high noise. The presence of so much electrical noise poses a problem for the accuracy of the TOF curve generated using the two-part detection threshold described in Chapter Three. With

a detection threshold of 85% and a noisy signal, the TOF curve shown in Figure 4.7 bears little resemblance to the signal curve visually identifiable in the b-scan.

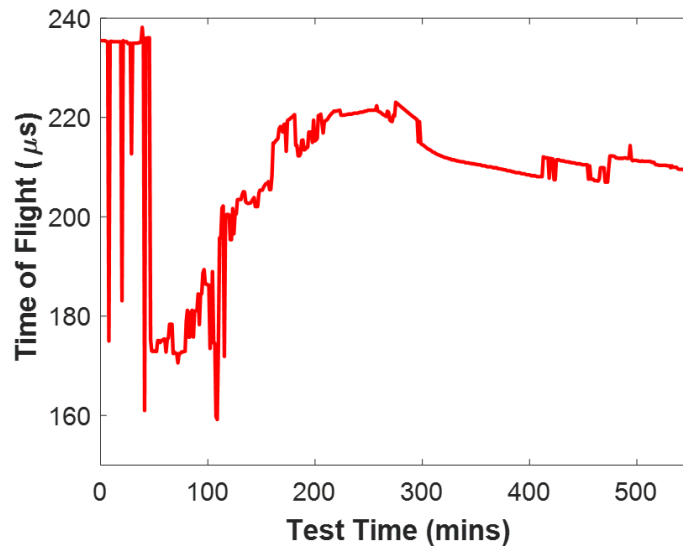


Figure 4.7. TOF curve for Channel 4.

To create a smoother speed of sound curves for use during analysis, points are chosen manually from a plot of the Channel 4 b-scan. MATLAB has a built-in function for piecewise cubic Hermite interpolating polynomials, called `pchip`, that is used to provide smooth, continuous, and second-order differentiable curves fit to the data. This function is used to interpolate between data points. The third-degree polynomials used between each data point are continuous, and the first derivatives at each point are chosen to preserve the shape of the data. A third-degree polynomial spline that is not Hermite may have local maxima or minima at locations not indicated by the data [47]. The piecewise cubic Hermite interpolation function does not create any extrema except where they are found in the data, making it a good fit for the complex speed of sound curve [47]. Figure 4.8 shows the TOF curve for Channel 4 generated using the `pchip` method, superimposed over the b-scan from Channel 4.

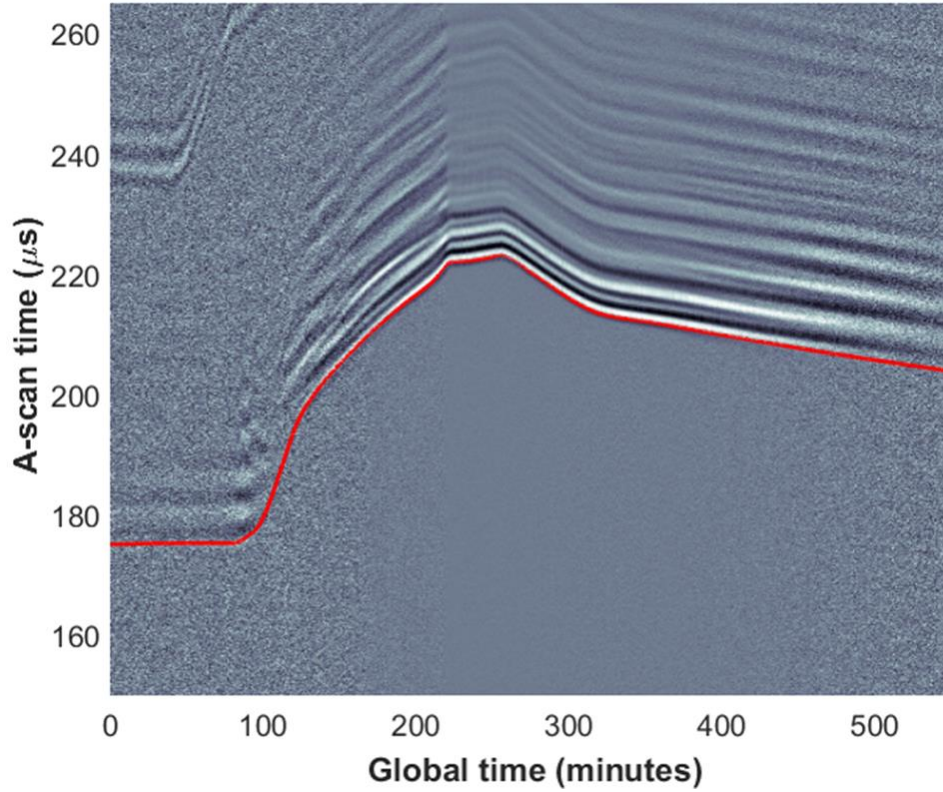


Figure 4.8. Channel 4 b-scan with TOF curve superimposed in red.

Note how the generated TOF curve follows the visible identifiable signal onset change. The time of flight curves for all eight channels are shown in Figure 4.9, and each channel's time of flight curve is colored as indicated in the legends.

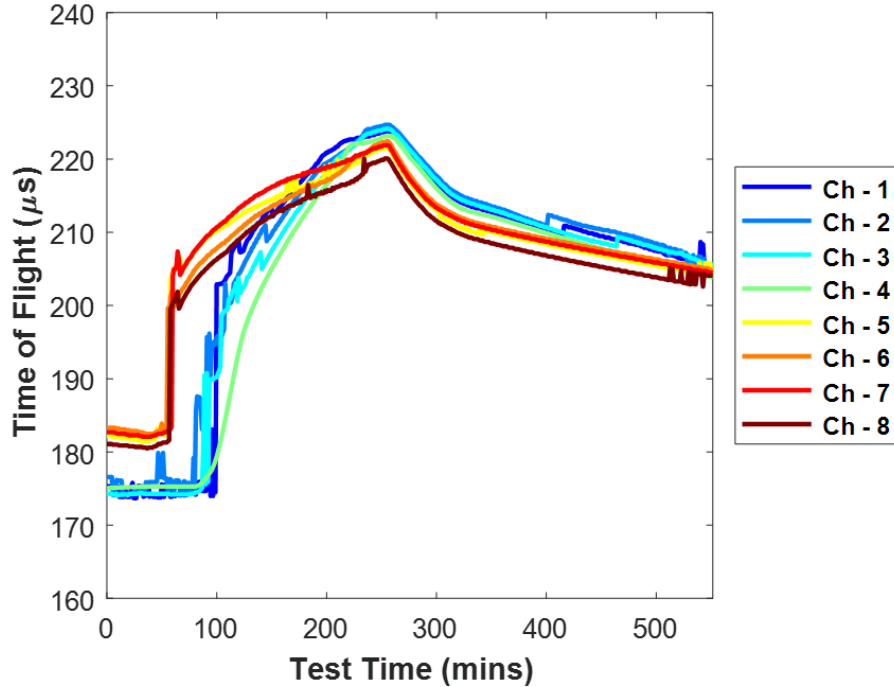


Figure 4.9. TOF curves for all 8 channels.

It is interesting to note how Channels 1-4, which correspond to the transducers on the upper plane, are at a notably different time of flight when the test begins. If the time of flight curve has a positive slope, i.e.  $dTOF/dt > 0$ , the heater is considered to be on, based on Figure 3.15, which is speed of sound of CBL-125 as a function of temperature. When the time of flight curve exhibits a negative slope, i.e.  $dTOF/dt < 0$ , the heater is considered to be off. Based on the time of flight curve shown in Figure 4.10, the heater turns is on until  $t = 255.2$  minutes, when it is assumed to turn off and remain off for the duration of the test. The heater for this test is known to be turned on at  $t = 37$  minutes, however the most prominent indication of the increasing time of flight occurs at  $t = 60$  minutes for Channels 5-8 and 90 minutes for Channels 1-4.

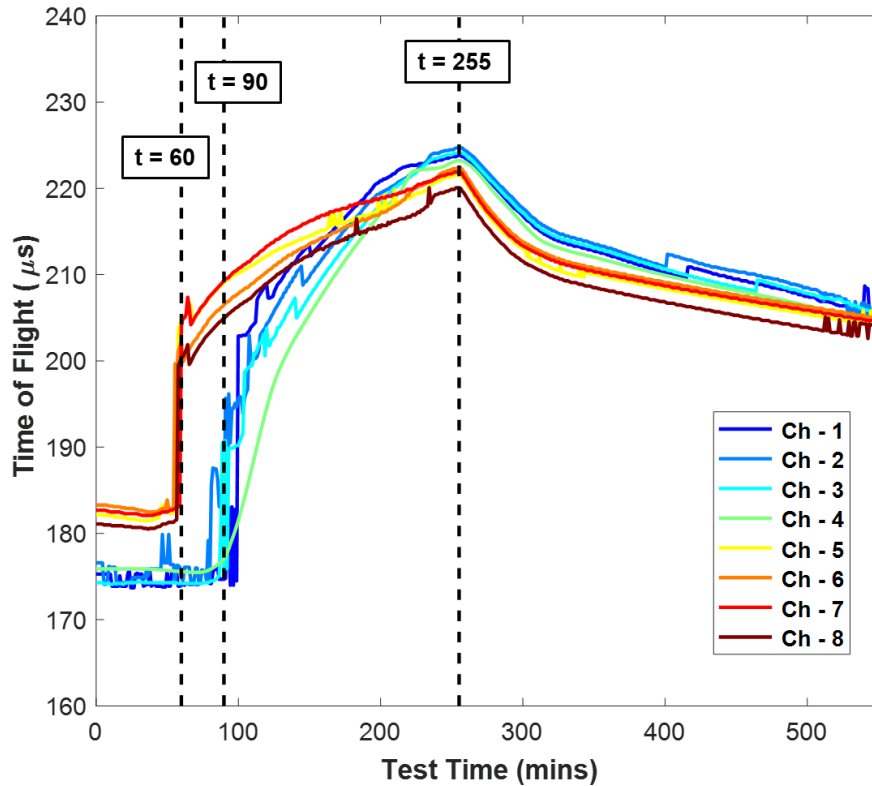


Figure 4.10. Time of flight curves with notable times.

Defining when the heater is on or off is important because of the effect it has on  $\Delta T$ . Recall that  $\Delta T$  is the temperature difference between the molten wax and the melt temperature, and is defined by the piecewise function in equation 3.27. So, for this experiment, while the heater is on,  $t < 255.2$  minutes, the molten wax is at  $20^\circ\text{C}$  above the melt temperature of the wax. When the heater turns off,  $\Delta T$  linearly decreases from  $20^\circ\text{C}$  to  $0.1^\circ\text{C}$ , over a set period of time, defined by  $t_{\text{cooling}} = 150$  minutes. The molten wax is then at a constant  $\Delta T$  of  $0.1^\circ\text{C}$  until the end of the test.

The bulk speed of sound curves are calculated from the TOF curves for each channel using the methods from Chapter 3. Those are shown in Figure 4.11

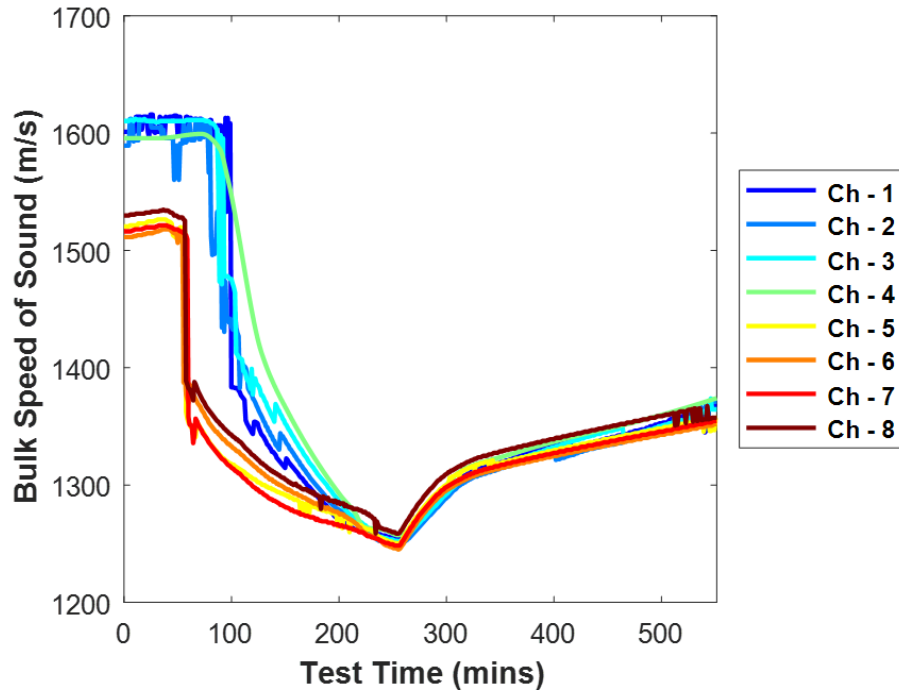


Figure 4.11. Bulk SOS curves for all 8 channels.

Recall that this experiment was left to cool for 24 hours, so it is likely that the temperature is approaching homogeneous across a single plane. Without an internal heat source, the wax will equilibrate to ambient temperature, given enough time. Looking at  $t < 100$  minutes, the bulk speed of sound is  $\sim 1625 \text{ m/s}$  for Channels 1-4. Based on the results from Figure 3.15, this corresponds to an isothermal effective temperature of  $24^\circ\text{C}$ . This is a reasonable number, given the ambient temperature of  $21^\circ\text{C}$ , residual heat left over from the previous day's testing, and the fact that the heater has not yet impacted the temperature state of the upper regions of the wax. This effective isothermal temperature is also checked against the internal temperatures measured by the thermocouples, shown in Figure 4.13, which confirm a range of  $20\text{-}30^\circ\text{C}$  for the bulk temperature across the upper plane that corresponds to transducer channels 1-4.

#### 4.2. Thermocouple Data

As discussed in Chapter 3, the 5-gallon experimental setup uses 17 internal thermocouples and 8 external thermocouples. The internal thermocouple temperatures are used exclusively to create 2D planar temperature approximations which are used to validate the results from the ultrasonic data, as is discussed later in this chapter. The numbering scheme for the internal thermocouples is shown in Figure 4.12.

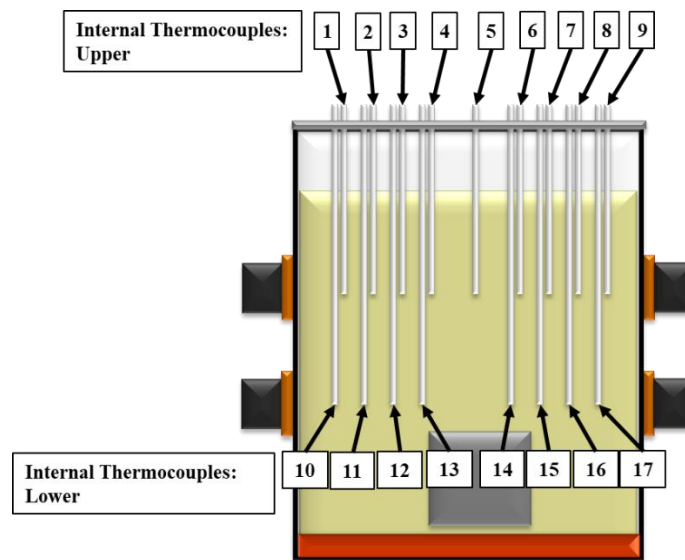


Figure 4.12. Internal thermocouple numbering scheme.

Thermocouple channels 1-9 are located on the same plane as the upper ring of transducers, while 10-17 are on the same plane as the lower ring of transducers. Figure 4.13 displays the monitored internal temperatures measured by the internal thermocouples as the test progresses. Recall that when the test began, there was a thermal gradient within the wax. Note that thermocouples 1 and 10 are the slowest to increase in temperature and are located on the outer edge of the same side of the container. Interestingly, the container does not heat symmetrically, as can be seen by TC9 and

TC17, the mirrored pair with TC1 and TC10. TC9 and TC17 reach  $T_{\text{melt}}$  nearly an hour before the corresponding thermocouples on the opposite side.

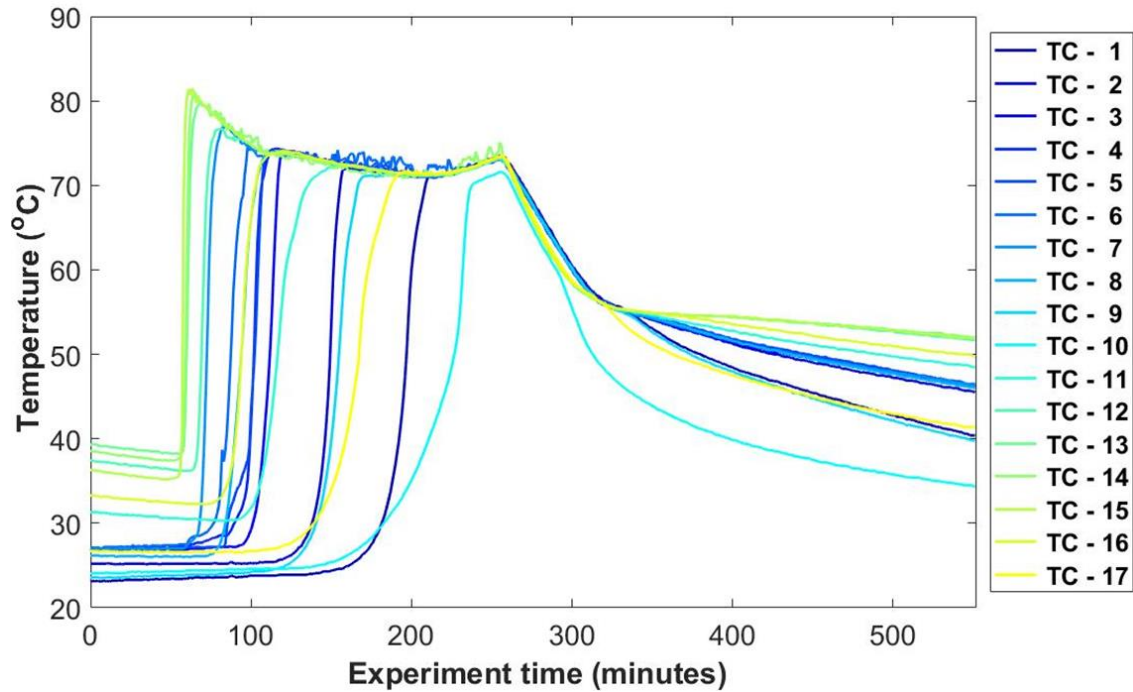


Figure 4.13. Internal thermocouple temperatures.

Notice that the internal thermal gradient present in the CBL-125 can be seen at the beginning of the test, prior to the heater being turned on 37 minutes into the test. Internal temperatures as recorded by the thermocouples initially read between 22 and 40 degrees Celsius, with the lower thermocouples reading between 30°C and 40°C, and the upper thermocouples reading between 22°C and 28°C. It is also interesting to observe that the outer thermocouples indicate a temperature lower than that of the interior thermocouples.

Recall that there are eight surfaces mounted externally. These thermocouples are used as boundary conditions for the ultrasonic data and are used in the analysis of the

radial temperature profile, as discussed in Section 3.5. They are numbered as shown in Figure 4.14.

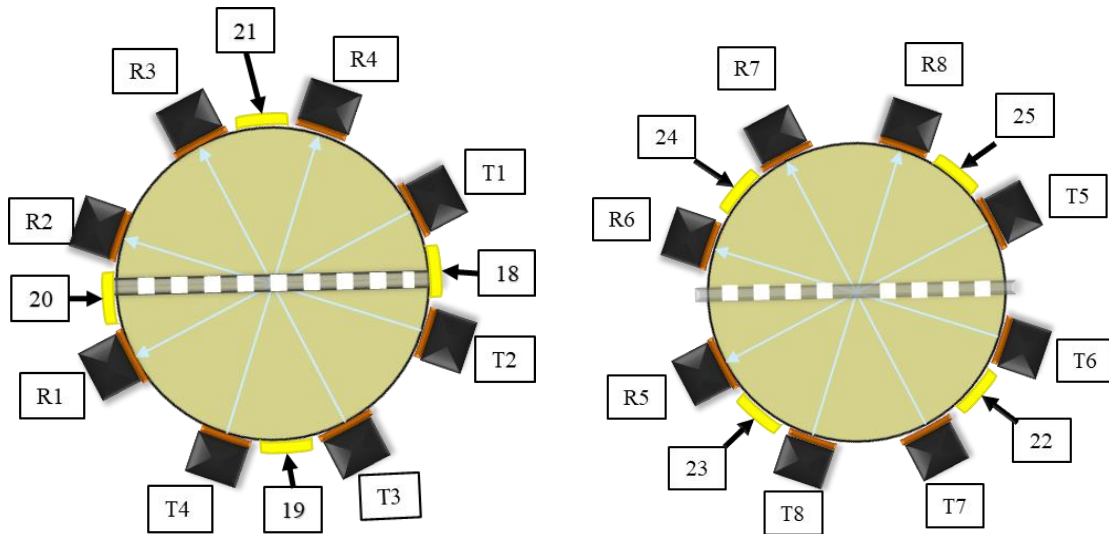


Figure 4.14. Location and labeling of external transducers and thermocouples on the upper plane (left) and lower plane (right).

The external thermocouples 18-21 are located between the upper transducers (channels 1-4), and external thermocouples 22-25 are located between the lower transducers (channels 5-8). Figure 4.15 shows the recorded data from the external thermocouples over the duration of this experiment. It is interesting to observe that the temperatures of the surface mounted external thermocouples increase by  $\sim 2^{\circ}\text{C}$  during the first 140-150 minutes of the test. Using only this data, “melt” would not be identified until that time frame, which is over 100 minutes after the heater is turned on. Comparing this to the “melt” which is observed by examining the internal temperature data, beginning at  $\sim 60$  minutes, the lag between internal and external temperature measurements as the wax heats is approximately 80 minutes. Interestingly, there is almost no lag as the wax cools. The heater is turned off 254 minutes into the test, and the

temperatures recorded by the surface mounted external thermocouples begin to decrease almost immediately, as do the temperatures recorded by the internal thermocouples. Using only external thermocouples, the wax could be considered to have resolidified by ~300 minutes. However the internal thermocouples indicate resolidification occurs after 400 minutes, if at all.

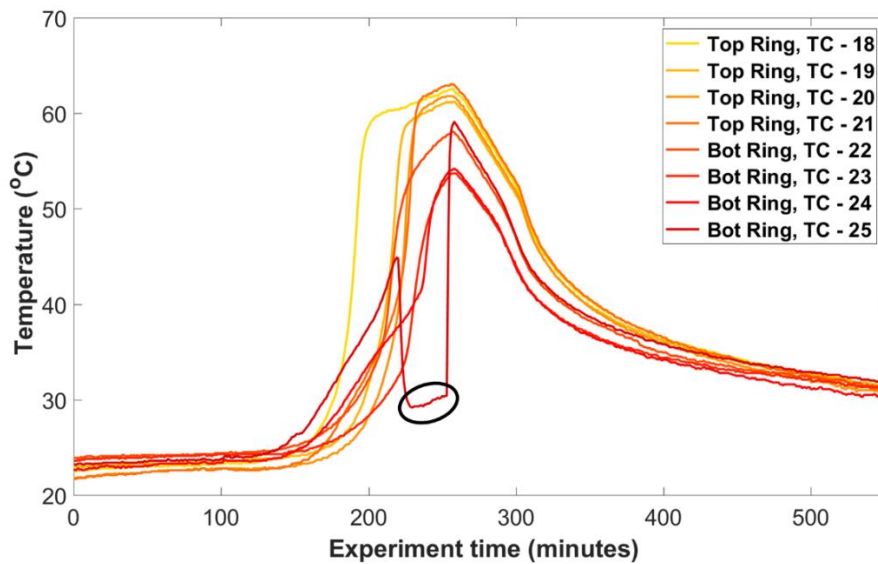


Figure 4.15. External thermocouples

Note that thermocouple 25 was observed at 259 minutes to have become detached from the container wall and it was remounted. It can be observed from Figure 4.15 that it became detached at 220 minutes into the test. To compensate for this, an average is taken for the upper and lower values, resulting in a single boundary condition across the four ultrasonic paths per plane. But during the time  $220 < t < 259$ , the results from TC25 required special consideration.

A linear fit and a spline fit for TC25 are visually compared for the best match to the heating trends of the other external thermocouples around the lower ring of

transducers and is shown in Figure 4.16. For the subsequent analysis, the spline fit was chosen as the results aligned best with the expected trends of the surround thermocouples. The boundary condition data for thermocouple 25 from 220 minutes to 259 minutes is replaced, as shown in Figure 4.16. The spline is a third-order polynomial which is fitted to the recorded data from 217-219 minutes and the data from 260-262 minutes.

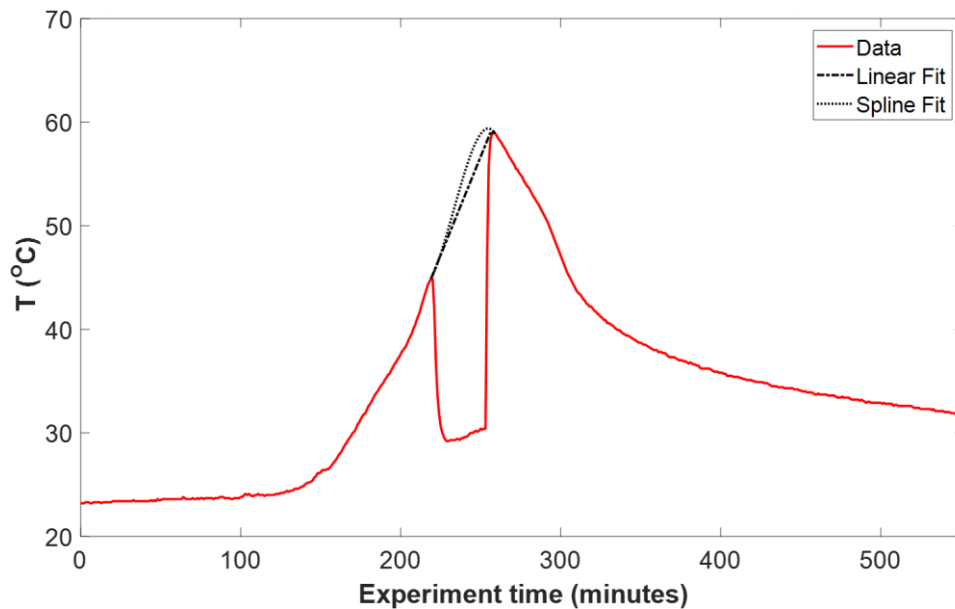


Figure 4.16 Comparison of linear and spline fits for TC25.

### 4.3 2D Approximated Temperature Profiles

Using the approach detailed in Section 3.5, the ultrasonic data from this test is analyzed, and radial temperature approximations are calculated. The comparison of approximate time of flight to measured time of flight is shown in Figure 4.17 for Channel 5.

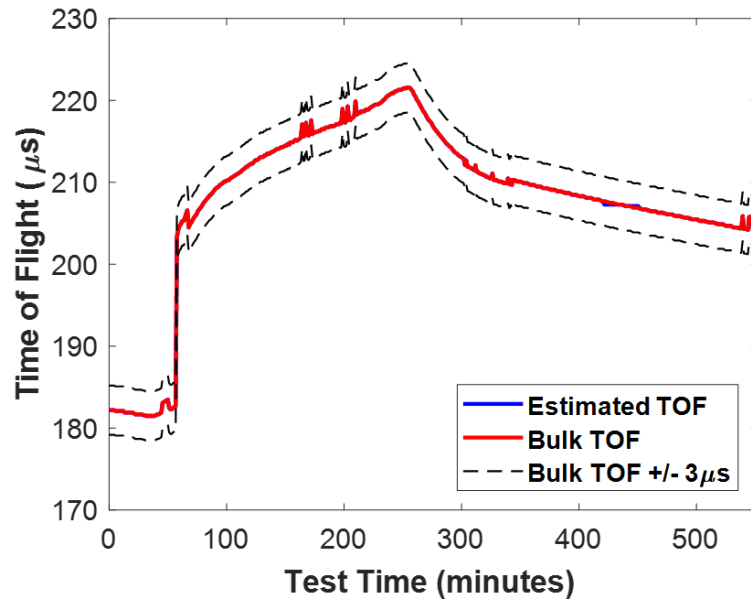


Figure 4.17. Comparison of measured TOF and approximate TOF for Channel 5.

Note that there is good agreement between the measured and approximate results, however there is some deviation as the wax cools. The plots for the other channels are contained in Appendix A. Using the radial temperature approximation, a plot of the radial temperature over time for Channel 5 is shown in Figure 4.18.

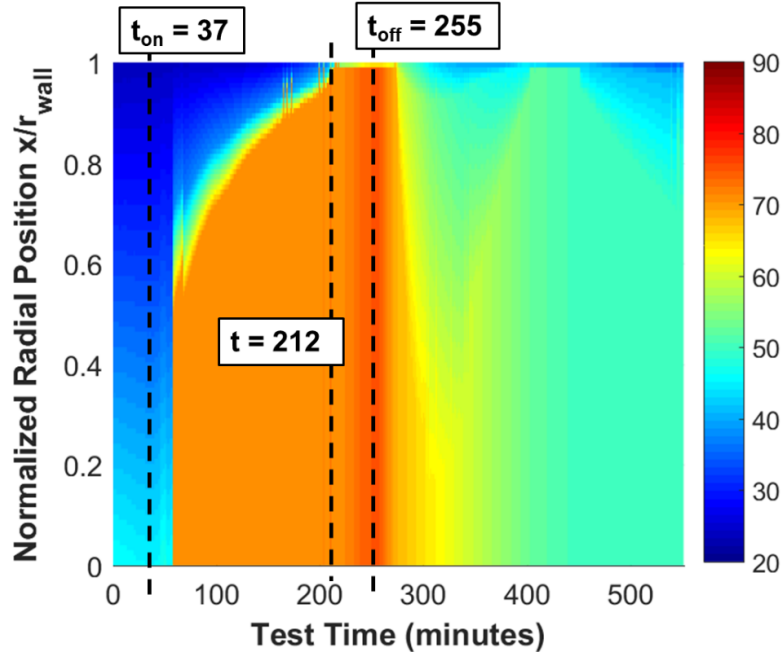


Figure 4.18. Radial temperature over time for Channel 5.

Times of interest are marked on the plot: heater on at  $t = 37$  minutes, fully melted at  $t = 212$  minutes, and heater off at  $t = 255$  minutes. Radial temperature plots for the other channels are shown without times of interest in Appendix A.

Using the approach detailed in Section 3.6, the 2D temperature approximations are provided in the section at select moments in time. These results are shown side-by-side with the results obtained by the thermocouples. In each set of images provided, the 2D temperature approximation from the internal thermocouples is shown on the left, and the 2D temperature approximation from the ultrasonic time of flight data is shown on the right. Temperatures are shown in degrees Celsius.

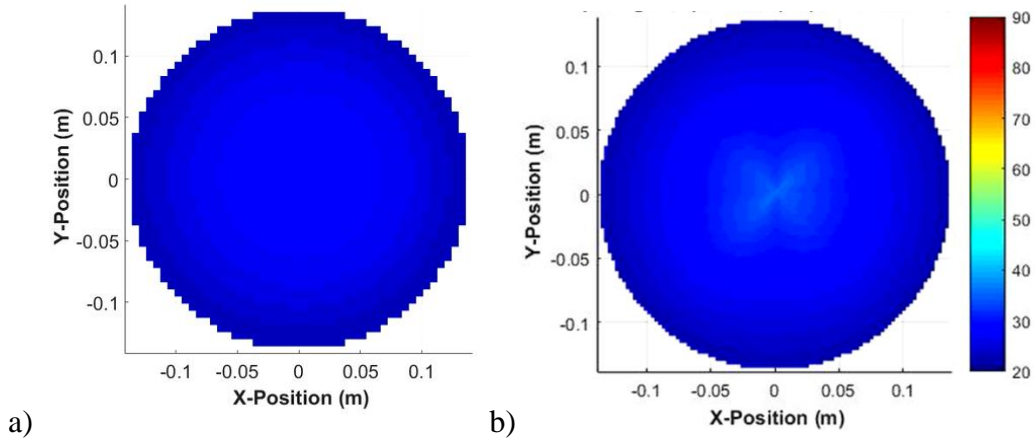


Figure 4.19 Top xy-plane temperature at  $t_{\text{experiment}} = 0$  minutes, a) experimental observation, b) approximated temperature state from acoustic measurements.

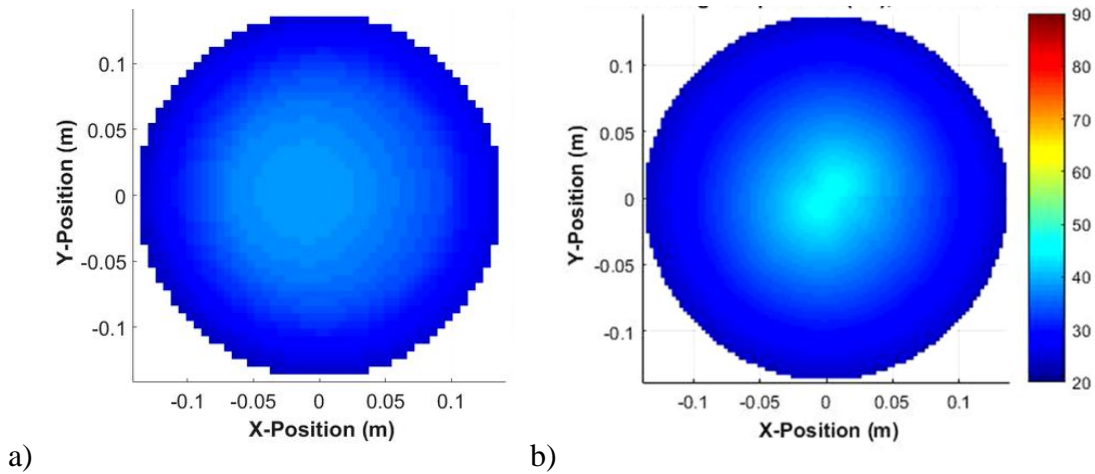


Figure 4.20 Bottom xy-plane temperature at  $t_{\text{experiment}} = 0$  minutes, a) experimental observation, b) approximated temperature state from acoustic measurements.

The first set of results shown is for the initial temperature state at  $t = 0$  minutes, and is shown in Figure 4.19 and Figure 4.20 for, respectively, the upper and lower ring of transducers. The temperature distributions for the top and bottom xy-plane show good agreement between the thermocouple and speed of sound approximations. Recall that the thermocouples are a single linear array across the diameter of the container. Thus, the 2D approximation based on thermocouples is symmetric about  $y = 0$ , while the speed of sound 2D temperature approximation is not held to the same limitation.

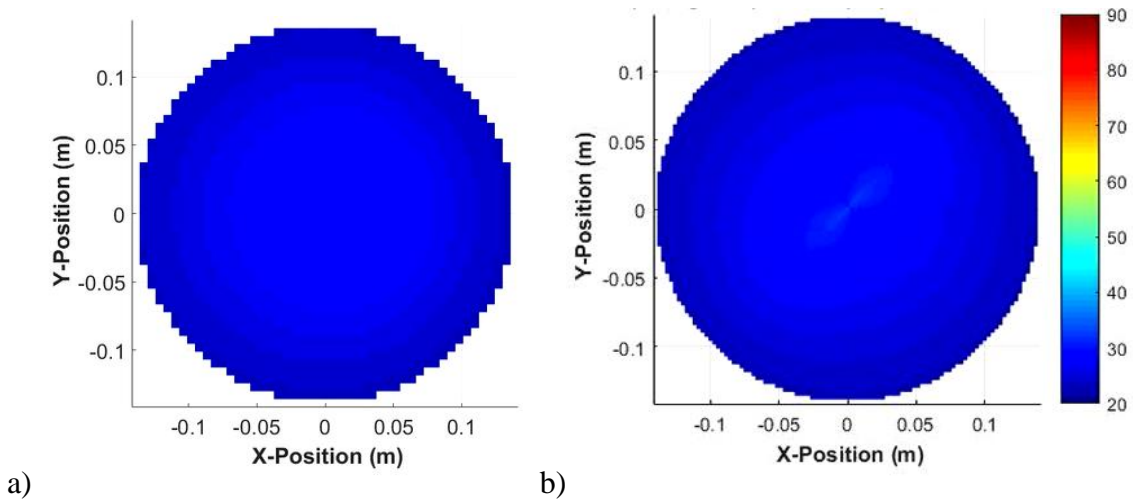


Figure 4.21 Top xy-plane temperature at  $t_{\text{experiment}} = 66$  minutes, a) experimental observation, b) approximated temperature state from acoustic measurements.

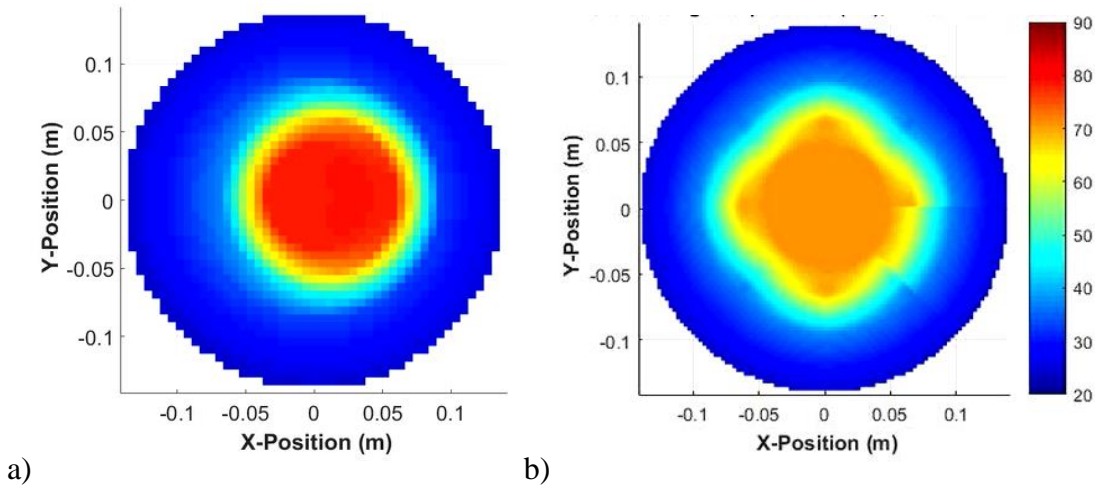


Figure 4.22 Bottom xy-plane temperature at  $t_{\text{experiment}} = 66$  minutes, a) experimental observation, b) approximated temperature state from acoustic measurements.

A  $t = 66$  minutes, the lower xy-plane began to melt near the center, beginning internally and spreading towards the edges of the container. The  $\Delta T$  approximation defined in the MATLAB code limits the molten wax temperature to be  $T_{\text{melt}} + 20^\circ\text{C}$ , which, in this scenario corresponds to  $70.4^\circ\text{C}$ , so long as the wax is not fully molten. The observed temperature of the wax during this initial melting period is approximately  $10^\circ\text{C}$  higher than the estimated  $70.4^\circ\text{C}$ , however the melt front locations are similar. The

internal temperature state at  $t = 127$  minutes is shown in Figure 4.23 and Figure 4.24. The estimated  $\Delta T$  value of the molten wax more closely matches that recorded by the thermocouples. The melt radius and size of the molten wax areas are comparable for both upper and lower planes when looking at the thermocouple and speed of sound approximations. Recall, this time is when heating is underway, and the molten wax boundary has not reached the walls of the container.

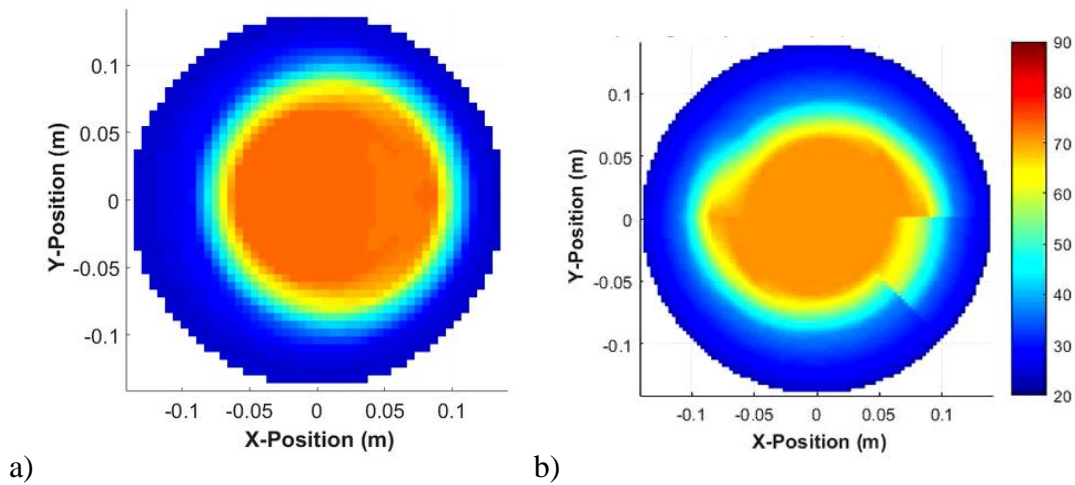


Figure 4.23 Top xy-plane temperature at  $t_{\text{experiment}} = 127$  minutes, a) experimental observation, b) approximated temperature state from acoustic measurements.

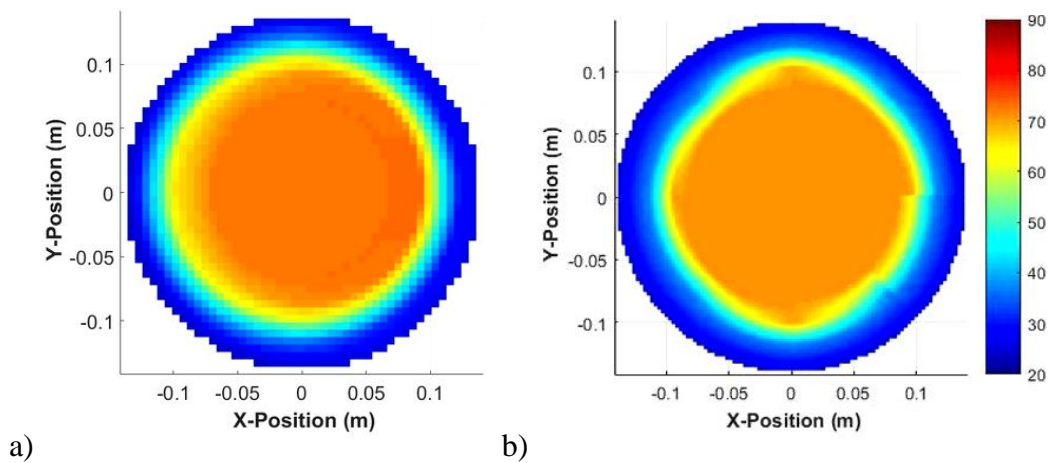


Figure 4.24 Bottom xy-plane temperature at  $t_{\text{experiment}} = 127$  minutes, a) experimental observation, b) approximated temperature state from acoustic measurements.

At 205 minutes into the test, the top and bottom xy-planes are both nearing fully melted. This is shown in the physical measurements of temperature and the temperature estimated from the acoustics, as shown in Figure 4.25 and Figure 4.26. There is very good agreement between the two methods as the wax continues to heat at both the upper and lower rings of transducers.

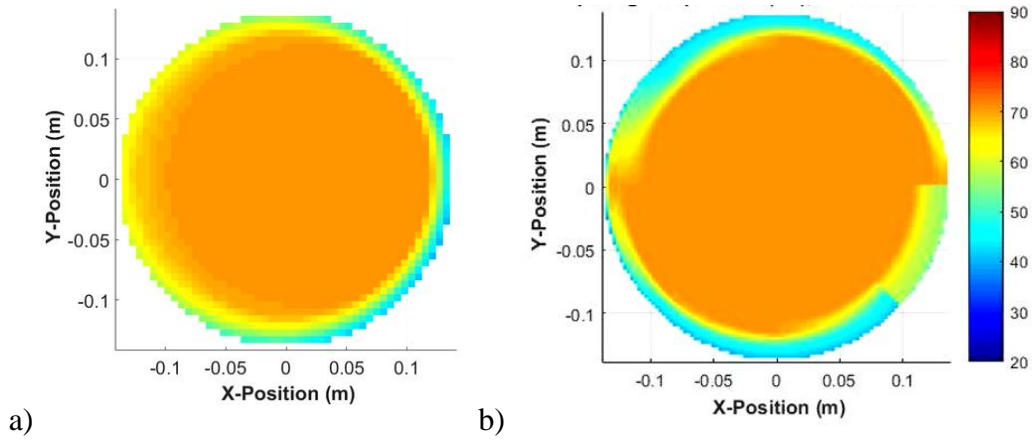


Figure 4.25 Top xy-plane temperature at  $t_{\text{experiment}} = 205$  minutes, a) experimental observation, b) approximated temperature state from acoustic measurements.

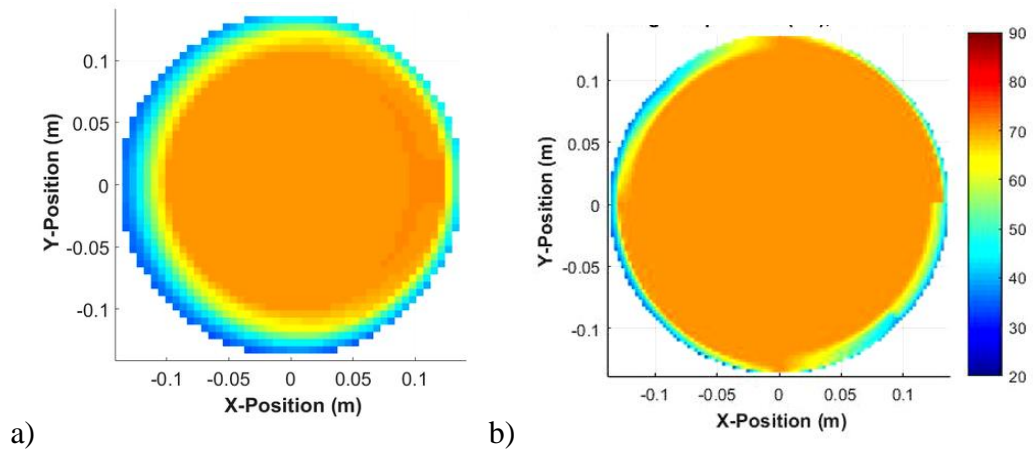


Figure 4.26 Bottom xy-plane temperature at  $t_{\text{experiment}} = 205$  minutes, a) experimental observation, b) approximated temperature state from acoustic measurements.

When the container is fully melted, the ultrasonic temperature approximation assumes a uniform temperature inside the container, with a brief temperature gradient along the edge of the container. This is shown in Figure 4.27 and Figure 4.28 for  $t = 233$  minutes. The heater is still on, and  $\Delta T$  is now affected by the X parameter, allowing it to increase above  $20^\circ\text{C}$  as discussed in Section 3.5.

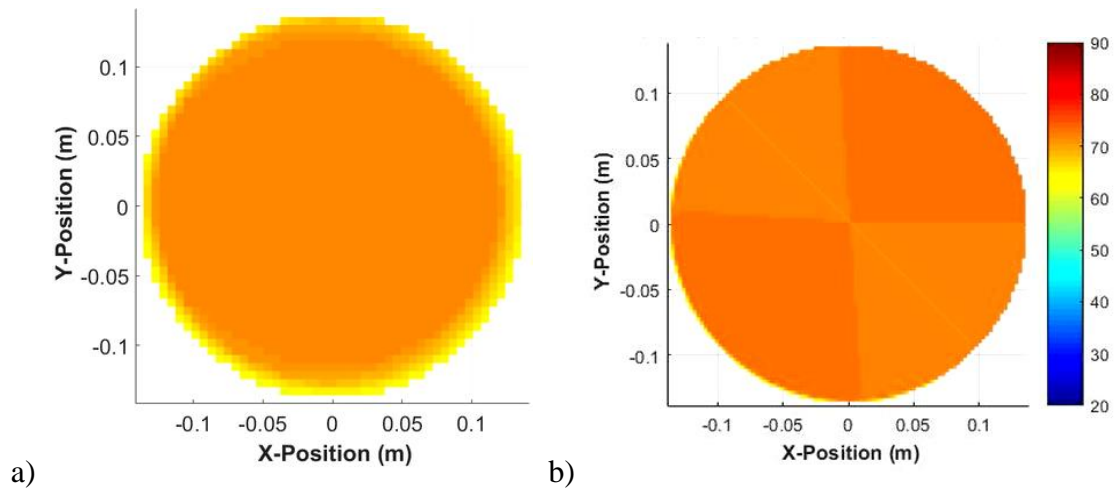


Figure 4.27 Top xy-plane temperature at  $t_{\text{experiment}} = 233$  minutes, a) experimental observation, b) approximated temperature state from acoustic measurements.

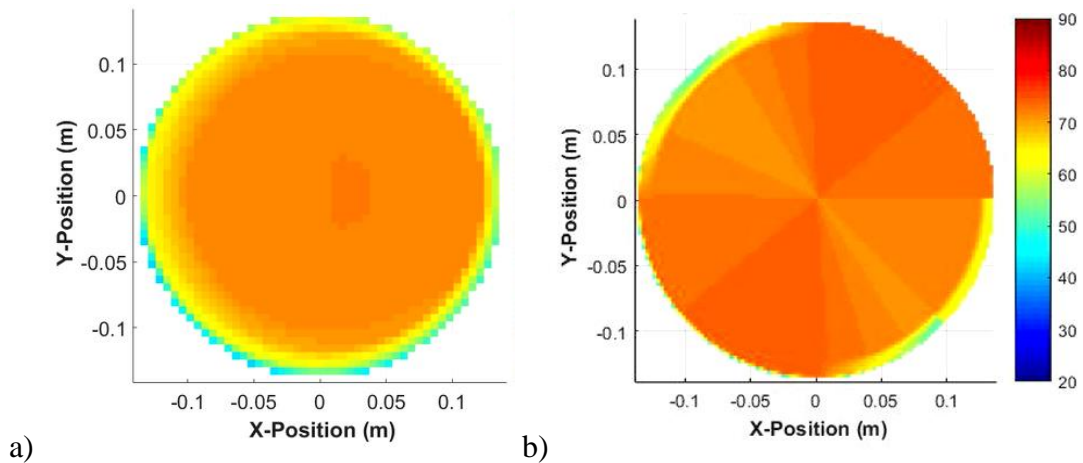


Figure 4.28 Bottom xy-plane temperature at  $t_{\text{experiment}} = 233$  minutes, a) experimental observation, b) approximated temperature state from acoustic measurements.

At 254 minutes into the test, the wax is nearing its hottest temperature, as seen in Figure 4.29 and Figure 4.30. Recall that the heater is turned off 255.2 minutes into the experiment. Note that the wall temperature measured by the external thermocouples is high enough that the gradient between the molten wax and wall temperature, which occurs along the edges of the container, is difficult to see visually.

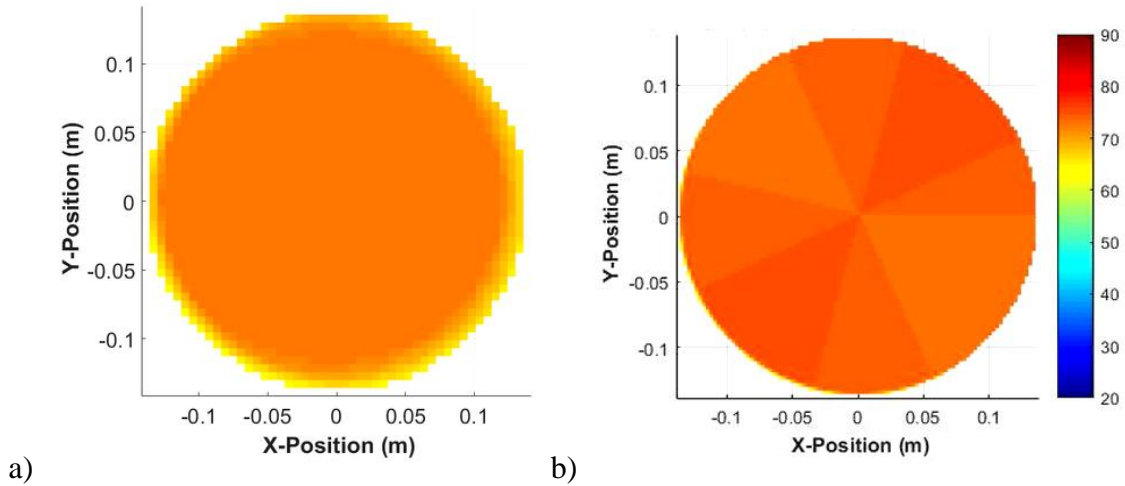


Figure 4.29. Top xy-plane temperature at  $t_{\text{experiment}} = 254$  minutes, a) experimental observation, b) approximated temperature state from acoustic measurements.

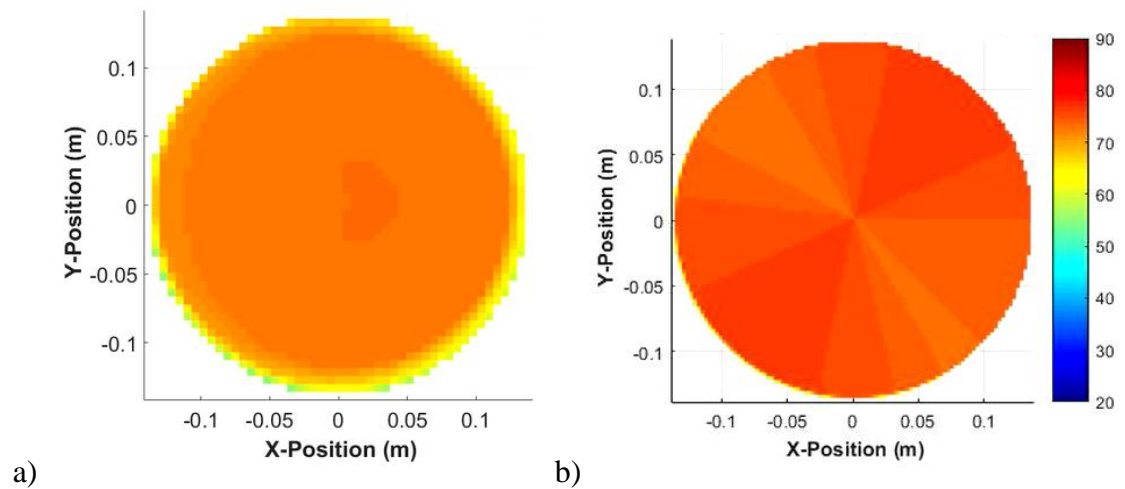


Figure 4.30. Bottom xy-plane temperature at  $t_{\text{experiment}} = 254$  minutes, a) experimental observation, b) approximated temperature state from acoustic measurements.

The transition period, where  $\Delta T$  is linearly decreasing from  $20^{\circ}\text{C}$  to  $0.1^{\circ}\text{C}$ , note that not all the radial temperature profiles on a plane appear to be using the same “bin” of  $X$  parameter. On the bottom plane in Figure 4.32, there is a visible difference between the temperature approximation for certain channels, which indicates that the temperature profiles for some channels may be approximated as fully melted, with  $X > r_{\text{wall}}$ , while other are approximated as partially melted, with  $r_{\text{melt}} < X < r_{\text{wall}}$ . At this moment in time, that does not appear to occur in the upper plane seen in Figure 4.31.

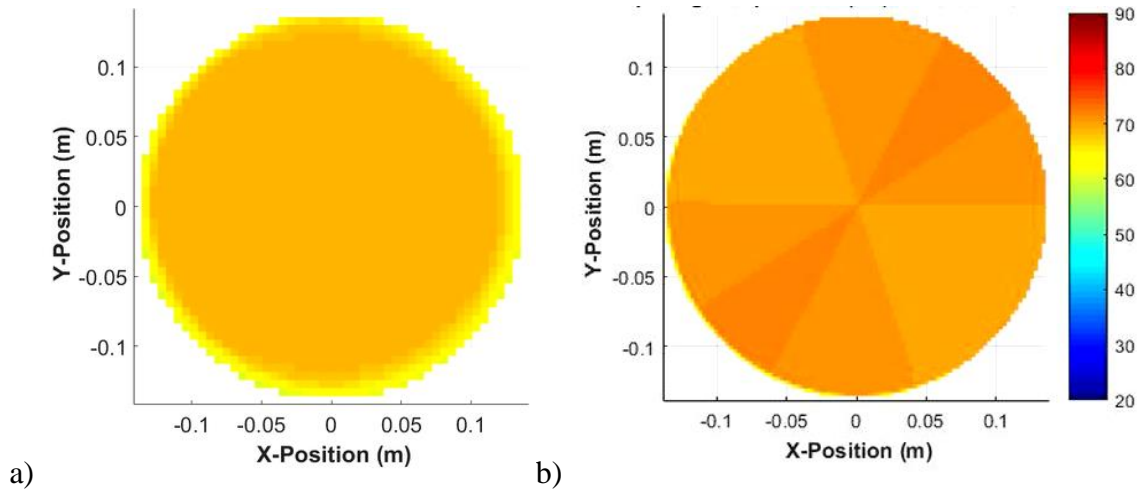


Figure 4.31 Top xy-plane temperature at  $t_{\text{experiment}} = 272$  minutes, a) experimental observation, b) approximated temperature state from acoustic measurements.

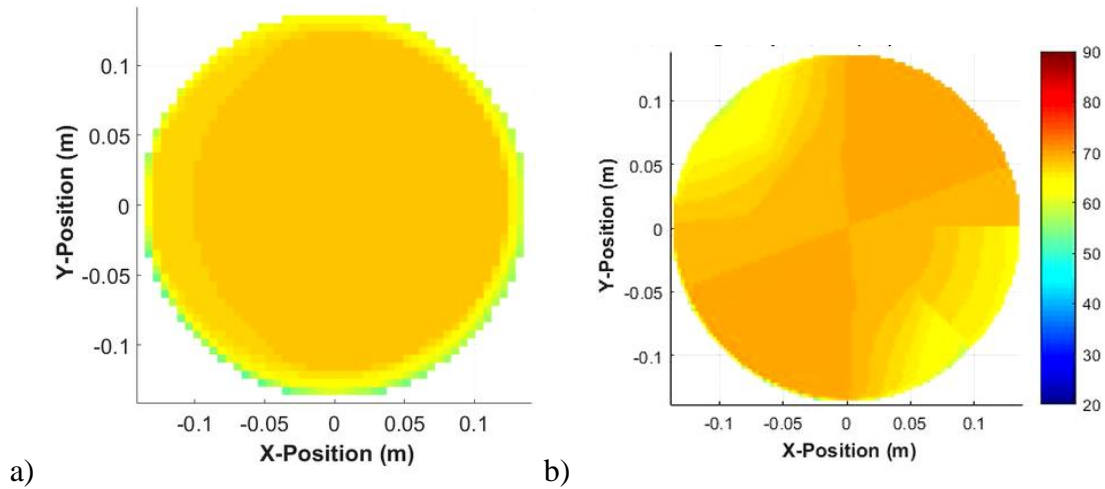


Figure 4.32 Bottom xy-plane temperature at  $t_{\text{experiment}} = 272$  minutes, a) experimental observation, b) approximated temperature state from acoustic measurements.

As the wax cools inside the container, the largest temperature gradients across the xy-planes are found near the edges of the container, as shown by the internal thermocouple data. As discussed in Section 3.5.2, the radial temperature profiles created from ultrasonic data are designed to reflect this. However, as shown in Figure 4.33 and Figure 4.34, for  $t = 310$  minutes, the ultrasonic temperature approximations are visually predicting a slightly elevated temperature near the center of the container.

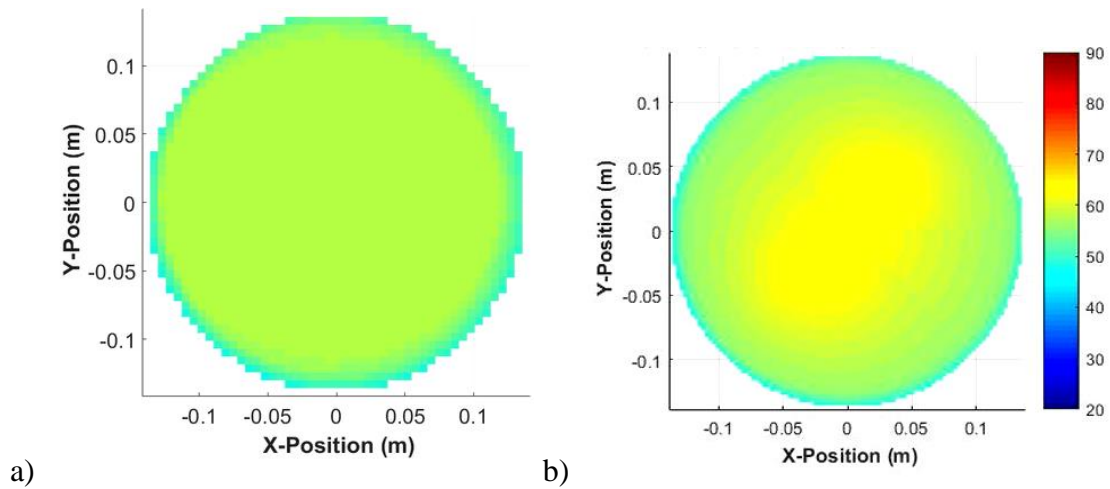


Figure 4.33. Top xy-plane temperature at  $t_{\text{experiment}} = 310$  minutes, a) experimental observation, b) approximated temperature state from acoustic measurements.

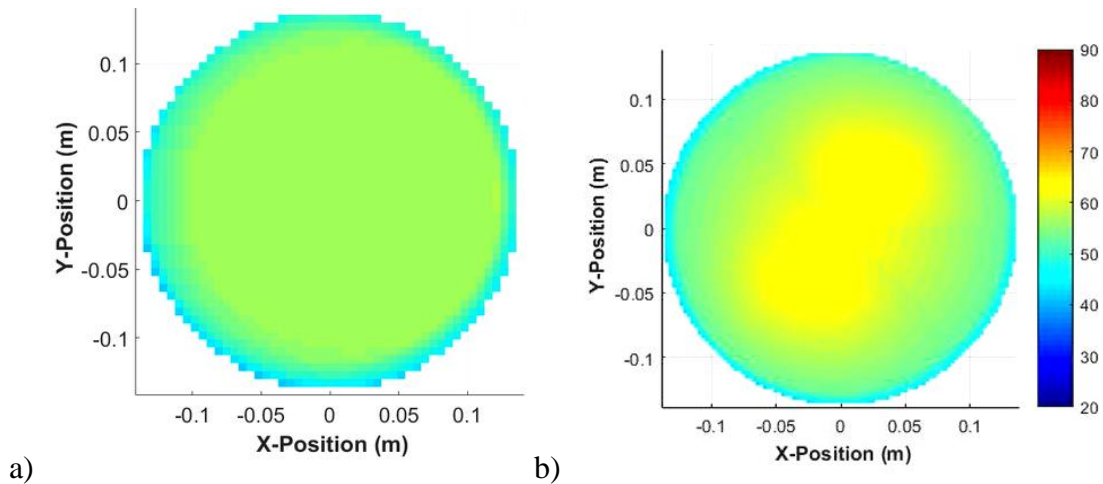


Figure 4.34 Bottom xy-plane temperature at  $t_{\text{experiment}} = 310$  minutes, a) experimental observation, b) approximated temperature state from acoustic measurements.

At  $t = 366$  minutes, the molten wax continues to cool, with the top plane cooling more uniformly than the bottom plane as noted in the thermocouple approximation shown in Figure 4.35 and Figure 4.36. Recall that the top plane of transducers is located  $\sim 1$ -inch below the surface of the wax, while the bottom plane is 4-inches below the top plane. The bottom plane is observed to cool from the outside in, whereas the top ring has cooling from the outside in but is also affected by surface convection of the top surface to the ambient temperature. At present, the 2D temperature approximation based on ultrasonic data does not differentiate between the top and bottom planes of transducers, and yet the results are in reasonable agreement with experimental observations.

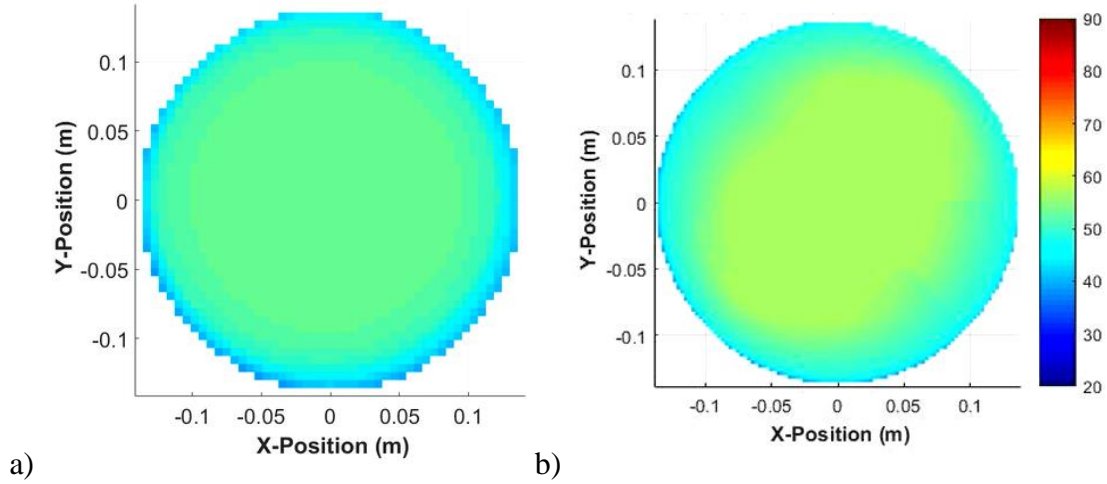


Figure 4.35 Top xy-plane temperature at  $t_{\text{experiment}} = 366$  minutes, a) experimental observation, b) approximated temperature state from acoustic measurements.

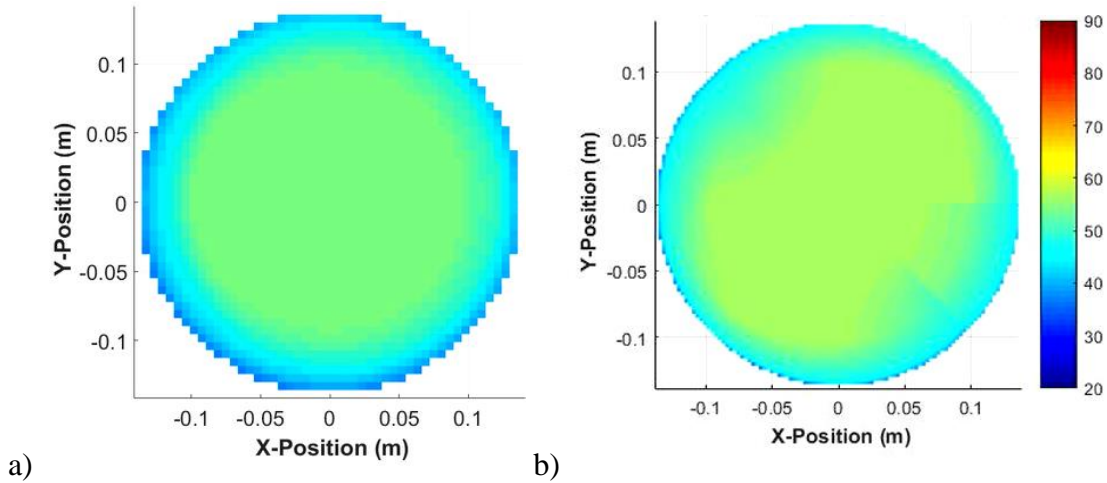


Figure 4.36 Bottom xy-plane temperature at  $t_{\text{experiment}} = 366$  minutes, a) experimental observation, b) approximated temperature state from acoustic measurements.

As the wax continues to cool, the core temperature across the top xy-plane approaches  $T_{\text{melt}}$  as observed in Figure 4.37 at  $t = 497$  minutes. The lower plane, shown in Figure 4.38, exhibits a higher temperature gradient around the edges of the container than the upper plan, but the results continue to be in reasonable agreement.

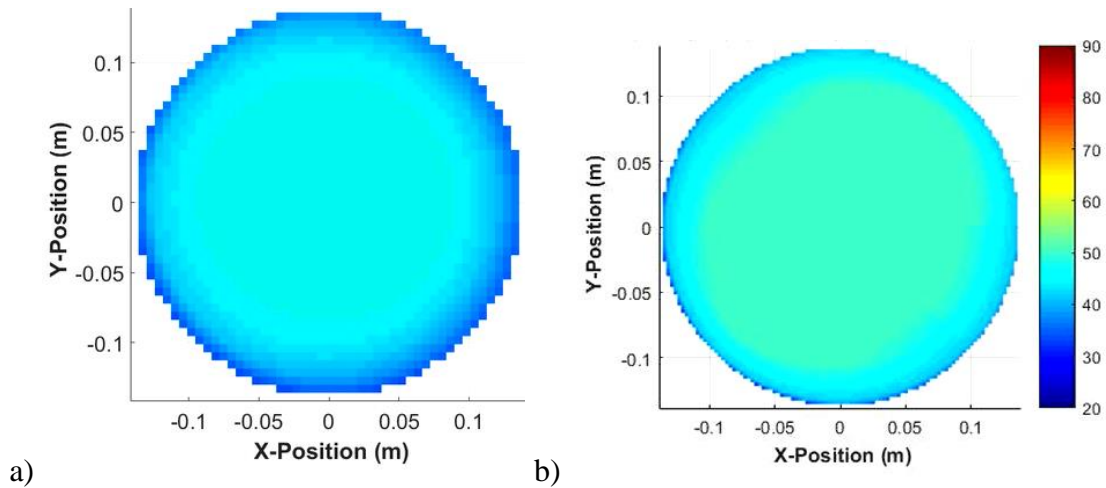


Figure 4.37 Top xy-plane temperature at  $t_{\text{experiment}} = 497$  minutes, a) experimental observation, b) approximated temperature state from acoustic measurements.

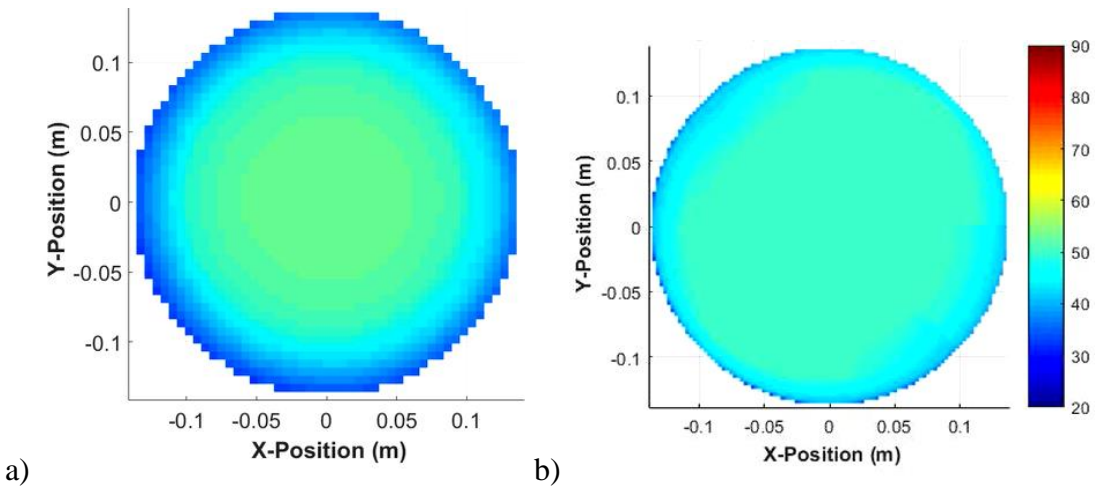


Figure 4.38 Bottom xy-plane temperature at  $t_{\text{experiment}} = 497$  minutes, a) experimental observation, b) approximated temperature state from acoustic measurements.

When the test concludes, both the upper and lower planes continue to have a varying internal temperature state, or, in the case of the lower plane, it is not yet fully solidified. The average 2D temperature approximation is within 5 degrees Celsius for both planes at the end of the test.

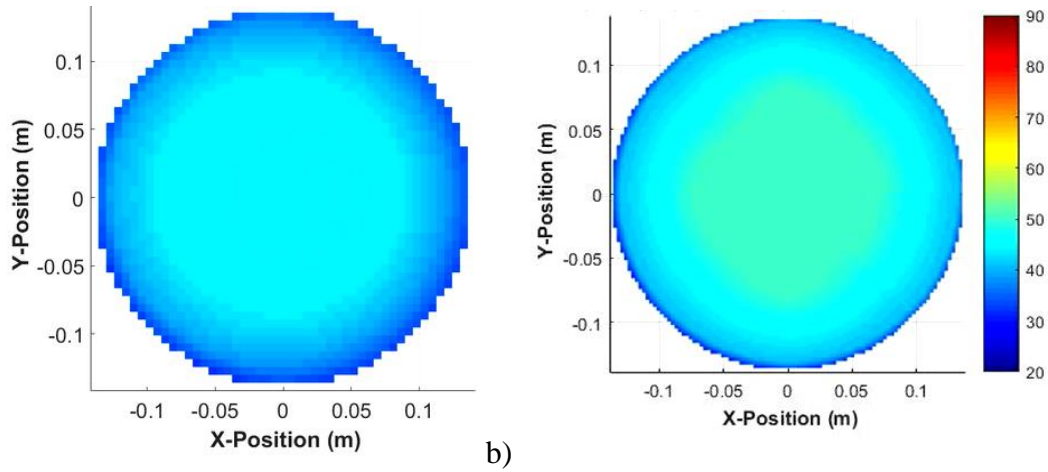


Figure 4.39 Top xy-plane temperature at  $t_{\text{experiment}} = 552$  minutes, a) experimental observation, b) approximated temperature state from acoustic measurements.

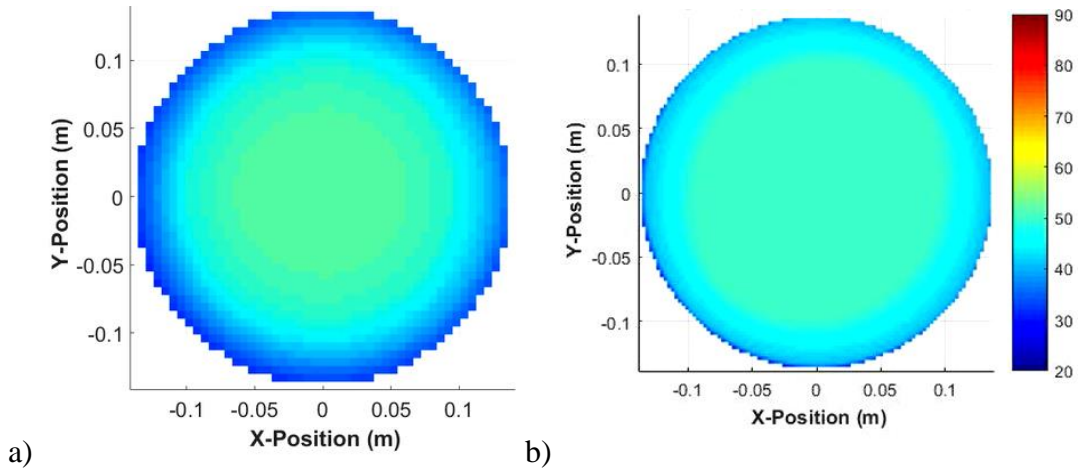


Figure 4.40 Bottom xy-plane temperature at  $t_{\text{experiment}} = 552$  minutes, a) experimental observation, b) approximated temperature state from acoustic measurements.

The results of the 2D temperature approximations based on the ultrasonic data are compared to the 2D temperature approximations based on the thermocouple data over the entire test. The results are compared by taking the difference between the approximation from acoustic data and the approximation from thermocouple data across the entire area at each moment in time. The difference is over the area, and the absolute value of that set of temperature differences is averaged for each moment in time. This is done for both the

top and the bottom plane, and the resulting average planar temperature difference is shown in Figure 4.41.

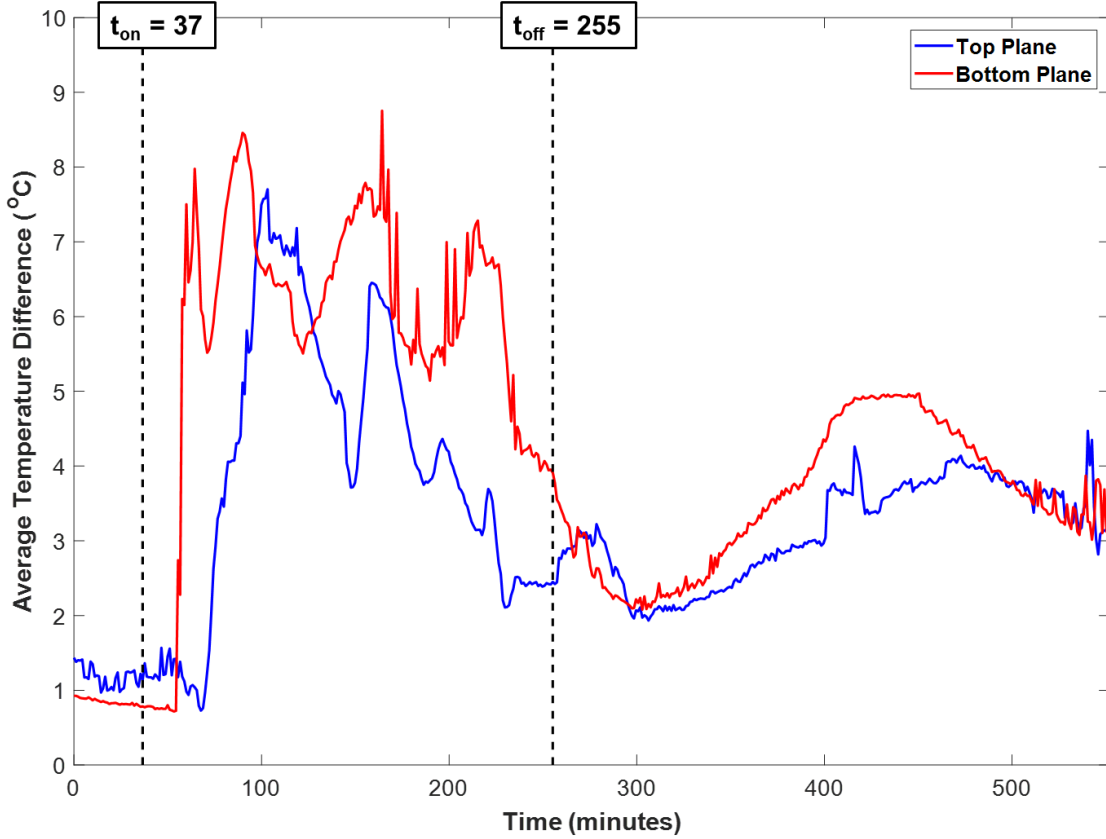


Figure 4.41 Average temperature difference between ultrasonic and thermocouple 2D temperature approximations over time.

For both planes, the largest difference between the average of the ultrasonic and thermocouple approximations occurs during the heating period of the wax, after the heater is on and when  $\Delta T$  is a constant  $20^{\circ}\text{C}$ . The sharp increase that occurs for the top plane over  $69\text{min} < t < 103\text{min}$ , and for the bottom plane over  $54\text{min} < t < 60\text{min}$ , correspond to the time ranges when those planes see significant TOF change and temperature increase from the thermocouples. The mean difference between the 2D

approximations for the upper plane is  $3.34^{\circ}\text{C}$ , and the mean difference for the lower plane is  $4.26^{\circ}\text{C}$ . Recall that from the previous discussion of error in Section 3.4.4 that an effective temperature approximated from a time of flight measurement across the diameter has compounding error from the height and diameter measurements and the size of the transducer face, which were estimated to be  $\pm 2.7^{\circ}\text{C}$ , as well as the thickness of the ultem insulating plate, which was estimated to be  $\pm 0.81^{\circ}\text{C}$ . There is also some error associated with the TOF for each a-scan, as the sample above the detection threshold might not be a perfect representation of the onset time of the signal. Additionally, the K-type thermocouples used in this research have an associated error of  $\pm 0.41^{\circ}\text{C}$ . Taking into account these sources of error, and the calculations done previously, it is reasonable to consider that a temperature approximated from the ultrasonic data has an error of  $\pm 4.12^{\circ}\text{C}$ .

#### *4.4 Further Experimentation*

Using the same equipment and experimental setup as described, another experiment is conducted. The heater is turned on at the beginning of the test, and turned off at  $t = 110$  minutes, as indicated by the change in the time of flight curves from increasing to decreasing in Figure 4.42.

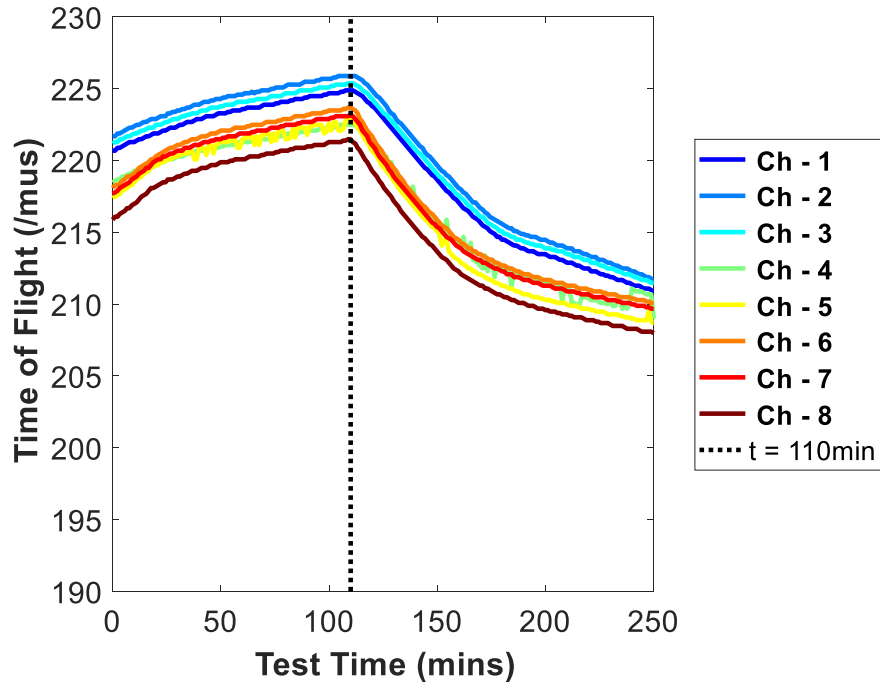


Figure 4.42 Time of flight curves.

During the initial heating of the wax, recall that  $T_{\text{molten}}$  is defined as  $70.4^{\circ}\text{C}$  by the temperature approximation algorithm. The wax begins nearly fully molten yet having cooled to a temperature below the assigned  $T_{\text{molten}}$ . Thus, predicted melt radius and molten temperature of the wax are different than the values indicated by the internal thermocouples on both the upper and lower planes Figure 4.43 and Figure 4.44.

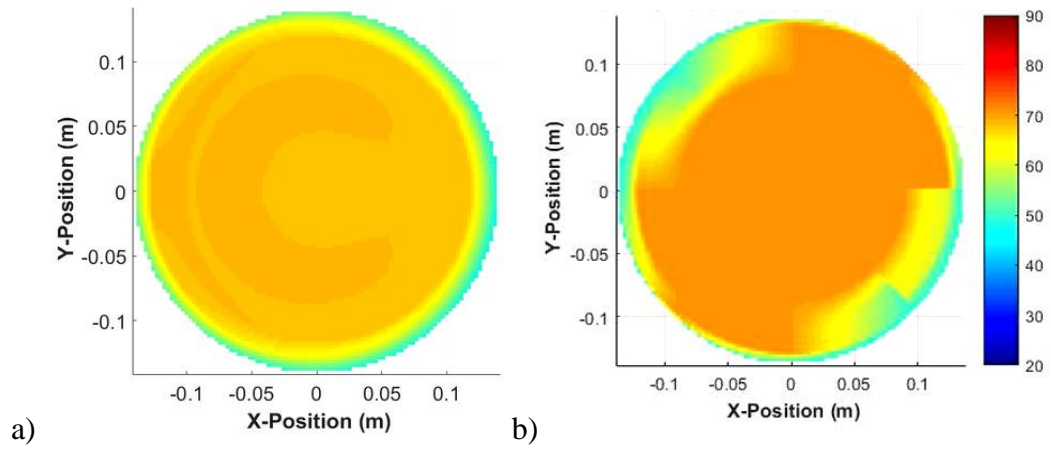


Figure 4.43 Top xy-plane temperature at  $t_{\text{experiment}} = 0$  minutes, a) experimental observation, b) approximated temperature state from acoustic measurements.

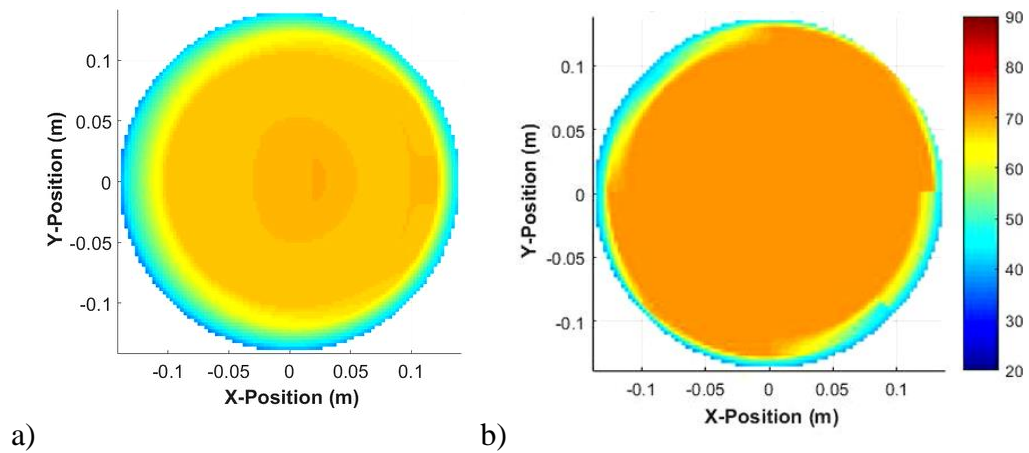


Figure 4.44 Bottom xy-plane temperature at  $t_{\text{experiment}} = 0$  minutes, a) experimental observation, b) approximated temperature state from acoustic measurements.

The wax continues to increase in temperature while the heater remains on, and the ultrasonic approximation reflects the overall change in temperature (Figure 4.45 and Figure 4.46).

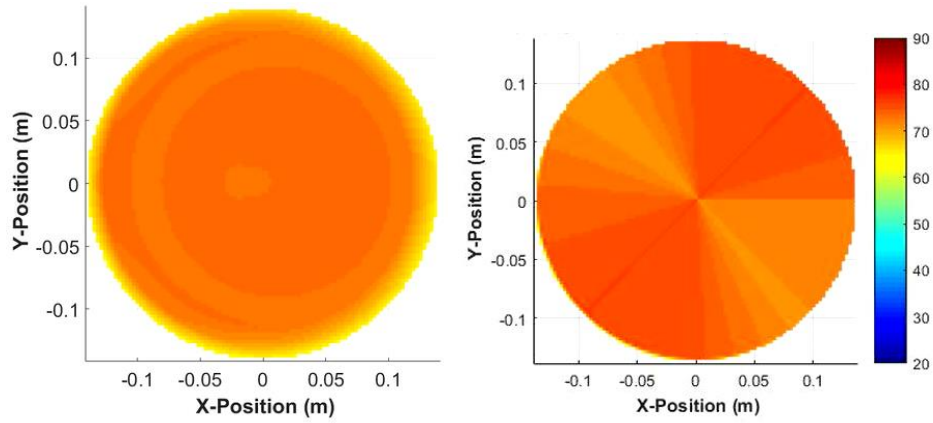


Figure 4.45 Top xy-plane temperature at  $t_{\text{experiment}} = 74$  minutes, a) experimental observation, b) approximated temperature state from acoustic measurements.

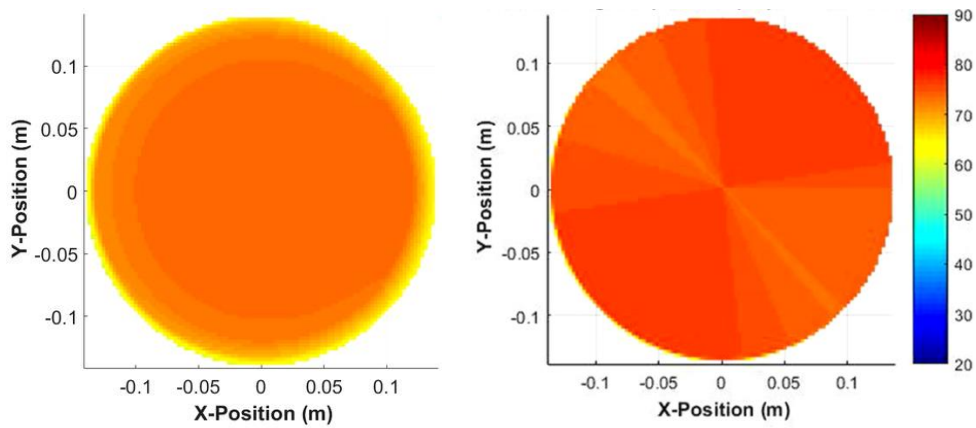


Figure 4.46 Bottom xy-plane temperature at  $t_{\text{experiment}} = 74$  minutes, a) experimental observation, b) approximated temperature state from acoustic measurements.

After the heater is turned off at  $t = 110$  minutes, the wax begins to cool and  $T_{\text{molten}}$  decreases by an estimate  $10\text{-}15^{\circ}\text{C}$  in 42 minutes, shown in Figure 4.47 and Figure 4.48.

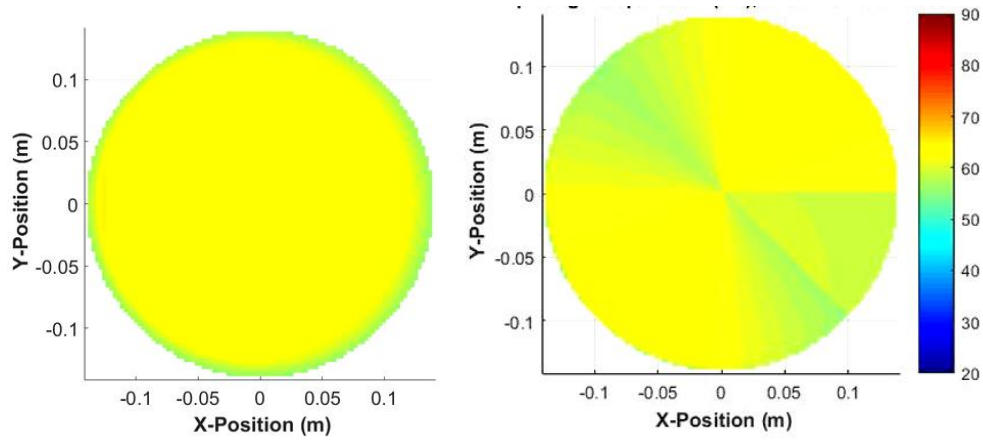


Figure 4.47 Top xy-plane temperature at  $t_{\text{experiment}} = 151$  minutes, a) experimental observation, b) approximated temperature state from acoustic measurements.

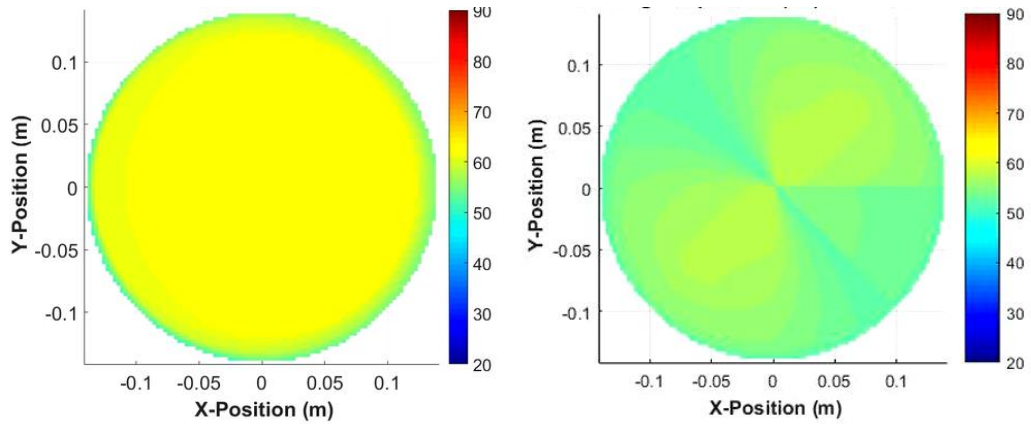


Figure 4.48 Bottom xy-plane temperature at  $t_{\text{experiment}} = 151$  minutes, a) experimental observation, b) approximated temperature state from acoustic measurements.

At the end of the experiment, when  $t = 249$  minutes, the molten wax is at approximately  $T_{\text{melt}}$  on the top plane (Figure 4.49), and approximately  $5^{\circ}\text{C}$  higher than that on the bottom plane, according to the thermocouple data (Figure 4.50).

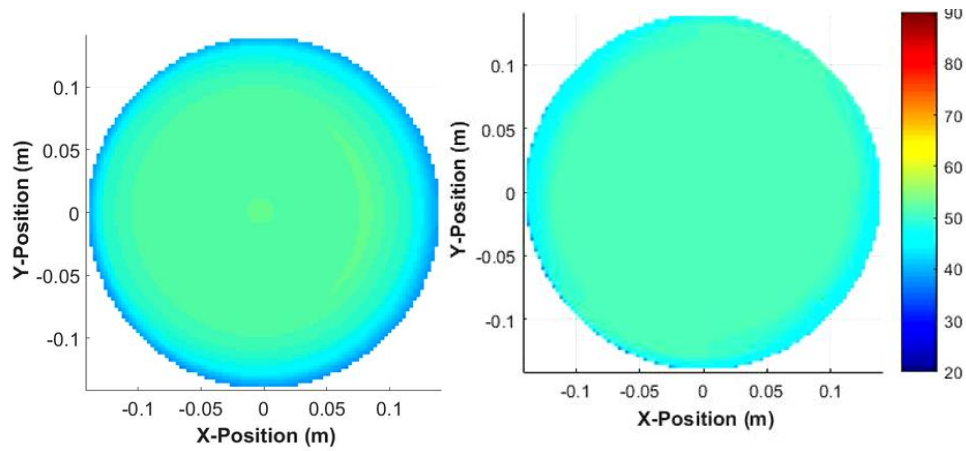


Figure 4.49 Top xy-plane temperature at  $t_{\text{experiment}} = 249$  minutes, a) experimental observation, b) approximated temperature state from acoustic measurements.

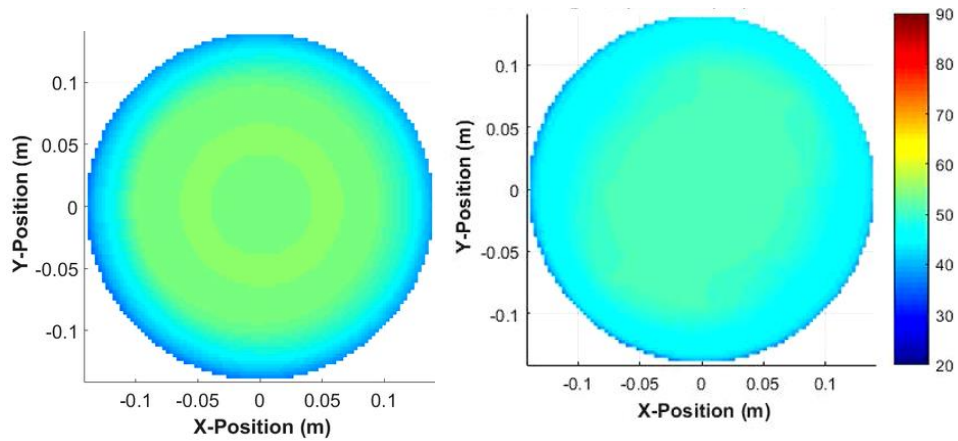


Figure 4.50 Bottom xy-plane temperature at  $t_{\text{experiment}} = 249$  minutes, a) experimental observation, b) approximated temperature state from acoustic measurements.

As done previously, a comparison of the 2D planar temperature approximation from the thermocouple data and the ultrasonic data is done, and the result is shown in Figure 4.51.

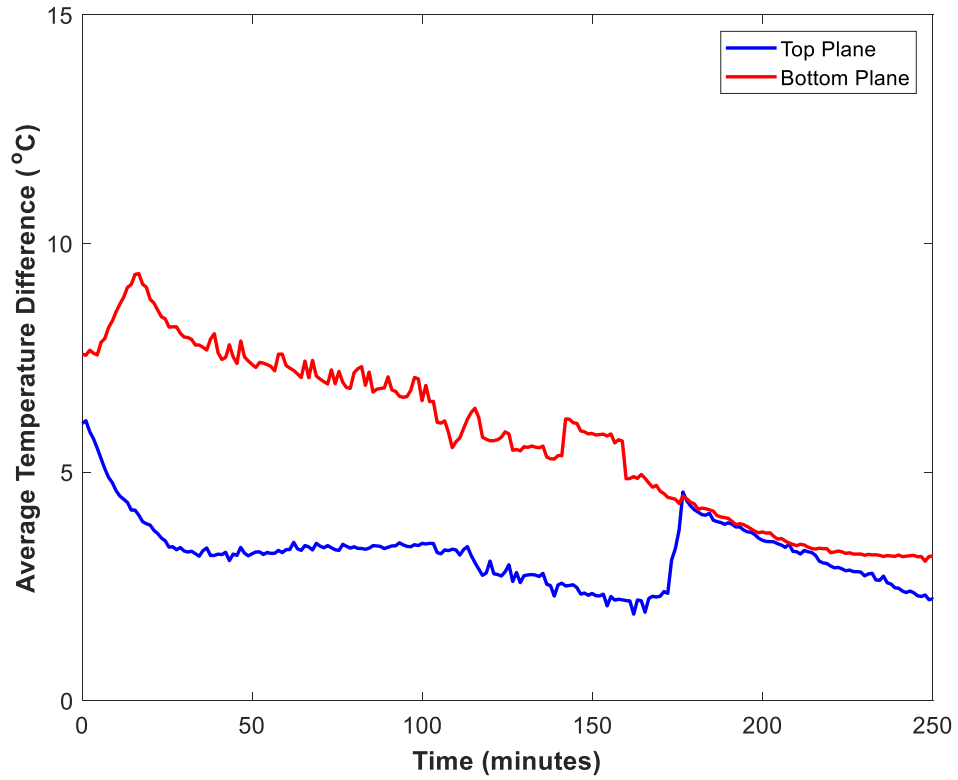


Figure 4.51 Average temperature difference between ultrasonic and thermocouple 2D temperature approximations over time.

The average temperature difference across the bottom plane is 5.89°C and across the top plane it is 3.60°C.

## CHAPTER FIVE

### Conclusions and Future Work

As additive manufacturing, food processing, petro-chemical, energy generation, and other industries continue to grow in complexity and size, the need to characterize the internal temperature and phase state of a material increases. Ultrasonic non-destructive evaluation is one method which may be used to evaluate these parameters.

This thesis studied the ability to approximate temperature across a 2D plane for a material undergoing a solid/liquid phase change. The 2D temperature approximations across the container agree with the 2D temperature profile based on the internal thermocouple data with a typical error of  $4.26^{\circ}\text{C}$  for the lower plane and  $3.34^{\circ}\text{C}$  for the upper plane, as shown in Figure 4.41. The ultrasonically based temperature approximations were shown to be robust relative to the measured wall temperatures. The methods described in this thesis yielded repeatable results, with ultrasonically based temperature approximations which were within  $10^{\circ}\text{C}$  of the temperatures based on internal thermocouples.

#### *5.1 Scientific Contributions*

One scientific contribution of this thesis is the identification of a temperature gradient inside a solid material without use of a waveguide. In waveguides, physical characteristics within the material partially reflect the ultrasonic wave back to the transducer. These characteristics are placed at known intervals, and the temperature gradient is approximated based on the change in time of flight of the reflected waves (see

e.g. [41]). The temperature approximations presented in this thesis are viable when the wax is solid and require no internal features to be present inside the wax.

The second scientific contribution is the mathematic approximation of the material temperature along an ultrasonic path. The radial temperature approximations are a function of  $\Delta T$ ,  $T_{\text{wall}}$ , and the parameter  $X$ . The algorithm which approximates temperature uses captured ultrasonic data, measured boundary conditions, and defined parameters which represent the thermal response of the wax in this experimental configuration. One driving parameter,  $\Delta T$ , is the difference between  $T_{\text{melt}}$  and the temperature of the molten wax, also called  $T_{\text{molten}}$ . This temperature difference was modeled as a single value while the heater is on, followed by a linear decrease, reflecting the heat loss to ambient conditions after the heater is turned off. A temperature profile along a radial path is approximated by the algorithm, and the effective time of flight for that profile is calculated. This effective TOF is compared to the measured TOF from the ultrasonic data, and the difference between the two is minimized by varying the parameter  $X$ . This parameter directly affects the corresponding physical state the wax is assumed to be in, either fully solid, partially liquid at the center, or fully liquid.

## *5.2 Future Work*

Non-invasive temperature measurement is relevant to many different industries. The wax chosen for this experiment has some similarity to thermoplastics, but there are other waxes which have different thermal behavior and may be used as a basis for understanding and approximating temperature through other waxes, thermoplastics, or a petro-chemical. The radial temperature approximation algorithm developed in this thesis can be modified to match the behavior of other waxes and materials in similar

experimental setups. The algorithm can also be refined to better reflect the physical behavior of the wax, such as with the equations used for  $\Delta T$ .

### *5.3 Conclusions*

This thesis has accomplished 2D temperature approximation using only bulk speed of sound, taken from measured ultrasonic data, and externally measured boundary conditions, as set forth in the introduction. The methods used resulted in planar temperature approximations with a typical variation of 3-6°C from the 2D temperature approximation based on the recorded internal thermocouple data.

## APPENDIX

## APPENDIX A

### Radial Temperature Profiles and TOF Comparisons

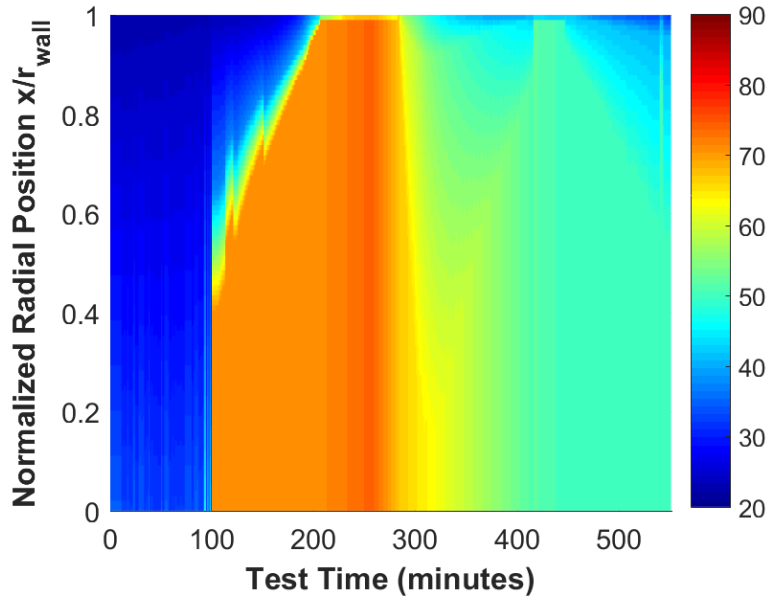


Figure A.1. Radial temperature profile for Channel 1.

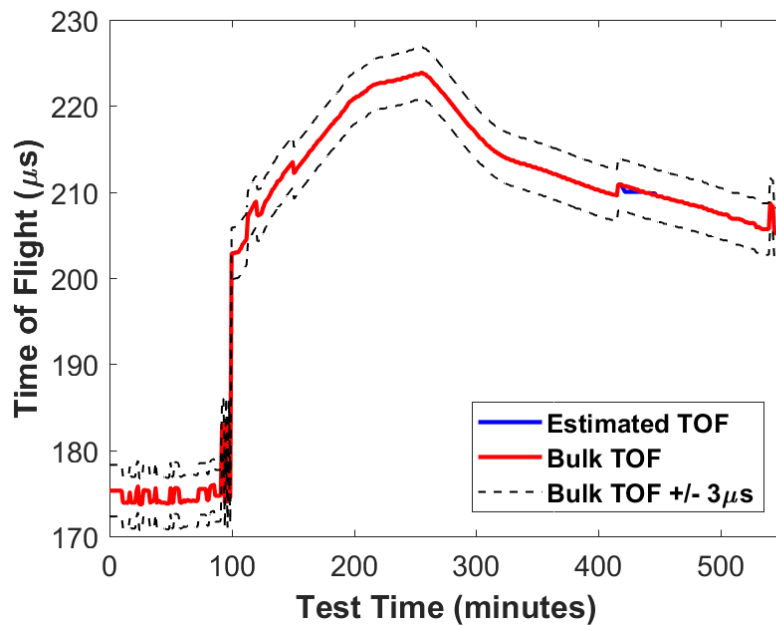


Figure A.2. Estimated and bulk TOF comparison for Channel 1.

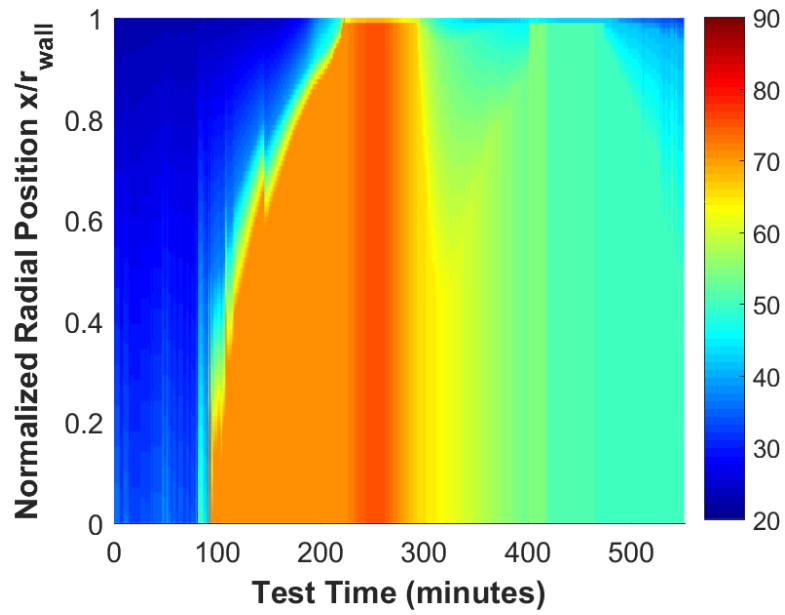


Figure A.3. Radial temperature profile for Channel 2.

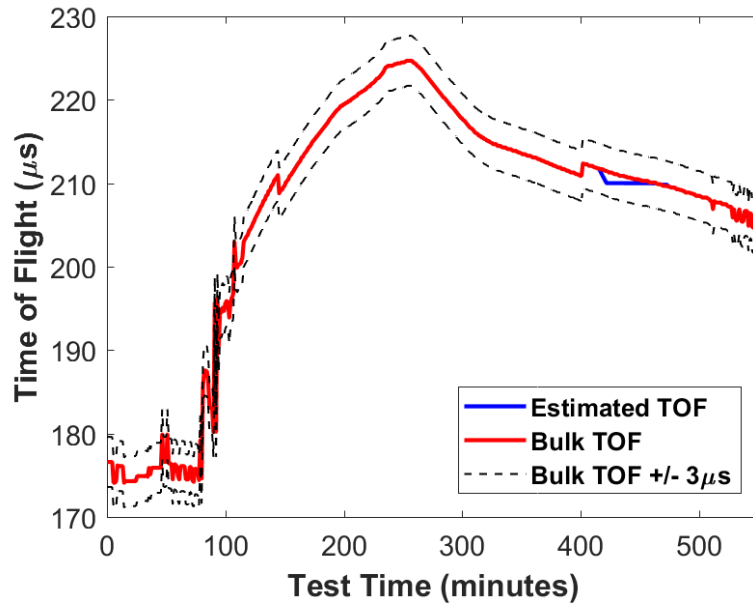


Figure A.4. Estimated and bulk TOF comparison for Channel 2.

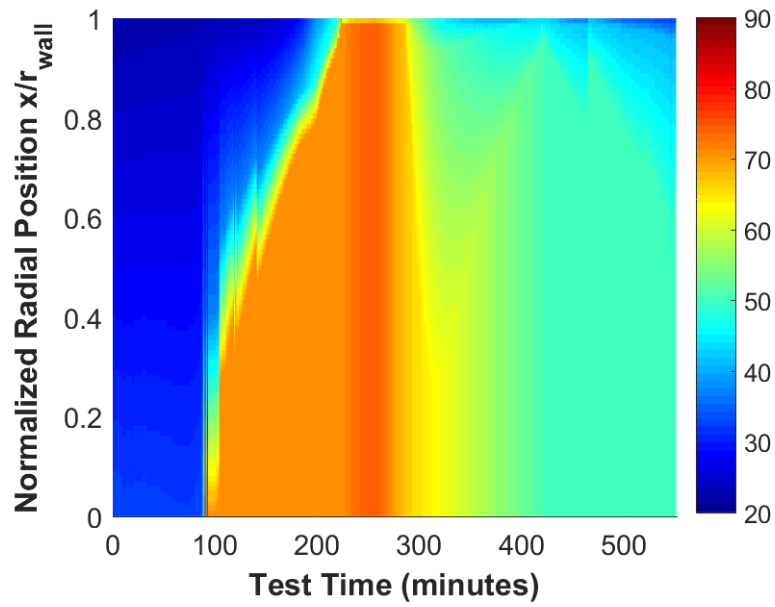


Figure A.5. Radial temperature profile for Channel 3.

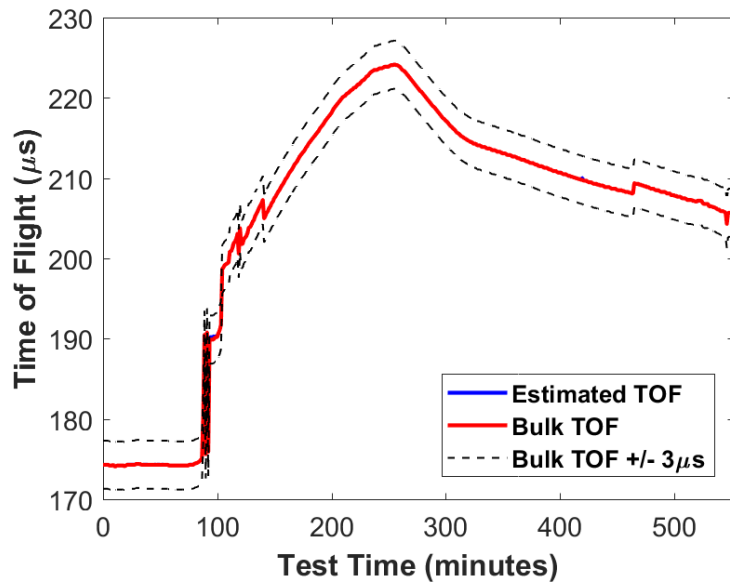


Figure A.6. Estimated and bulk TOF comparison for Channel 3.

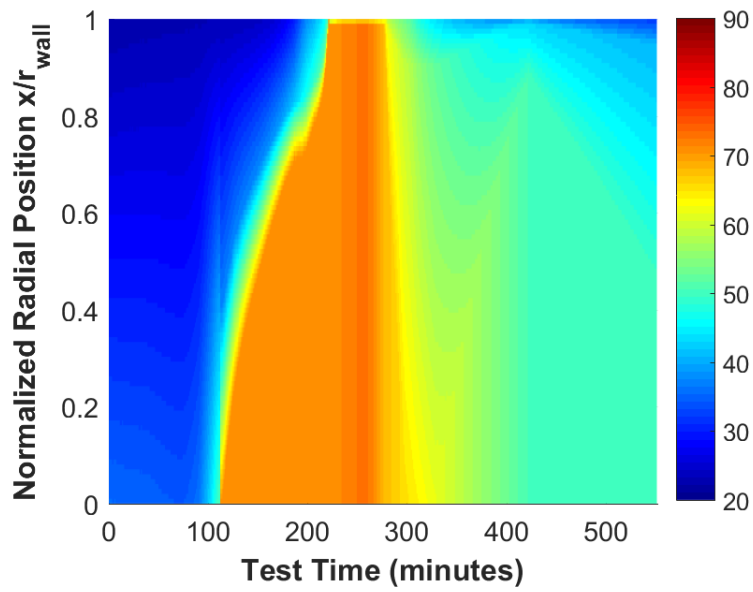


Figure A.7. Radial temperature profile for Channel 4.

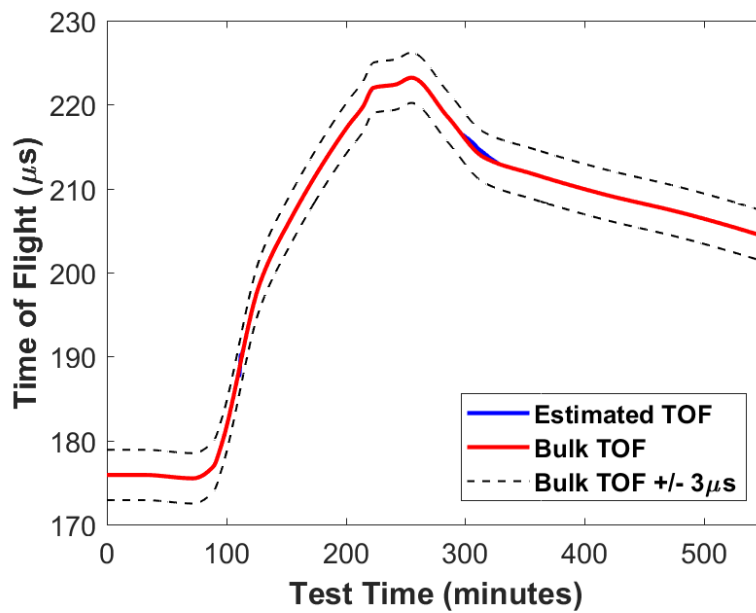


Figure A.8. Estimated and bulk TOF comparison for Channel 4.

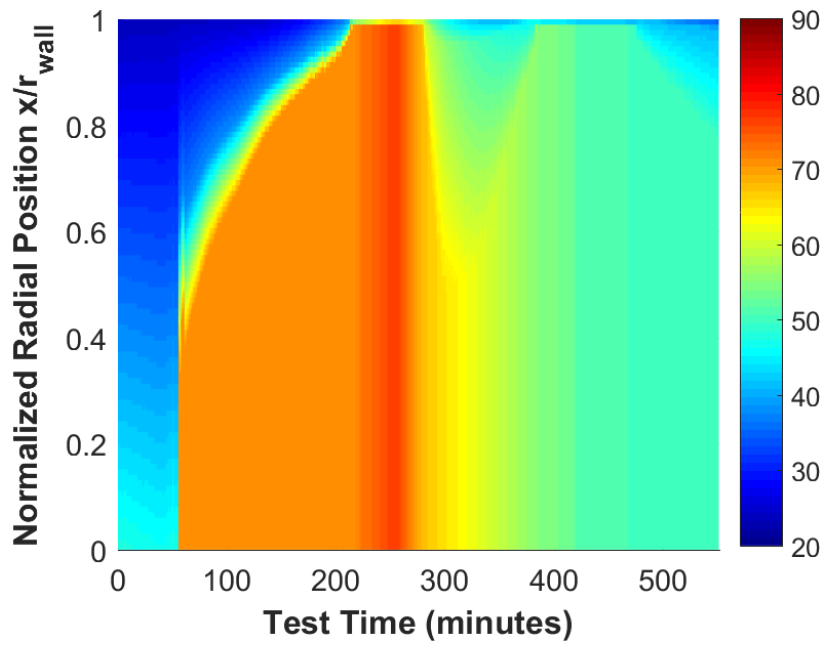


Figure A.9. Radial temperature profile for Channel 6.

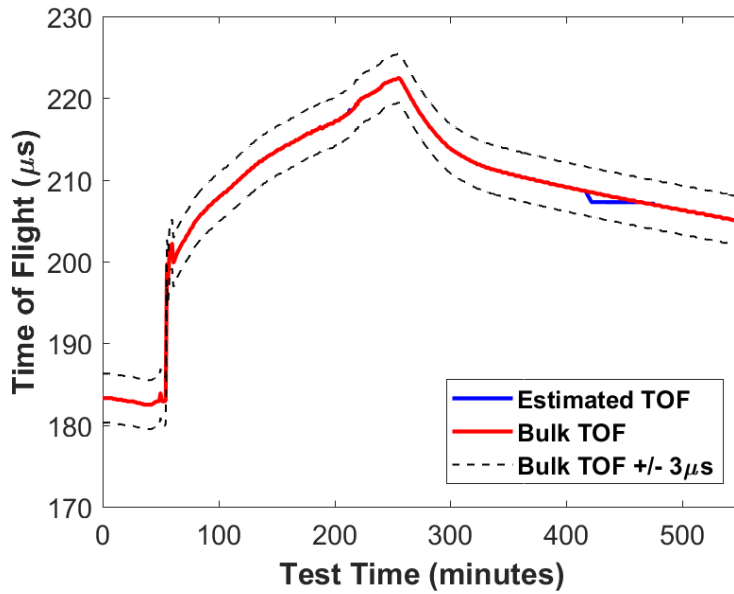


Figure A.10. Estimated and bulk TOF comparison for Channel 6.

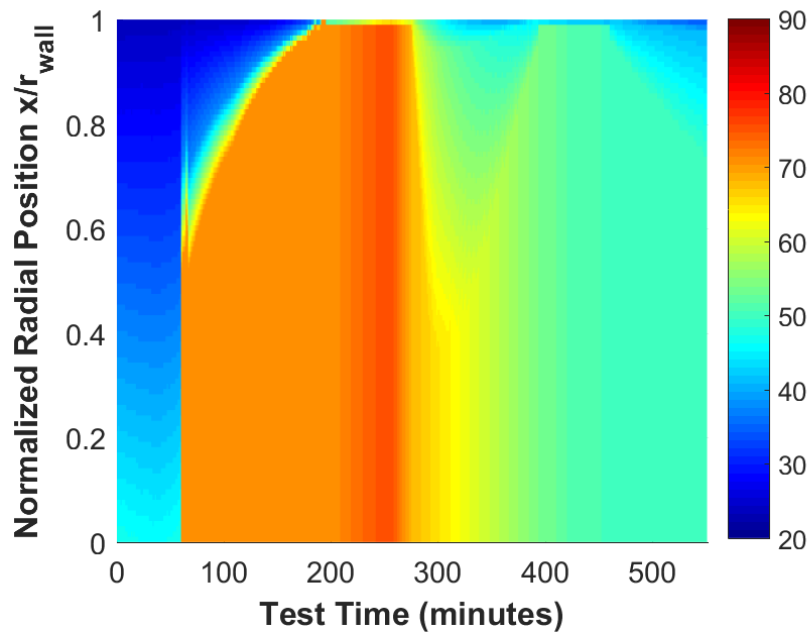


Figure A.11. Radial temperature profile for Channel 7.

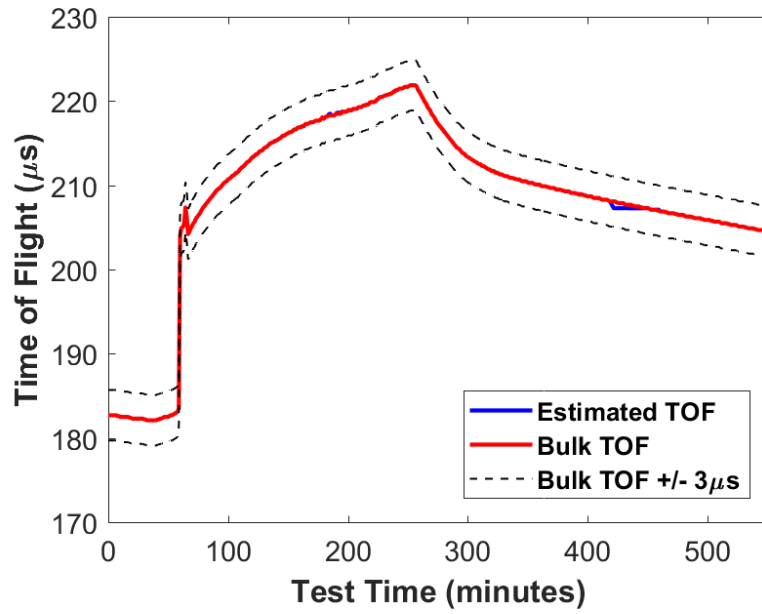


Figure A.12. Estimated and bulk TOF comparison for Channel 7.

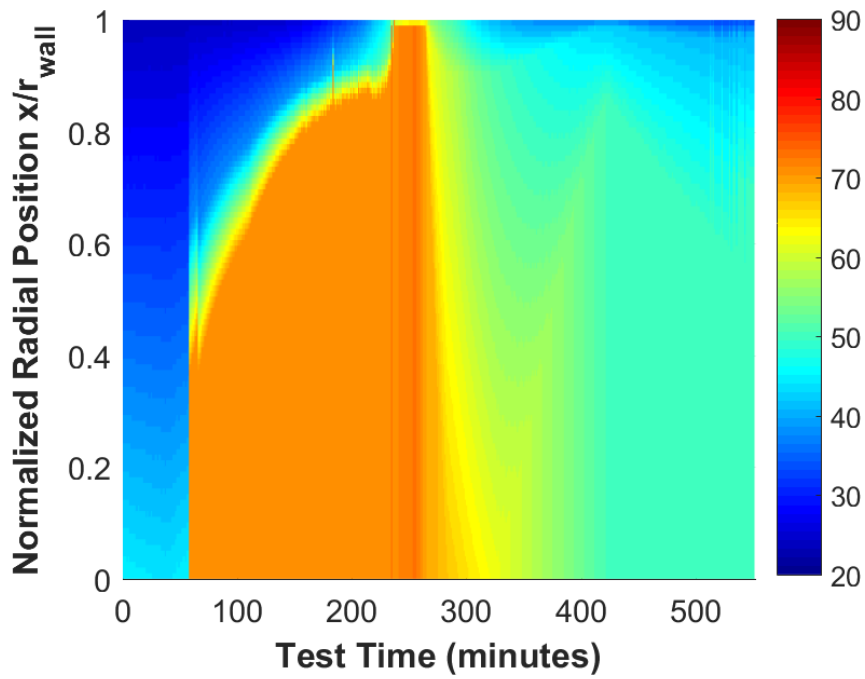


Figure A.13. Radial temperature profile for Channel 8.

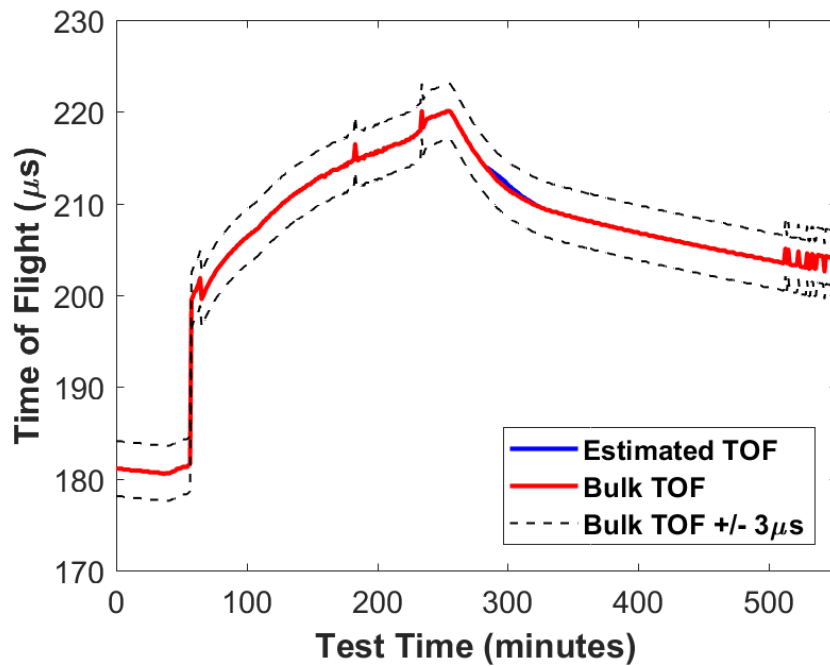


Figure A.14. Estimated and bulk TOF comparison for Channel 8.

## BIBLIOGRAPHY

- [1] Trusler, J. P. M., 1991, *Physical Acoustics and Metrology of Fluids*, Taylor & Francis Group, New York.
- [2] Colclough, A. R., Quinn, T. J., and Chandler, T. R. D., 1979, "An Acoustic Redetermination of the Gas Constant," *Proceedings of the Royal Society A*, **368**(1732).
- [3] Moldover, M. R., Trusler, J. P. M., Edwards, T. J., Mehl, J. B., and Davis, R. S., 1988, "Measurement of the Universal Gas Constant R Using a Spherical Acoustic Resonator," *Physical Review Letters*, **60**(249).
- [4] Mayer, A. M., 1873, "II. On an Acoustic Pyrometer," *The London, Edinburgh, and Dublin Philosophical Magazine and Journal of Science*, **45**(297), pp. 18–22.
- [5] Green, S. F., 1985, "An Acoustic Technique for Rapid Temperature Distribution Measurement," *The Journal of the Acoustical Society of America*, **77**.
- [6] Bramanti, M., Salerno, E. A., Tonazzini, A., Pasini, S., and Gray, A., 1996, "An Acoustic Pyrometer System for Tomographic Thermal Imaging in Power Plant Boilers," *IEEE Transactions on Instrumentation and Measurement*, **45**(1), pp. 159–167.
- [7] Jia, R., Xiong, Q., Xu, G., Wang, K., and Liang, S., 2017, "A Method for Two-Dimensional Temperature Field Distribution Reconstruction," *Applied Thermal Engineering*, **111**, pp. 961–967.
- [8] Shen, X., Xiong, Q., Shi, X., Wang, K., Liang, S., and Gao, M., 2015, "Ultrasonic Temperature Distribution Reconstruction for Circular Area Based on Markov Radial Basis Approximation and Singular Value Decomposition," *Ultrasonics*, **62**, pp. 174–185.
- [9] Fujii, M., and Zhang, X., 2001, "Noncontact Measurement of Internal Temperature Distribution in a Solid Material Using Ultrasonic Computed Tomography," *Experimental Thermal and Fluid Science*, **24**(3–4), pp. 107–116.
- [10] Schmidt, P. L., Greg Walker, D., Yuhas, D. J., and Mutton, M. M., 2014, "Thermal Measurements Using Ultrasonic Acoustical Pyrometry," *Ultrasonics*, **54**(4), pp. 1029–1036.
- [11] Zhu, N., Jiang, Y., and Kato, S., 2005, "Ultrasonic Computerized Tomography (CT) for Temperature Measurements with Limited Projection Data Based on Extrapolated Filtered Back Projection (FBP) Method," *Energy*, **30**(2–4), pp. 509–522.

- [12] McClements, D. J., and Gunasekaran, S., 1997, "Ultrasonic Characterization of Foods and Drinks: Principles, Methods, and Applications," *Critical Reviews in Food Science and Nutrition*, **37**(1), pp. 1–46.
- [13] Gregg, C., 2017, "The Observation of Phase State and Temperature Using Noninvasive Ultrasonic Waves," Baylor University.
- [14] D'Orazio, T., Leo, M., Distante, A., Guaragnella, C., Pianese, V., and Cavaccini, G., 2008, "Automatic Ultrasonic Inspection for Internal Defect Detection in Composite Materials," *NDT & E International*, **41**(2), pp. 145–154.
- [15] Tuziuti, T., Tsuge, A., Nishida, M., and Kanematsu, W., 2014, "Measurement of Speed of Sound in Poly(Lactic Acid)-Clay Composite," *Ultrasonics*, **54**(4), pp. 1010–1014.
- [16] Lionetto, F., Tarzia, A., and Maffezzoli, A., 2007, "Air-Coupled Ultrasound: A Novel Technique for Monitoring the Curing of Thermosetting Matrices," *IEEE Transactions on Ultrasonics, Ferroelectrics and Frequency Control*, **54**(7), pp. 1437–1444.
- [17] Lionetto, F., and Maffezzoli, A., 2013, "Monitoring the Cure State of Thermosetting Resins by Ultrasound," *Materials*, **6**(9), pp. 3783–3804.
- [18] Samet, N., Maréchal, P., and Duflo, H., 2011, "Ultrasound Monitoring of Bubble Size and Velocity in a Fluid Model Using Phased Array Transducer," *NDT & E International*, **44**(7), pp. 621–627.
- [19] Brown, E. C., Olley, P., and Coates, P. D., 2000, "In Line Melt Temperature Measurement during Real Time Ultrasound Monitoring of Single Screw Extrusion," *Plastics, Rubber and Composites*, **29**(1), pp. 3–13.
- [20] Ning, F., Cong, W., Hu, Y., and Wang, H., 2017, "Additive Manufacturing of Carbon Fiber-Reinforced Plastic Composites Using Fused Deposition Modeling: Effects of Process Parameters on Tensile Properties," *Journal of Composite Materials*, **51**(4), pp. 451–462.
- [21] Carlson, J. E., van Deventer, J., Scolan, A., and Carlander, C., 2003, "Frequency and Temperature Dependence of Acoustic Properties of Polymers Used in Pulse-Echo Systems," *IEEE Symposium on Ultrasonics, 2003*, IEEE, Honolulu, HI, USA, pp. 885–888.
- [22] Stair, S., 2017, "Nondestructive Inspection and Characterization of Complex Engineering Materials via Ultrasound Techniques," Dissertation, Baylor University.
- [23] Jost, E., 2017, "Non-Destructive Inspection Approach Using Ultrasound to Identify the Material State and Internal Temperature for Amorphous and Semi-Crystalline Materials," Baylor University.

- [24] “NDE/NDT Resource Center” [Online]. Available: [https://www.nde-ed.org/index\\_flash.php](https://www.nde-ed.org/index_flash.php). [Accessed: 05-Feb-2019].
- [25] Schmerr, L. W., 1998, *Fundamentals of Ultrasonic Nondestructive Evaluation: A Modeling Approach*, Plenum Press, New York.
- [26] Tsai, W.-Y., Chen, H.-C., and Liao, T.-L., 2006, “High Accuracy Ultrasonic Air Temperature Measurement Using Multi-Frequency Continuous Wave,” *Sensors and Actuators A: Physical*, **132**(2), pp. 526–532.
- [27] Rae, P. J., and Brown, E. N., 2016, “Some Observations on Measuring Sound Speeds in Polymers Using Time-of-Flight,” *Experimental Techniques*, **40**(3), pp. 1085–1097.
- [28] Halmen, N., Kugler, C., Hochrein, T., Heidemeyer, P., and Bastian, M., 2017, “Ultrasound Tomography for Inline Monitoring of Plastic Melts,” *Journal of Sensors and Sensor Systems*, **6**(1), pp. 9–18.
- [29] Maffezzoli, A., Quarta, E., Luprano, V. A. M., Montagna, G., and Nicolais, L., 1999, “Cure Monitoring of Epoxy Matrices for Composites by Ultrasonic Wave Propagation,” *Journal of Applied Polymer Science*, **73**(10), pp. 1969–1977.
- [30] Sia, T. F., Liu, X. L., Chiu, W. K., and Paton, R., 2002, “Glass Transition and Viscoelastic Behaviour of Partially Cured Composites,” *Composite Structures*, **57**(1–4), pp. 489–493.
- [31] Figueiredo, M. M. F., Goncalves, J. L., Nakashima, A. M. V., Fileti, A. M. F., and Carvalho, R. D. M., 2016, “The Use of an Ultrasonic Technique and Neural Networks for Identification of the Flow Pattern and Measurement of the Gas Volume Fraction in Multiphase Flows,” *Experimental Thermal and Fluid Science*, **70**, pp. 29–50.
- [32] Häupler, M., Peyronel, F., Neeson, I., Weiss, J., and Marangoni, A. G., 2014, “In Situ Ultrasonic Characterization of Cocoa Butter Using a Chirp,” *Food Bioprocess Technol*, **7**(11), pp. 3186–3196.
- [33] Oliveira, P. A., Silva, R. M. B., Morais, G. C., Alvarenga, A. V., and Félix, R. P. B. C., 2016, “Speed of Sound as a Function of Temperature for Ultrasonic Propagation in Soybean Oil,” *Journal of Physics: Conference Series*, **733**, p. 012040.
- [34] Hægström, E., and Luukkala, M., 2000, “Ultrasonic Monitoring of Beef Temperature During Roasting,” *LWT - Food Science and Technology*, **33**(7), pp. 465–470.

- [35] Russell, T., Heller, B., Jack, D., and Smith, D., 2018, “Prediction of the Fiber Orientation State and the Resulting Structural and Thermal Properties of Fiber Reinforced Additive Manufactured Composites Fabricated Using the Big Area Additive Manufacturing Process,” *Journal of Composites Science*, **2**(2), p. 26.
- [36] Wang, Z., and Smith, D., 2018, “Rheology Effects on Predicted Fiber Orientation and Elastic Properties in Large Scale Polymer Composite Additive Manufacturing,” *J. Compos. Sci.*, **2**(1), p. 10.
- [37] Praher, B., Straka, K., and Steinbichler, G., 2013, “An Ultrasound-Based System for Emperature Distribution Measurements in Injection Moulding: System Design, Imulations and off-Line Test Measurements in Water,” *Measurement Science and Technology*, **24**(8).
- [38] Hoppman, C., and Wipperfurth, J., 2017, “Ultrasound Tomography for Spatially Resolved Melt Temperature Measurements in Injection Moulding Processes,” *J Appl Mech Eng*, **06**(03).
- [39] Jia, Y., Puga, M., Butterfield, A. E., Christensen, D. A., Whitty, K. J., and Skliar, M., 2013, “Ultrasound Measurements of Temperature Profile Across Gasifier Refractories: Method and Initial Validation,” *Energy & Fuels*, **27**(8), pp. 4270–4277.
- [40] Chen, T.-F., Nguyen, K. T., Wen, S.-S. L., and Jen, C.-K., 1998, “Temperature Measurement of Polymer Extrusion by Ultrasonic Techniques,” *Measurement Science and Technology*, **10**(3), p. 139.
- [41] Jia, Y., Chernyshev, V., and Skliar, M., 2016, “Ultrasound Measurements of Segmental Temperature Distribution in Solids: Method and Its High-Temperature Validation,” *Ultrasonics*, **66**, pp. 91–102.
- [42] “What’s A Transducer - Piezo Theory | APC International” [Online]. Available: <https://www.americanpiezo.com/piezo-theory/whats-a-transducer.html>. [Accessed: 11-Feb-2019].
- [43] Svilainis, L., 2013, “Review of High Resolution Time of Flight Estimation Techniques for Ultrasonic Signals,” Telford.
- [44] 2018, “Paraffin Wax: Chemical Compound,” *Encyclopedia Britannica*.
- [45] “Material Sound Velocities | Olympus IMS” [Online]. Available: <https://www.olympus-ims.com/en/ndt-tutorials/thickness-gage/appendices-velocities/>. [Accessed: 22-May-2019].
- [46] 2012, “Technical Drawing of Vestil Product PAIL-STL-RI.”

- [47] “Piecewise Cubic Hermite Interpolating Polynomial (PCHIP) - MATLAB Pchip”  
[Online]. Available: <https://www.mathworks.com/help/matlab/ref/pchip.html>.  
[Accessed: 10-Jun-2019].